UNIVERSITÀ
DEGLI STUDI
DI TRIESTE

UNIVERSITÀ DEGLI STUDI DI TRIESTE

XXXVII CICLO DEL DOTTORATO DI RICERCA IN
SCIENZE DELLA RIPRODUZIONE E DELLO SVILUPPO

Mechanical forces regulate cardiac cell proliferation

Settore scientifico-disciplinare: MED/03 – Genetica medica.

DOTTORANDO
FRANCESCO RICCITELLI

COORDINATORE
PROF. PAOLO GASPARINI

SUPERVISORE DI TESI
PROF. SERENA ZACCHIGNA

ANNO ACCADEMICO 2023/2024

UNIVERSITÀ DEGLI STUDI DI TRIESTE

PhD Program in:
Reproduction and Developmental Sciences

Mechanical forces regulate cardiac cell proliferation

PhD student:
Francesco Riccitelli MD

Supervisor:
Chiar.ma Prof. Serena Zacchigna
Co-supervisor:
Giulio Ciucci, PhD

Cycle XXXVII

Table of contents

Abbreviations

CAF	Cancer-associated fibroblasts
CM	Cardiomyocytes
DDR	DNA Damage Response
EdU	5-ethynyl-2'-deoxyuridine
ECM	Extracellular Matrix
EHT	Engineered Heart Tissue
ERK	Extracellular Signal-Regulated Kinases
FAK	Focal Adhesion Kinase
GFP	Green Fluorescent Protein
HA	Hyaluronic Acid
HHT	Heterotopic Heart Transplant
IF	Intermediate Filaments
INM	Inner Nuclear Membrane
KDM	Lysine-Specific Demethylases
LAD	Lamina-Associated Domains
LINC	Linkers of the Nucleoskeleton to the Cytoskeleton
LOX	Lysyl Oxidase
LV	Left Ventricle
LVAD	Left Ventricular Assist Device
MAPK	Mitogen-Activated Protein Kinase
MT	Microtubules
NE	Nuclear Envelope
NPC	Nuclear Pore Complex
ONM	Outer Nuclear Membrane
PBS	Phosphate-Buffered Saline
ROCK	Rho-Associated Protein Kinase
ROS	Reactive Oxygen Species
siRNA	Small Interfering RNA
SUN	Sad1 and UNC-84 Domain-Containing Protein
SYNE	Spectrin Repeat-Containing Nuclear Envelope Protein
TAZ	Transcriptional Co-Activator with PDZ-Binding Motif
TME	Tumor Microenvironment
UPS	Undifferentiated Pleomorphic Sarcoma
YAP	Yes-Associated Protein

1. Introduction

1.1. Cardiomyocytes and the Heart's Regenerative Capacity

1.1.1. Starting points

Lower vertebrates, such as fish and amphibians, are able to regenerate the myocardium after damage, a capacity that contrasts sharply with the limited regenerative ability observed in mammals. The mammalian heart has long been viewed as a post-mitotic organ, meaning it lacks the ability to regenerate significantly in adult life. This belief is supported by the common understanding that myocardial damage heals through scarring rather than new tissue growth. However, recent evidence challenges this notion by revealing that the heart retains a modest regenerative capacity. For example, studies using ^{14}C-dating and imaging mass spectrometry have shown that cardiomyocytes renew at a rate of about 1% per year, translating to the formation of 30-40 million new cells annually. This renewal rate, although low, is not insignificant and appears to increase after myocardial infarction [1;11].

The limited regenerative potential of adult cardiomyocytes is closely tied to their behavior during development. Cardiomyocytes actively proliferate during embryogenesis, contributing to heart growth, but they exit the cell cycle shortly after birth. This developmental shift is thought to result from postnatal changes such as increased oxygen levels, heightened oxidative stress, and mechanical strain, which collectively inhibit cell division [2-3].

The origin of new cardiomyocytes in the adult heart remains debated. Some researchers suggest that existing cardiomyocytes may divide, while others highlight the role of endogenous cardiac progenitor cells. These progenitor cells, identified by markers like Sca-1 or c-Kit, have been shown in animal studies to generate not only cardiomyocytes but also vascular cells. However, the clinical relevance of these findings, especially in humans, is still uncertain.

This modest yet demonstrable regenerative capacity of the heart has spurred interest in developing therapies to enhance it. Inspired by the remarkable regenerative abilities of lower vertebrates, scientists aim to uncover mechanisms that could overcome the barriers imposed by postnatal changes, potentially unlocking the heart's latent regenerative potential. Such advancements offer hope for innovative treatments for heart disease and myocardial repair [1].

1.1.2. Loss of angiogenic potential after birth in cardiac endothelial cells

Using Apelin-CreER mice to genetically trace sprouting endothelial cells, some study observed a notable divergence in angiogenic behavior between skeletal and cardiac muscle [4]. Both tissue types responded similarly to pro-angiogenic stimuli, such as VEGF, by activating Apelin expression, a key marker of endothelial activation. However,

only skeletal muscle endothelial cells progressed beyond this activation phase. In skeletal muscle, Apelin-positive cells were able to sprout, form elongated vascular structures, activate Notch signaling, and incorporate into newly forming arteries. This robust angiogenic response underscores the tissue's regenerative and vascular adaptability.

In contrast, cardiac endothelial cells exhibited a profound limitation in their angiogenic potential. Despite expressing Apelin in response to the same stimuli, these cells failed to initiate sprouting or form functional vascular networks. Apelin-positive endothelial cells in the heart transiently persisted but did not contribute to new vessel formation, effectively stalling angiogenesis at an early stage. This inability to progress further reflects the heart's intrinsic challenges in both regenerative vascularization and tumor-induced angiogenesis. Tumor cells, which typically induce robust angiogenesis to sustain their growth and metastasis in other tissues, encounter resistance in the cardiac microenvironment. Consequently, tumors grow less in the heart than in the skeletal muscle: cardiac endothelial cells do not adequately respond to tumor-driven pro-angiogenic signals, a phenomenon potentially linked to their specialized biology and the postnatal loss of angiogenic and regenerative potential.

These findings suggest that skeletal muscle endothelial cells possess an intrinsic ability to fully execute the angiogenic program, a capability that is markedly deficient in cardiac endothelial cells. This disparity not only illustrates the heart's limited capacity for regeneration but also its unique resistance to tumor-associated vascular remodeling, driven by a developmental decline in angiogenic capacity after birth [4].

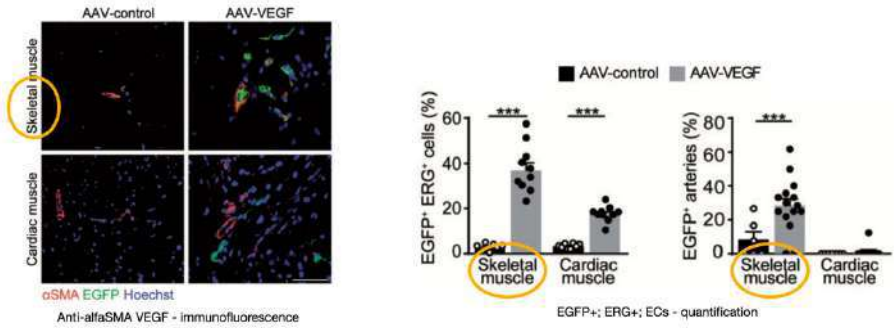

Figure 1-1. Representative immunofluorescence staining of skeletal and cardiac muscle of Apln-CreER; R26mT/mG mice injected with either AAV-control (left) or AAV-VEGF (right), labelled with anti-a-SMA antibodies [left image].

Quantification of the number of EGFPþ ERGþ endothelial cells (% of ERGþ cells) and quantification of the number of ar- teries containing EGFPþ endothelial cells (% of total arteries)- [right image].

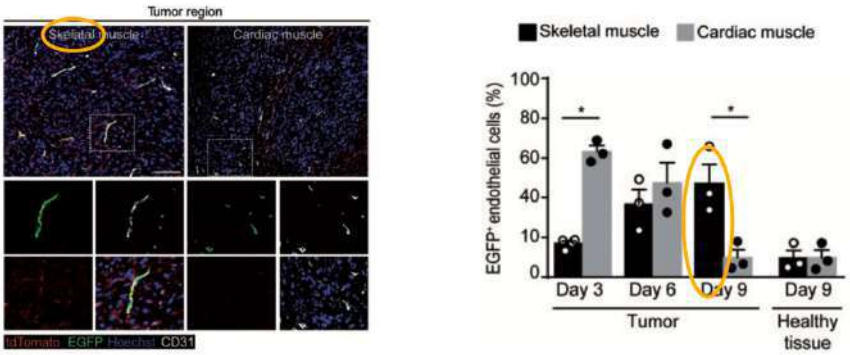

Figure 1-2. Representative immunofluorescence staining of skeletal and cardiac muscle of Apln-CreER; R26mT/mG mice injected with LG cells, labelled with anti-CD31 antibodies 9 days after cancer cell in- jection. Panels on the left show regions highly infiltrated by cancer cells, whereas panels on the right show the surrounding, healthy tissue. Boxed regions are magnified in the lower panels to show split channels [left image]. Quantification of the number of EGFPþ endothelial cells (% of CD31þ cells) at the indi- cated time points in either the tumour region or the surrounding, healthy tissue [right image].

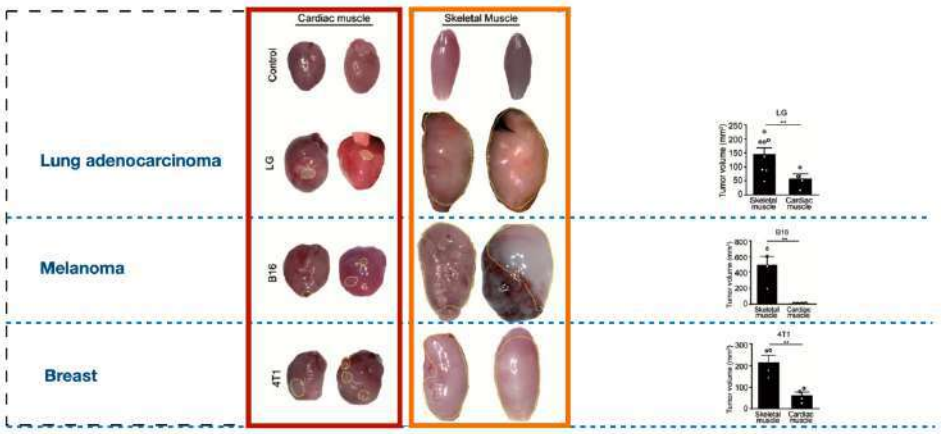

Figure 1-3. Representative whole organ pictures of hearts and skeletal muscle not treated or injected with LG lung adenocarcinoma (left). Relative quantification (right).

1.2. The Role of Hyperoxic Stress and Reactive Oxygen Species (ROS) in Cardiomyocyte Proliferation Arrest

Recent investigations emphasize the pivotal role of reactive oxygen species (ROS) and DNA damage response (DDR) in cardiomyocyte proliferation arrest during the early postnatal period. This shift is marked by a surge in ROS production and DDR markers within the first week after birth, correlating with a sharp decline in the proliferative ability

of cardiomyocytes [2]. The findings suggest a causal link between oxidative stress and cardiomyocyte cell-cycle exit.

In utero, fetal circulation is characterized by specialized shunts—ductus venosus, foramen ovale, and ductus arteriosus—that prevent a clear segregation of venous and arterial blood. This system results in moderate oxygen saturation levels, with umbilical venous blood reaching approximately 80-90% oxygenation and left ventricular output around 65% [5]. Following birth, the closure of these shunts establishes a distinct arterial-venous separation, exposing cardiomyocytes to an oxygen-rich environment. This postnatal hyperoxia triggers a metabolic transition from anaerobic glycolysis to oxidative phosphorylation in mitochondria [6]. While this adaptation enhances energy efficiency, it concurrently increases ROS production, leading to oxidative DNA damage and DDR activation [7].

The study by Canseco et al. (2015) [3] further elaborates on these processes, highlighting mitochondrial biogenesis as a central component of ROS generation and DDR activation postnatally. Mitochondrial proliferation amplifies oxidative stress, which inhibits cardiomyocyte proliferation by activating the DDR pathways. However, evidence from left ventricular assist device (LVAD) studies reveals that mechanical unloading can reverse this cascade. In patients undergoing LVAD implantation, reductions in mitochondrial content and DDR markers, such as phosphorylated ATM protein, were observed. This was associated with a re-entry of cardiomyocytes into the cell cycle, suggesting that metabolic and mechanical stresses jointly regulate cardiomyocyte quiescence and proliferation. So, prolonged mechanical unloading induces adult human cardiomyocyte proliferation, possibly through prevention of mitochondria-mediated activation of DDR.

This interplay underscores the complexity of cardiomyocyte development and the intrinsic limitations of the postnatal heart's regenerative capacity. ROS-driven oxidative damage, exacerbated by hyperoxic stress and mechanical load, establishes a cellular environment resistant to regeneration. However, therapeutic interventions like LVADs provide insights into potential pathways for enhancing cardiac regeneration through targeted modulation of these stressors.

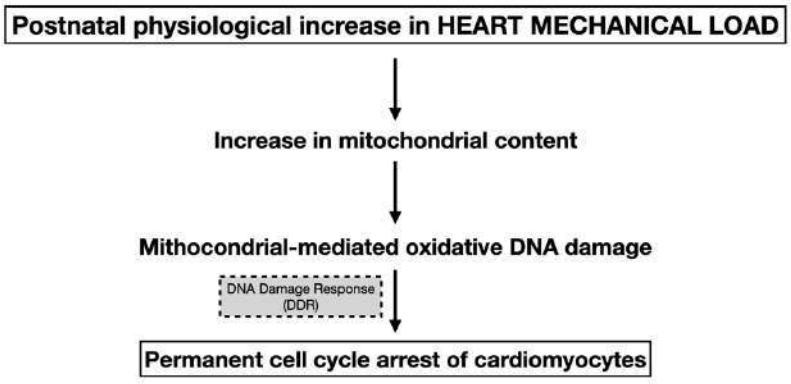

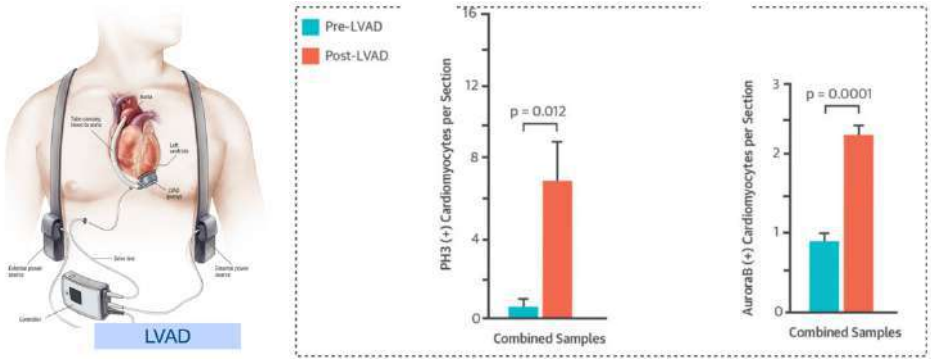

Figure 1-4. Cardiomyocyte Proliferation in LVAD Patients: Prolonged Mechanical Unloading Results in a Switch From Hypertrophic to Hyperplastic Cardiomyocyte Growth: Post-LVAD, cardiomyocytemitosis, shown by increased pH3-positive cardiomyocytes (left), and cardiomyocytecytokinesis, shown by increased Aurora B localization to cytokinetic furrows (right), were both significantly increased in the combined samples.

1.3. Heart cancers

1.3.1. Epidemiology

Primary and secondary cardiac tumors exhibit distinct characteristics in terms of incidence and pathogenesis. Primary cardiac tumors are exceptionally rare, with post-mortem studies reporting frequencies ranging from 0.001% to 0.28% [8]. These tumors are predominantly benign, such as myxomas, lipomas, and fibroelastomas, with malignant forms like sarcomas being far less common. Secondary cardiac tumors, however, are more prevalent, as the heart can serve as a metastatic site for any malignant neoplasm capable of distant spread [9]. The incidence of cardiac metastases, while more frequent than primary tumors, remains lower than in other organ systems. This is paradoxical given the heart's extensive vascularization, which theoretically should facilitate metastatic seeding.

When cardiac metastases occur, they primarily affect the pericardium, large vessels, and coronary arteries, with limited infiltration of the myocardium [10]. Tumors such as melanoma, lung cancer, breast cancer, and mesothelioma are particularly likely to metastasize to the heart. Despite the heart's susceptibility to metastatic involvement, its intrinsic protection against primary tumorigenesis and limited tumor growth capacity reflect unique biological constraints.

The rarity of primary cardiac tumors may be explained by the negligible proliferative capacity of mature CMs. Studies suggest that only 1% of CMs divide annually in adulthood [1; 11]. Although CMs are not the sole cell type in the heart—fibroblasts, smooth muscle cells, vascular endothelial cells, peripheral neurocytes, and myocardial interstitial cells also contribute to its cellular composition—tumors originating from these other cell types are equally uncommon [12]. This raises intriguing questions about

the heart's unique microenvironment and its resistance to tumorigenesis, highlighting the need for further exploration into the mechanisms underlying its tumor biology.

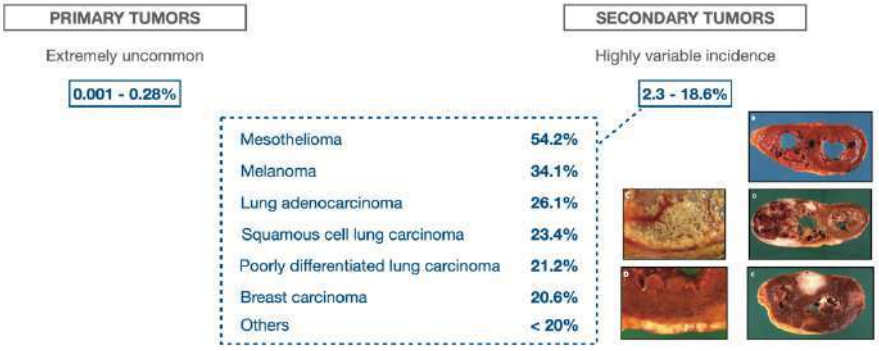

Figure 1-5. A schematic representation of heart's tumor epidemiology.

1.3.2. Primary Cardiac Neoplasms

Primary cardiac tumors predominantly arise in the epicardium and atrial walls, areas subject to lower mechanical stress [13]. These neoplasms can be benign or malignant.

1.3.2.1. Benign Primary Cardiac Neoplasms

Approximately 75% of primary cardiac tumors are benign, including myxomas, lipomas, fibroelastomas, rhabdomyomas, fibromas, and angiomas [14-15].

Myxomas are the most frequently encountered benign cardiac tumors, originating from the endocardium and projecting into the cardiac chambers. They are most commonly found in the left atrium and typically manifest between the fourth and sixth decades of life. These tumors exhibit a slight predominance in females and are predominantly sporadic in nature, with no established genetic or underlying conditions linked to their occurrence [16]. Myxomas are known for their potential to cause symptoms related to obstruction or embolization, necessitating prompt surgical intervention in most cases.

Rhabdomyomas, on the other hand, are congenital hamartomas that represent the most prevalent cardiac tumors in pediatric populations. These lesions generally present in neonates within the first two weeks of life and are frequently multiple, often localized in the ventricles or the interventricular septum. A significant proportion of rhabdomyomas are associated with tuberous sclerosis, indicating a genetic basis for their development. Unlike other tumors, rhabdomyomas often regress spontaneously over time, with surgical intervention reserved for severe or symptomatic cases where critical cardiac function is compromised [17].

Fibromas are another type of benign cardiac tumor, originating from connective tissue and predominantly seen during childhood, with a notable male predominance. These tumors often arise in the interventricular septum or the left ventricle. Clinically, they can present with a variety of symptoms, including arrhythmias, syncope, chest pain, or signs

of heart failure, depending on their size and location. In symptomatic cases, surgical resection may be required to alleviate these complications and restore normal cardiac function [18].

Lipomas, by contrast, tend to occur in elderly, overweight females and are typically located in subendocardial, subepicardial, or endocardial regions. These tumors are often asymptomatic and discovered incidentally. As a result, treatment is generally unnecessary unless the lipoma becomes symptomatic, in which case surgical resection may be considered to address the patient's symptoms and prevent further complications [19].

Hamartomas of mature cardiac myocytes are a distinct form of cardiac tumor, characterized by solitary lesions composed of disorganized and hypertrophic cardiomyocytes. These tumors are more commonly observed in males, approximately twice as often as in females, and typically present during the second decade of life. Although relatively rare, their identification is critical to differentiating them from other cardiac pathologies and managing potential complications associated with their presence [20]. Together, these tumors highlight the diverse nature of benign cardiac neoplasms, each with unique clinical presentations, prognoses, and management strategies.

1.3.2.2. Malign Primary Cardiac Neoplasms

Malignant primary cardiac tumors are exceptionally rare, accounting for only 25% of all primary cardiac neoplasms, with sarcomas representing the vast majority. Other malignancies in this category include mesotheliomas, lymphomas, and tumors associated with Li-Fraumeni syndrome, highlighting the diverse but infrequent nature of these conditions [15].

Among malignant primary cardiac tumors, high-grade undifferentiated pleomorphic sarcoma (UPS) is the most common. This tumor typically arises in the posterior wall of the left atrium and has an average onset age of 47, with a slight predominance in females. UPS is composed of undifferentiated, mitotically active, and pleomorphic cells that often lack distinctive histological features, making diagnosis challenging. Immunohistochemistry is of limited utility in identifying UPS, with overexpression of the MDM2 gene and protein being the most consistent diagnostic marker [21]. Despite its rarity, the aggressive nature of UPS necessitates early recognition and intervention, although the prognosis remains guarded.

Angiosarcomas are the second most frequent malignant primary cardiac tumors, predominantly occurring in the right atrium or atrioventricular sulcus. These tumors are generally sporadic and are characterized by their highly vascular nature, which often leads to symptoms such as chest pain, weight loss, dyspnea, and cardiac tamponade. Prognosis is poor, with a five-year mortality rate of approximately 87%, reflecting the aggressive progression and limited treatment options available for this malignancy [22].

Pericardial mesothelioma, while exceedingly rare, represents 50% of all primary pericardial tumors. This malignancy arises from either the visceral or parietal pericardium and is notable for its lack of strong correlation with asbestos exposure, a factor commonly linked to pleural mesotheliomas. Clinically, pericardial mesotheliomas present with pericardial effusion, tamponade, and chest discomfort, and the prognosis is dismal, with a median survival time typically under six months [23]. The rarity of this condition, coupled with its nonspecific symptoms, often delays diagnosis, further complicating management.

Cardiac lymphomas, while constituting only 1–2% of all cardiac tumors, are more frequently observed in immunocompromised patients. The majority of these malignancies are B-cell lymphomas that primarily involve the right atrium and pericardium. Patients with cardiac lymphomas often present with systemic symptoms such as fever, fatigue, and weight loss, in addition to localized manifestations including chest pain and, in rare cases, pulmonary embolism [24]. The diagnosis and treatment of cardiac lymphomas require a multidisciplinary approach due to their systemic nature and involvement of critical cardiac structures.

Collectively, malignant primary cardiac tumors are rare but aggressive entities that pose significant diagnostic and therapeutic challenges. The limited regenerative capacity of cardiac tissues and the unique biology of cardiac cells may contribute to their low incidence but also hinder effective therapeutic responses, emphasizing the need for continued research into these complex conditions.

1.3.2.3. Cardiac metastases

Cardiac metastases are significantly more common than primary cardiac tumors, with reported incidences ranging from 0.7% to 3.5% in the general population and up to 14.2% in individuals with advanced malignancies. Despite this, cardiac metastases are less frequently observed compared to metastases in other organs, such as the liver or lungs. The relative rarity of cardiac involvement is intriguing, given the heart's extensive vascularization, which would theoretically make it a prime target for metastatic spread.

When cardiac metastases do occur, they typically affect the pericardium, large vessels, and coronary arteries, with myocardial infiltration being relatively uncommon. This distribution reflects the pathways through which malignant cells can reach the heart: hematogenous dissemination, lymphatic spread, direct extension from adjacent structures (such as the lungs), or venous invasion via the vena cava. The specific tumor types most likely to metastasize to the heart include carcinomas of the breast and lung, hematological malignancies (such as lymphomas and leukemias), and melanomas. In contrast, slower-growing neoplasms, such as prostate cancer, rarely metastasize to the heart [8].

The cardiac microenvironment poses intrinsic barriers to metastasis. Tumor cells that reach the heart may encounter challenges such as the high mechanical stress of cardiac contractions and the unique properties of cardiac endothelial cells, which exhibit limited

angiogenic potential. This contrasts with endothelial cells in other tissues, which are more responsive to pro-angiogenic stimuli. The inability to establish a robust vascular network in cardiac tissues likely contributes to the restricted growth of metastases in this organ.

Clinically, cardiac metastases often present with nonspecific symptoms or remain asymptomatic, making diagnosis challenging. When symptomatic, patients may experience pericardial effusion, tamponade, arrhythmias, or heart failure, depending on the location and extent of the metastatic involvement. Pericardial involvement is the most common and is frequently associated with effusions that can progress to tamponade, requiring urgent intervention [8].

1.4. Mechanobiology

Mechanobiology is the study of how cells sense and respond to mechanical stimuli [25]. Recent advancements in mechanobiology have enhanced our understanding of mechanotransduction mechanisms [26].

Mechanotransduction is the process by which mechanical signals from the extracellular matrix (ECM) or cytoskeleton are converted into intracellular biochemical signals, triggering cellular responses. This process involves the ECM, cytoskeleton, LINC (linker of nucleoskeleton and cytoskeleton) complexes, and the nucleus. Mechanotransduction enables cells to rapidly adapt to changes in their physical environment, playing critical roles in cell differentiation, tissue function, and disease development [27].

1.4.1. The Role of Mechanical Forces

Various studies suggest that elevated mechanical load in the heart inhibits cardiomyocyte proliferation. First, during postnatal development, subendocardial myocardial cells experience higher mechanical loads and proliferate less compared to subepicardial cells [28]. Second, lower vertebrates capable of heart regeneration in adulthood have low-pressure cardiac chambers [29]. Third, an inverse relationship between mechanical load (increased cavity pressure and volume, resulting in cardiomyocyte stretching) and proliferation has been observed in patients with end-stage heart failure treated with LVADs, which bypass the left ventricle and pump blood directly into the aorta. Post-mortem analyses of hearts from LVAD-implanted patients revealed increased cardiomyocyte replication [3].

Reducing mechanical stimuli, such as cavity pressure and volume, allowed cardiomyocytes to re-enter the cell cycle. These findings suggest that mechanical forces may inhibit cardiomyocyte duplication.

1.4.2. Nuclear Mechanotransduction: Structure, Function, and Key Components

The nucleus, the largest and most rigid organelle in the cell, plays a central role in mechanotransduction, where mechanical stimuli are converted into biochemical signals that influence various cellular processes. The structural organization and mechanical properties of the nucleus are crucial for functions such as gene expression, cell division, differentiation, apoptosis, and disease progression, including cancer metastasis [30-34]. The mechanical properties of the nucleus not only reflect its structural integrity but also mediate interactions with the extracellular environment, making nuclear mechanics a key indicator of cellular responses to mechanical stimuli [35].

1.4.2.1. Structural Organization of the Nucleus and Mechanotransduction Pathways

The nucleus is composed of the nuclear envelope (NE), nuclear lamina, chromatin, and nucleoplasm, with the nuclear lamina and chromatin being the primary contributors to nuclear mechanics [27]. As a semi-permeable barrier, the nuclear envelope encapsulates the genome and serves as a dynamic interface for mechanical and biochemical signal transmission between the cytoskeleton and the chromatin. The nuclear lamina, composed of type A and type B lamins, provides structural support, while chromatin, the complex of DNA and associated proteins, mediates genomic activities and contributes to nuclear stiffness.

1.4.2.2. Mechanisms of Nuclear Mechanotransduction

Mechanotransduction within the nucleus involves several mechanisms that allow the cell to sense and respond to external mechanical stimuli. These include the deformation of the nuclear envelope, conformational changes in associated proteins, and alterations in chromatin organization. These pathways operate synergistically to translate mechanical forces into biochemical signals, ultimately influencing cellular behavior [27].

<u>Nuclear Lamina and Its Role in Mechanotransduction</u>

The nuclear lamina, an elastic mesh located beneath the inner nuclear membrane, is primarily composed of type A and type B lamins, which are intermediate filaments critical for maintaining nuclear shape and mechanical stability. The lamina resists deformation during mechanical stress and supports cellular processes like migration and spreading [36-37]. Lamins also regulate chromatin organization by tethering chromatin domains, known as lamina-associated domains (LADs), to the nuclear periphery. The stability of these interactions is vital for maintaining nuclear integrity and influencing gene silencing or activation [38].

<u>Chromatin Dynamics in Response to Mechanical Forces</u>

Chromatin, which mediates DNA-centric activities such as transcription, replication, and repair, contributes significantly to nuclear stiffness. Unlike the elastic nuclear lamina, chromatin exhibits viscoelastic behavior under mechanical forces, with its compaction

state determining its stiffness and capacity to respond to stress [39]. Mechanical forces applied to the nucleus can alter chromatin compaction, reorganizing chromatin territories and influencing gene expression. These changes often involve LADs and the repositioning of chromatin to enable or restrict transcriptional activity [41]. The viscoelastic properties of chromatin also facilitate the absorption of mechanical stress, protecting nuclear integrity during deformation.

Nuclear Envelope and Pore Complexes in Signal Transmission

The nuclear envelope (NE) is a key structural and functional component in mechanotransduction. It houses nuclear pore complexes (NPCs), which regulate the bidirectional trafficking of molecules such as transcription factors, RNA, and ions. Under mechanical stress, the NE and NPCs undergo deformation, influencing the transport of signaling molecules like YAP/TAZ, which are critical regulators of mechanosensitive gene expression [42]. Stretching of the NE increases pore permeability, allowing the translocation of transcription factors into the nucleus to activate stress-responsive genes. Additionally, the NE connects to the cytoskeleton through the linker of nucleoskeleton and cytoskeleton (LINC) complex, enabling the direct transmission of extracellular mechanical forces to the chromatin.

1.4.2.3. Emerging Insights from Literature

Recent studies have expanded our understanding of how nuclear mechanics contribute to cellular function and pathology. For example, alterations in nuclear stiffness and mechanotransduction pathways have been linked to cancer progression and metastasis. Loss of lamin A/C or dysregulation of chromatin organization has been implicated in enhanced nuclear deformability, enabling cancer cells to navigate through dense extracellular matrices during metastasis [43-44]. Additionally, mutations in nuclear envelope proteins, such as lamins, can disrupt mechanotransduction, contributing to laminopathies and other diseases associated with defective nuclear mechanics [33].

The interplay between the nuclear lamina, chromatin, and the NE highlights the nucleus's role as a central hub for integrating mechanical and biochemical signals. Advances in high-resolution imaging and biomechanical assays continue to unravel the complexity of nuclear mechanotransduction, paving the way for targeted therapies in mechanopathologies, including cancer and fibrotic diseases.

In conclusion, nuclear mechanotransduction is a multifaceted process involving the structural and functional components of the nucleus. The nuclear lamina, chromatin, and nuclear envelope each play distinct but interconnected roles in sensing and transmitting mechanical signals, underscoring the nucleus's pivotal role in cellular mechanobiology.

1.4.3. The LINC Complex: A Critical Mediator of Nuclear Mechanotransduction

The Linker of Nucleoskeleton and Cytoskeleton (LINC) complex is an essential structural and functional mediator in the mechanotransduction pathway, facilitating the direct transmission of mechanical forces from the extracellular environment to the nucleus. By connecting the nuclear envelope (NE) to the cytoskeleton, the LINC complex serves as a dynamic interface that integrates signals from the extracellular matrix (ECM), cytoskeleton, and nucleus, thereby orchestrating cellular responses to mechanical stress [44-45; 66]. This connection enables cells to adapt to their physical surroundings and maintain structural integrity under various physiological and pathological conditions.

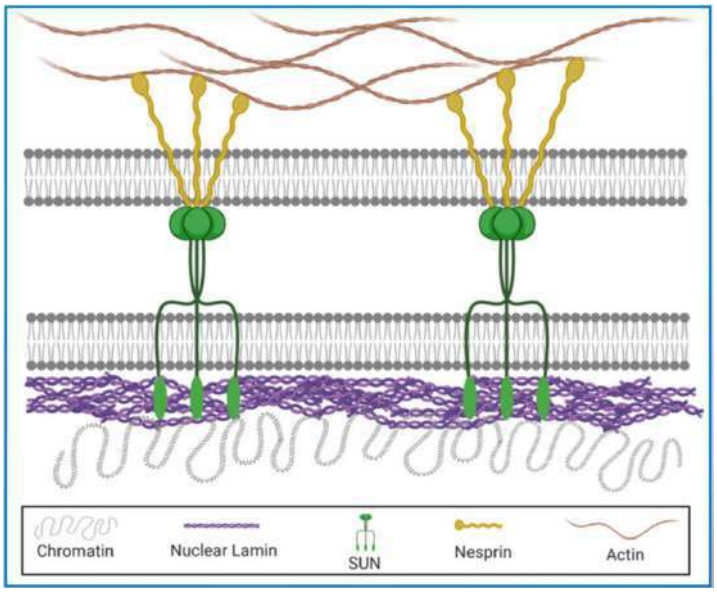

Figure 1-6. THE LINC complex: a schematic representation.

1.4.3.1. Structure and Composition of the LINC Complex

The LINC complex is primarily composed of nesprins and SUN (Sad1 and UNC-84 homology) proteins, which are transmembrane proteins located in the outer nuclear membrane (ONM) and inner nuclear membrane (INM), respectively. Nesprins extend into the cytoplasm and interact with cytoskeletal filaments, such as actin, microtubules, and intermediate filaments, creating a direct link between the cytoskeleton and the nuclear envelope [46]. Nesprins possess a conserved KASH (Klarsicht, ANC-1, and Syne Homology) domain that anchors them to SUN proteins within the perinuclear space. On the nuclear side, SUN proteins connect to the nuclear lamina, a dense network of intermediate filaments composed of lamin A/C and lamin B, which provides mechanical support to the nucleus and anchors chromatin [47].

1.4.3.2. Functional Roles of the LINC Complex

Force Transmission and Nuclear Deformation

The LINC complex plays a pivotal role in transmitting forces exerted on the ECM through the cytoskeleton to the nucleus. This force transmission causes nuclear deformation, which can alter chromatin organization, gene expression, and nuclear pore permeability, ultimately influencing cellular behavior. For example, during cell migration through confined spaces, the LINC complex enables the nucleus to respond to mechanical constraints by reorganizing its structure and reducing stiffness [48].

Nuclear Positioning and Shape Maintenance

The LINC complex ensures proper nuclear positioning within the cell, which is critical for cellular polarity, division, and migration. Disruption of nesprins or SUN proteins leads to misaligned nuclei, impaired migration, and altered cellular mechanics, as demonstrated in studies on laminopathies and other diseases associated with defective nuclear-cytoskeletal connectivity [49]. Furthermore, the LINC complex maintains the elliptical shape of the nucleus, ensuring optimal spatial organization for chromatin and nuclear processes.

Mechanotransduction and Gene Regulation

By transmitting mechanical signals, the LINC complex plays a central role in activating mechanosensitive pathways that regulate gene expression. For instance, mechanical stress transmitted through the LINC complex can lead to chromatin remodeling and activation of mechano-responsive genes, such as those involved in tissue remodeling and repair. This function is particularly important in cells exposed to dynamic mechanical environments, such as endothelial cells, fibroblasts, and osteocytes [42].

Pathophysiological Implications

Dysregulation of the LINC complex has been implicated in several diseases, including laminopathies, cancer, and cardiovascular disorders. In cancer, altered expression of nesprins and SUN proteins compromises nuclear stiffness and mechanotransduction, facilitating tumor cell invasion and metastasis [44]. In cardiac and skeletal myopathies, mutations in nesprin or SUN protein genes disrupt nuclear positioning and force transmission, contributing to disease progression.

1.4.3.3. Implication for tumorigenesis

The Linker of Nucleoskeleton and Cytoskeleton (LINC) complex serves as a critical structural and functional bridge between the nuclear envelope and the cytoskeleton. This intricate system enables the transmission of mechanical signals across cellular compartments, influencing processes such as mechanotransduction, nuclear integrity, and gene regulation. In the context of cancer, alterations in the LINC complex have profound effects, driving tumorigenesis, enhancing cellular plasticity, and facilitating invasive and metastatic behaviors.

Downregulation and Mutation of LINC Components

One of the key observations in cancer research is the consistent downregulation of LINC complex components in tumor cells. Proteins such as SUN1/2, located within the inner nuclear membrane, and nesprins, which span the outer nuclear membrane, exhibit significantly reduced expression in various malignancies. In breast cancer tissues and cell lines, SUN1/2 and nesprin-2 expression levels are markedly diminished, correlating with tumor aggressiveness and progression [50]. Additionally, mutations in nesprin genes, such as SYNE1 and SYNE2, are frequently identified in cancers of the breast, colon, and gastrointestinal tract [51]. These molecular disruptions impair nuclear-cytoskeletal connectivity, undermining the cell's ability to maintain structural stability and respond to mechanical stimuli.

Mechanotransduction Disruption and Tumor Plasticity

Mechanotransduction, the cellular process of sensing and responding to mechanical forces, is critically dependent on the functionality of the LINC complex. In cancer cells, the dysregulation of this system leads to significant impairments in force transmission from the extracellular matrix (ECM) to the nucleus. This loss of mechanosensitivity allows cancer cells to bypass mechanical constraints within the tumor microenvironment, enabling them to migrate and invade surrounding tissues more effectively [52]. Moreover, the disruption of the LINC complex alters chromatin organization and gene expression, promoting oncogenic signaling pathways that drive uncontrolled proliferation and survival.

Nuclear Mechanics and Genomic Instability

The LINC complex also plays a vital role in maintaining nuclear mechanics and genomic stability. The connection between nesprins and SUN proteins strengthens the nuclear envelope and supports chromatin organization. In cancer cells, the disruption of these interactions leads to nuclear deformation and fragility. During migration through confined spaces, such weakened nuclei are prone to rupture, resulting in DNA damage and genomic instability. This instability not only fuels tumor progression but also contributes to intratumoral heterogeneity, a hallmark of advanced cancers [49].

Enhanced Metastatic Potential

The loss of LINC-mediated nuclear-cytoskeletal connectivity enhances cancer cell adaptability, particularly in overcoming physical barriers during invasion and metastasis. Mechanosensitive transcription factors, such as YAP/TAZ, are hyperactivated in the absence of proper LINC function, driving gene expression programs associated with cell migration, proliferation, and survival [42]. These alterations allow tumor cells to detach from primary sites, invade distant tissues, and establish secondary tumors.

Therapeutic Implications

The critical role of the LINC complex in maintaining cellular and nuclear integrity highlights its potential as a therapeutic target in cancer. Restoring the expression or function of SUN proteins and nesprins may help reinforce nuclear stability and reduce metastatic capabilities. Additionally, targeting downstream pathways activated by LINC dysfunction, such as YAP/TAZ signaling, represents a promising strategy for limiting

tumor progression. Small molecules, gene therapies, or biologics designed to modulate LINC complex components could potentially mitigate the invasive and metastatic behavior of cancer cells.

1.4.3.4. Future Directions

Recent studies highlight the versatility of the LINC complex in cellular mechanobiology. Advanced imaging techniques and biophysical tools have uncovered new roles for the LINC complex in nuclear shape adaptation and chromatin organization under varying mechanical conditions [53]. Additionally, therapeutic strategies targeting LINC complex components are being explored for diseases involving aberrant mechanotransduction, such as fibrosis and certain cancers.

1.5. Purpose of the Study and Experimental Research Methods

In this study, we propose that variations in mechanical load significantly influence the proliferation of cancer cells in the heart, potentially providing an explanation for the notably low incidence of cardiac tumors. To investigate this hypothesis, we employed a combination of *in vivo* and *ex vivo* experimental approaches to dissect the interplay between mechanical forces and cancer cell behavior within the myocardium. Specifically, we demonstrated that mechanical load suppresses, while tissue unloading enhances, cancer cell proliferation within the cardiac microenvironment.

1.5.1. Heterotopic Heart Transplantation (HHT)

To investigate the effects of mechanical forces on cancer cell proliferation within the myocardium, we utilized two complementary methodologies. The first involved the development of an *in vivo* model of cardiac unloading via heterotopic heart transplantation (HHT). In this model, a donor heart was transplanted into the cervical region of a syngeneic recipient mouse. While the donor heart remained perfused through the recipient's circulation, it was mechanically unloaded, allowing us to isolate the effects of reduced mechanical stress on cardiac tissue. This model preserved critical physiological characteristics such as cellular composition and vascularization while eliminating cyclic mechanical strain, providing a unique platform to study mechanical unloading in a living organism.

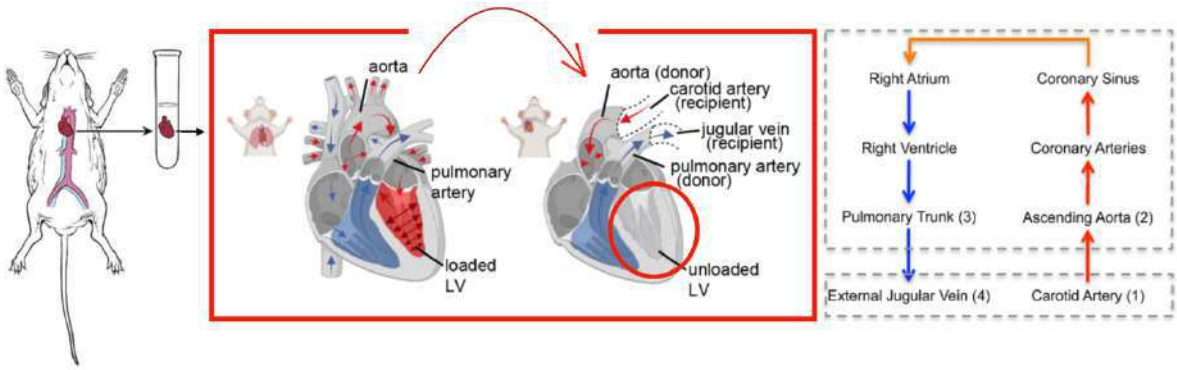

Figure 1-7. Heterotopic Heart Transplantation: a schematic representation.

Studies in humans have previously shown that mechanical unloading of the heart can restore the replicative capacity of terminally differentiated cells, such as cardiomyocytes [3]. This suggests that mechanical pressure, such as that caused by ventricular filling, may play a key role in inhibiting cellular proliferation. Given these insights, the HHT model emerged as a valuable tool for studying the effects of mechanical unloading, initially being developed to investigate immunological mechanisms during acute and chronic graft rejection [54-55].

The HHT model has traditionally involved transplanting a donor heart into an ectopic site in the recipient, typically the abdomen. In the abdominal HHT model for mice, the donor heart's ascending aorta is anastomosed to the recipient's abdominal aorta, and the pulmonary artery is connected to the inferior vena cava [56-57].

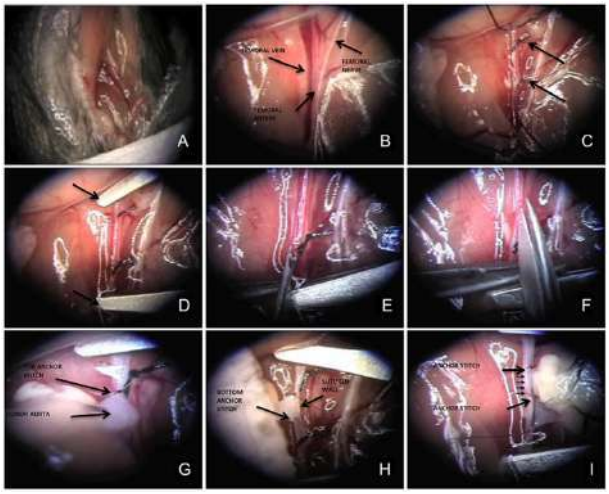

Figure 1-8. An Extraperitoneal Technique for Murine Heterotopic Cardiac Transplantation: surgical times.

However, our study employed a cervical heterotopic transplant model, wherein the donor heart is transplanted into the recipient's neck region. In this model, the recipient's external jugular vein and common carotid artery are anastomosed to the donor heart's pulmonary artery and aorta, respectively [58]. This configuration ensures the donor heart

receives oxygenated blood via the recipient's circulation while mechanically unloading the left ventricle.

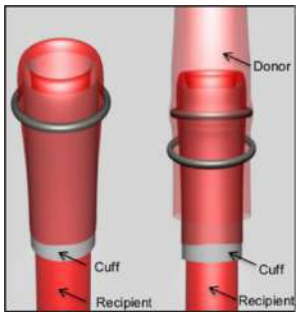

Figure 1-9. A schematic representation of cuffing: the recipient vessel is everted directly on the cuff to subsequently receive the donor vessel.

This model provided an exceptional opportunity to study how unloading influences cellular behavior, including proliferation and gene expression, in a controlled physiological context. Importantly, the heterotopically transplanted heart retained characteristics of a native heart, such as its cellular composition, extracellular matrix, contractile activity, and vascular integrity, while being subjected to significantly altered mechanical forces.

The implications of this model extend beyond basic research into cancer cell proliferation within the myocardium. By leveraging the HHT approach, we aim to elucidate how mechanical unloading can alter cellular and molecular pathways, with a particular focus on understanding how the absence of cyclic mechanical stress impacts cancer cell growth, chromatin remodeling, and gene expression.

1.5.2. Engineered Heart Tissues (EHTs)

Second, we employed Engineered Heart Tissues (EHTs), an advanced tissue engineering platform that allows the generation of three-dimensional (3D) cardiac tissues outside the body. EHTs mimic key structural and functional properties of the native myocardium, providing a highly controlled environment to investigate the effects of mechanical loading and unloading on cellular behavior. This system is particularly advantageous for modeling conditions such as volumetric compression and mechanical unloading, which are challenging to replicate in vivo.

1.5.2.1. Historical and Technical Advances in EHTs

EHT technology was first introduced in the early 2000s by Eschenhagen et al., who developed a method to construct functional cardiac tissues using neonatal rat cardiomyocytes embedded in a hydrogel composed of type I collagen and Matrigel. [59]. Over time, these constructs matured into contractile myocardial cultures, offering a platform to study cardiomyocyte behavior, contractile dynamics, and

mechanotransduction mechanisms. Subsequent refinements in 2010 further enhanced the technology, particularly by adapting the EHT system for high-throughput applications. By miniaturizing the hydrogel constructs into multi-well plate formats, researchers could assess contractile forces across multiple samples simultaneously, greatly increasing the reproducibility and scalability of experiments [60].

1.5.2.2. Methodological Improvements

Two pivotal improvements were introduced during this refinement. First, type I collagen was replaced with fibrinogen, a biopolymer that forms fibrin upon thrombin-mediated polymerization. Fibrin exhibits superior elasticity and softness, closely mimicking the mechanical properties of in vivo fibrin structures. Additionally, fibrin supports the covalent binding of growth factors and is biodegradable, making it an ideal scaffold for cardiac tissue engineering. However, aprotinin supplementation was required to prevent fibrin degradation during the culture period [61]. Second, silicone anchors and Teflon spacers were incorporated into the system. These modifications allowed the creation of molds within a 24-well plate format, where cardiomyocytes could attach to paired silicone posts to form 3D tissue constructs. These posts provided a stable framework for the developing tissues while enabling precise measurements of contractile forces under different experimental conditions [60].

1.5.2.3. Cultivation and Experimental Application

In practice, EHTs are cultured over 15–30 days under tightly regulated conditions, allowing for tissue maturation and functional development. This setup enables researchers to manipulate mechanical forces with high precision, making it possible to model mechanical loading and unloading scenarios observed in vivo.

1.5.2.4. Integration into this study

For this study, EHTs were instrumental in evaluating the role of mechanical forces on cancer cell proliferation within the cardiac microenvironment. By subjecting EHTs to controlled mechanical stress or unloading conditions, we could simulate the biomechanical environment of the heart and study its effects on cellular behavior in detail.

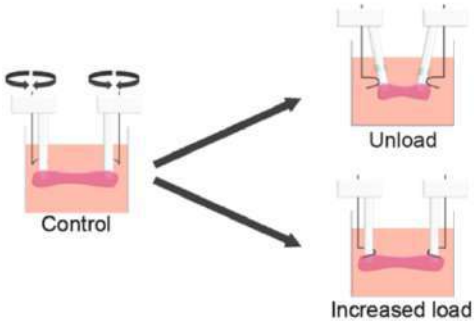

Figure 1-10. Schematic representation of control EHT (left) and its adaptation to induce either unload (top right) or increased load (bottom right).

1.5.3. Comparison Between Cardiac and Extra-Cardiac Metastases Derived from Human Samples

Furthermore, to deepen our understanding of the mechanisms underlying these effects, we analyzed human samples of cardiac metastases and compared them to extra-cardiac lesions from the same patients. This investigation aimed to unravel the molecular and cellular pathways that inhibit cancer cell proliferation within the heart, emphasizing the protective role of mechanical forces in this unique organ environment.

2. Methods

2.1. Cell Culture

In this study, two murine cell lines were utilized: LG1233 [160] and CT26-Cas9-hyg (GeneCopoeia). The LG1233 cells originate from a pulmonary adenocarcinoma and were genetically engineered to stably express green fluorescent protein (GFP). On the other hand, the CT26-Cas9-hyg cells are derived from a colorectal carcinoma and were engineered to stably express both GFP and the CRISPR-associated protein Cas9.
LG1233 cells were cultured in Dulbecco's Modified Eagle Medium (DMEM) supplemented with GlutaMAX (Gibco; glucose concentration: 1 g/L), whereas CT26-Cas9-hyg cells were maintained in Roswell Park Memorial Institute (RPMI) 1640 medium (Corning; glucose concentration: 4.5 g/L). Both media were enriched with 10% fetal bovine serum (FBS) and 0.2% penicillin/streptomycin.
For experimental procedures involving LG1233 cells, the same DMEM-based medium was used, but the glucose concentration was increased to 4.5 g/L to match the experimental requirements.
This standardized approach ensured the optimal growth and stability of the engineered cell lines while maintaining their functional characteristics throughout the study.

2.2. Isolation of Neonatal Rat Cardiomyocytes

Neonatal Wistar rat hearts (postnatal day 0 to 3) were minced into small fragments and subjected to enzymatic digestion using a DNase/Trypsin-based protocol to obtain single-cell suspensions. Following digestion, the collected cells were centrifuged to remove debris, filtered through a 100 µm cell strainer to ensure uniformity, and resuspended in a culture medium composed of:

DMEM (Biochrom F0415)
10% heat-inactivated fetal bovine serum (Thermo Fisher 26140-079)
1% penicillin/streptomycin (Thermo Fisher 15140-122)
1% L-glutamine (200 mM, Gibco)

This process ensured the generation of viable, high-quality cardiomyocytes suitable for subsequent experimental applications.

2.3. Comprehensive Protocol for Cardiac Mechanical Unloading Studies

2.3.1. Ethical Compliance and Animal Housing

All animal experiments were conducted in accordance with the Directive 2010/63/EU of the European Parliament on animal experimentation and in compliance with European and international guidelines (EC Council Directive 86/609, OJL 34, 12 December 1987). The study was approved by the ICGEB Animal Welfare Board, the Ethical Committee, and the Austrian Ministry of Education, Science, and Culture (BMWFW-66.011/0155-WF/V/3b/2017). Animals were housed in ventilated cages with a 12-hour light/dark cycle. Environmental conditions were controlled, maintaining a temperature of 20–22 °C and relative humidity between 45–65%.

2.3.2. Heterotopic Heart Transplantation

The study utilized a modified heterotopic heart transplantation (HHT) technique in which vessels are everted over synthetic cuffs for vascular anastomoses. This approach allowed precise modeling of cardiac mechanical unloading.

2.3.3. Heart Harvesting from the Donor Animal

Donor animals were anesthetized with an intraperitoneal injection of ketamine/domitor (75 mg/kg and 1 mg/kg) or ketamine/xylazine (100 mg/kg and 5 mg/kg). Complete immobilization and maintenance of respiration were confirmed. Sensitivity was tested by applying incremental pressure to a limb, while whisker movement was observed, initiating the procedure only after complete cessation.

The donor mouse was positioned supine on a heated platform at 37°C, and the abdomen was moistened with alcohol to prevent hair contamination. A transverse incision was made to expose the inferior vena cava, which was injected with 500 µL of heparinized saline (1:4 heparin-sodium ratio) to achieve circulatory anticoagulation. The thoracoabdominal cavity was opened along the costal margins, the diaphragm was severed, and the sternum was rotated cranially to expose the heart. The superior vena cavae were isolated and cut to induce venous bleeding, facilitating cardiac flushing with Custodiol® HTK solution at 4°C, either retrogradely (via the ascending aorta) or anterogradely (via the inferior vena cava). The heart was excised and preserved in cardioplegic solution until transplantation.

2.3.4. Cervical Cardiac Transplantation in the Recipient Animal

Recipient mice were anesthetized as described above, and their right cervical region was prepared for surgery. The external jugular vein and common carotid artery were isolated, and cuffs were attached to these vessels using an eversion technique. The harvested heart was placed in an inverted position (with the pulmonary artery oriented laterally and the aorta medially) in the cervical region. The pulmonary artery was anastomosed to the external jugular vein cuff, and the aorta was anastomosed to the carotid artery cuff.

Clamps were sequentially removed to restore perfusion, and the transplanted heart resumed sinus rhythm.
Postoperative analgesics, including carprofen (4 mg/kg) and buprenorphine (0.1 mg/kg), were administered subcutaneously every 12 hours for up to five days to minimize pain. The animals were housed in cages with access to soft food and water.

2.3.5. Carotid-Aortic and Jugulo-Pulmonary Anastomoses

The pulmonary artery of the graft was aligned with the cuffed external jugular vein and secured with a circumferential 8-0 silk ligature, completing the jugulo-pulmonary anastomosis. Similarly, the aorta of the graft was aligned with the cuffed common carotid artery and secured with a silk ligature, completing the carotid-aortic anastomosis. Once clamps on the recipient's vessels were removed, the grafted heart was perfused and resumed contractile activity.

2.3.6. Injection of Tumor Cells and Monitoring

Following recovery, a solution containing murine lung carcinoma cells (LG1233, 1×10^5 cells/animal) was injected tangentially into the myocardium of either the transplanted or native hearts. To label proliferating cells, 5'-ethynyl-2'-deoxyuridine (EdU) was administered intraperitoneally on days 1, 3, 7, 14, 18, 20, and 24 after tumor implantation. Animals were weighed weekly and monitored for clinical signs, including apathy, reduced nutritional intake, and weight loss exceeding 10–15%. If necessary, animals were humanely euthanized via isoflurane inhalation before reaching the experimental endpoint.

2.3.7. Integration with Experimental Goals

This study was conducted in collaboration with the Daniel Swarovski Research Laboratory (Innsbruck), which provided technical expertise and training for mastering these complex procedures. The use of heterotopic heart transplantation enabled the modeling of cardiac mechanical unloading, creating a unique system to study the effects of biomechanical forces on tumor proliferation.
In parallel, LG1233 murine lung carcinoma cells were used to explore whether mechanical unloading in the transplanted heart could create conditions conducive to tumor cell proliferation. By combining mechanical manipulation and tumor cell implantation, this protocol provided critical insights into the interplay between mechanical stress, cardiac biology, and cancer growth.

2.3.8. Significance of the Model

This comprehensive protocol bridges technical precision and biological inquiry, allowing for the reproducible study of cardiac unloading. The combination of HHT models, tumor cell implantation, and proliferative labeling with EdU facilitates detailed investigations into how mechanical forces regulate cancer cell behavior within the myocardium. These

findings hold potential implications for understanding cardiac resistance to cancer and may inform novel therapeutic strategies.

2.4. Generation and Modulation of Fibrin-Based Engineered Heart Tissues (EHTs)

Fibrin-based Engineered Heart Tissues (EHTs) provide a robust and reproducible platform for studying cardiac biology and tumor cell behavior under controlled mechanical conditions. By combining neonatal cardiomyocytes (CMs) and cancer cell lines (e.g., CT26, LG1233, B16), EHTs allow for the investigation of cell proliferation, biomechanical interactions, and load-dependent cellular responses. This protocol describes the preparation, maturation, and modulation of fibrin-based EHTs, along with a custom mechanical load system for precise experimental manipulation.

2.4.1. Cell Preparation and Reconstitution Mixture

CMs were isolated from neonatal Wistar rats (postnatal days 0–3) using the Neonatal Cardiomyocyte Dissociation Kit(Miltenyi, 130-098-373). The reconstitution mixture for EHTs was prepared with the following components:

Cardiomyocytes: 6×10^6 cells/EHT
Bovine fibrinogen: 5 mg/mL (Sigma-Aldrich F8630)
DMEM 10X: 20% (Fisher Scientific, 10134902)
Heat-inactivated horse serum: 10% (Thermo Fisher, 26050-088)
Penicillin/streptomycin: 1% (Thermo Fisher, 15140-122)
Thrombin: 3 µL of 100 U/mL (Merck T7513)

For cancer cell-containing EHTs, specific concentrations of tumor cells were added to the reconstitution mixture:

LG1233 cells: 2×10^5 cells/EHT
B16 melanoma cells: 2×10^5 cells/EHT
CT26 colon carcinoma cells: 3×10^5 cells/EHT

2.4.2. Preparation of Agarose Molds and Casting Setup

Molds were created by adding 1.5 mL of 2% agarose (Invitrogen, 15510-027) into the wells of a 24-well culture plate. Once the agarose solidified, Teflon spacers (12 × 3 × 4 mm) were removed, creating casting wells. Silicone posts were placed within the molds, and 30G needles (Meso-Relle) were bent into hook shapes and positioned near the anchoring areas of the silicone posts. This hook design was chosen to counteract the spontaneous reduction in EHT length that occurs during development due to fibroblast contraction.

The reconstitution mixture (100 µL) was carefully pipetted into the molds containing the silicone posts, and the setup was incubated in a humidified cell culture incubator at 37°C and 7% CO_2 for 2 hours to allow fibrinogen polymerization.

2.4.3. EHT Maturation and Maintenance

After fibrinogen polymerization, 300 µL of EHT culture medium was added to each well to facilitate the gentle removal of the constructs from the molds. The racks containing EHTs were transferred to fresh 24-well culture plates, and the culture medium was replaced every two days. The culture medium consisted of:

DMEM: Biochrom F0415
Horse serum: 10% (Thermo Fisher, 26050-088)
Penicillin/streptomycin: 1% (Thermo Fisher, 15140-122)
Insulin: 10 µg/mL (Sigma-Aldrich I9278)
Aprotinin: 33 µg/mL (Merck A1153)

EHTs were monitored daily, and maturation was confirmed 7–10 days post-casting by the appearance of consistent and synchronous beating. During this period, the hooks were intentionally kept free from contact with the silicone posts to avoid interference with the spontaneous reduction in EHT length.

2.4.4. Adjustable Mechanical Load System

A custom hook-based system was developed to allow precise modulation of mechanical load on EHTs. The design enabled three distinct configurations for mechanical loading:

1. Standard Load (Resting Position): The default configuration where the load was determined by the inherent elasticity of the silicone posts.
2. Unloaded Position: The convex side of the hook was rotated against the silicone posts, reducing the distance between the two ends of the EHT and minimizing tension.
3. Increased Load Position: The concave side of the hook was rotated around the silicone post, increasing stiffness and applying a higher mechanical load to the EHT.

The adjustable mechanical load system allowed precise control over tension, enabling the investigation of how load influences tissue development, CM behavior, and cancer cell proliferation.

2.4.5. Load Modulation Experiments

To study the effects of mechanical load on CM and tumor cell proliferation, EHTs were subjected to:

EdU pulse-labeling: Administered during load modulation experiments lasting 72 hours.
Unloading conditions: Simulated using calcium-free DMEM (Thermo Fisher, 21068028) for 5 days.

The custom hook system ensured consistent and reproducible application of mechanical forces, enabling detailed analysis of biomechanical effects.

2.4.6. Applications and Significance

This protocol provides a robust system for generating functional fibrin-based EHTs with tunable mechanical properties. It has several applications:

Cardiac Biology: Investigating the effects of load modulation on cardiomyocyte contractility, maturation, and survival.

Cancer Research: Exploring tumor cell proliferation, invasion, and interactions with cardiac tissue under varying mechanical stresses.

Drug Testing: Evaluating therapeutic efficacy in a 3D, physiologically relevant environment.

The integration of neonatal cardiomyocytes and cancer cells within fibrin-based scaffolds enables a deeper understanding of the interplay between biomechanical forces and cellular behavior. This system represents a valuable tool for advancing research in cardiac and oncological pathophysiology.

2.5. siRNA Transfection and Lentiviral Transduction in Cancer Cells

To investigate the role of specific genes in cancer cell behavior, siRNA transfection and lentiviral transduction were employed. Cancer cells (CT26, LG1233, or B16) were transfected using the “Lipofectamine RNAiMAX” reagent (Invitrogen, 13778-150), following the manufacturer’s protocol.

2.5.1. siRNA Transfection Protocol

siRNAs targeting specific genes were prepared using Horizon siGENOME SMARTpools, each containing four siRNAs per target. The genes targeted were:

Syne1, encoding Nesprin-1 (Cat # M-062644-00-0005)

Syne2, encoding Nesprin-2 (Cat # M-056764-02-0005)

Syne3, encoding Nesprin-3 (Cat # M-052180-01-0005)

Syne4, encoding Nesprin-4 (Cat # M-054687-01-0005)

Sun1, encoding SUN1 (Cat # M-040715-00-0005)

Sun2, encoding SUN2 (Cat # M-041247-01-0005)

Ubc, encoding Ubiquitin-C (positive control; Cat # M-019408-01-0010)

Kdm4c and Kdm4d, encoding lysine demethylases 4C and 4D, respectively (Cat # M-051504-00-0005, Cat # M-052542-01-0005)

Non-Targeting Control siRNA (NT4; D-001210-04-20), serving as a negative control.

siRNA solutions were diluted in opti-MEM medium (Life Technologies 31985-047) to a final concentration of 50 nMper siRNA and dispensed into 96- or 6-well plates. Lipofectamine RNAiMAX reagent was diluted in opti-MEM and added to the siRNA-containing wells. After 30 minutes, cancer cells were seeded onto the siRNA-laden wells at a concentration of 1.5×10^4 cells/cm^2.

For 2D cultures, the medium was replaced the day after transfection, and cells were fixed after 5 days for downstream analysis.

For EHT incorporation, transfected cells were harvested 12 hours post-transfection using trypsinization and introduced into the EHT casting mixture at a concentration of 3×10^4 CT26 or LG1233 cells per EHT.

2.5.2. Lentiviral Transduction Protocol

For stable gene silencing, cancer cells were transduced with lentiviral vectors containing short-hairpin RNAs (shRNAs) targeting Syne2 (Origene TL517485V) or a scramble shRNA control (Origene TR30021V) at a multiplicity of infection (MOI) of 1. Transduced cells were cultured for 48 hours, followed by selection with 1 µg/mL puromycin for 72 hours to ensure stable knockdown.

2.5.3. Incorporation into EHT Models

After transfection or transduction, cancer cells were introduced into the fibrin-based EHTs as previously described. The cells were added to the reconstitution mixture containing cardiomyocytes, and the EHTs were cultured under controlled conditions for maturation.

2.5.4. Controls and Experimental Validity

A pool of four siRNAs for each targeted gene ensured robust downregulation of the target. The inclusion of Ubc siRNAas a positive control and a non-targeting siRNA control (NT4) ensured specificity and validated the transfection efficiency.

This protocol allows efficient transient or stable knockdown of genes associated with the LINC complex and related pathways, enabling detailed analysis of the impact of mechanical cues and gene expression on cancer cell behavior within EHT models.

2.6. Histology and Immunostaining Protocol

Hearts and Engineered Heart Tissues (EHTs) were fixed in 10% formalin in PBS, embedded in paraffin, and sectioned at a thickness of 4 µm using a microtome (Leica). To prepare the sections for staining, paraffin was removed through a sequential process involving heat treatment (60°C for 1 hour) followed by two xylene baths (30 minutes each). Rehydration was achieved through a series of ethanol dilutions in descending concentrations.

2.6.1. Antigen Retrieval and Permeabilization

Antigen retrieval was performed by boiling the sections in a retrieval buffer containing 10 mM Tris base, 1 mM EDTA, and 0.05% Tween 20 at pH 9.0 for 20 minutes in a microwave. After retrieval, sections were rinsed three times in water and permeabilized for 20 minutes in PBS containing 0.25–0.5% Triton X-100.

2.6.2. EdU Detection

EdU incorporation was visualized using the Click-IT EdU 647 Imaging Kit (Thermo Fisher C10247), following the manufacturer's protocol.

2.6.3. Blocking and Primary Antibody Staining

To reduce non-specific binding, tissue sections were incubated in a blocking solution consisting of 10% horse serum and 0.25% Triton X-100 in PBS for 30 minutes. Following blocking, the sections were incubated overnight at 4°C with primary antibodies diluted 1:100 in the blocking solution. The primary antibodies used included:

Anti-cardiac troponin I (Abcam ab47003)
Anti-cardiac troponin T (Abcam ab8295)
Anti-phospho-Histone H3 (Ser10) (Merck 06-570)
Anti-Ki67 (Abcam ab15580)
Anti-PCM1 (Merck HPA023374)
Anti-Histone H3 (trimethyl K9) (Abcam ab176916)
Anti-Melanoma gp100 (Abcam ab137078)

2.6.4. Secondary Antibody Detection and Nuclear Staining

Primary antibody detection was performed using Alexa Fluor-conjugated secondary antibodies (Thermo Fisher). To visualize nuclei, sections were counterstained with DAPI (Thermo Fisher 62247), and slides were mounted with Fluoromount-GTM Mounting Medium (Thermo Fisher 00-4958-02).

2.6.5. Cross-Sectional Area Analysis

Cross-sectional area analysis was conducted on sections stained with an anti-dystrophin antibody (Abcam ab15277) using the VECTASTAIN ABC Kit (Vectorlabs PK-6100) and ImmPACT DAB substrate (Vectorlabs SK-4105). A minimum cross-sectional area threshold of 40 μm^2 was applied for quantification.

This comprehensive histology and immunostaining protocol enables precise localization and quantification of molecular markers and cellular structures in both cardiac tissues and EHTs, supporting investigations into cell proliferation, tissue architecture, and disease pathology.

2.7. Heart and EHT Mechanical Simulation

To investigate the mechanics of the heart under normal and unloaded conditions, as well as the mechanical properties of Engineered Heart Tissues (EHTs) under different loading scenarios, finite element models were developed for both systems.

2.7.1. Finite Element Simulation of Cardiac Mechanics

A finite element model of the rodent left ventricle (LV) was constructed using a simplified truncated prolate ellipsoid geometry with the following dimensions:

Wall thickness: 1.5 mm

Short-axis radius: 4 mm

Long-axis radius: 8 mm

Myofiber orientations were assigned to rotate from -60° to +60° between the endocardium and epicardium, while sheet orientations were orthogonal to both the fibers and the gradient direction spanning the epicardium to the endocardium.

Systolic contraction was simulated using a FEniCS-based solver for cardiac mechanics, employing P2 finite elementsfor displacement. The boundary conditions were:

Robin boundary condition applied at the epicardium.

Imposed endocardial pressure to simulate intracavity forces.

Fixed motion at the basal plane in the longitudinal direction.

The active contraction was modeled using an active strain approach, where the total deformation tensor was multiplicatively decomposed into active and passive components. Contraction along the fiber direction was controlled using an activation parameter (γ). The myocardium was represented as a transversely isotropic, slightly compressible hyperelastic material.

Simulations were conducted under two conditions:

1. Control (Normal Load): End-systolic pressure (ESP) was set to 15 kPa.
2. Unloaded: Cavity pressure was removed (ESP = 0 kPa).

For each case, deviatoric Cauchy stresses were computed in the fiber, sheet, and sheet-normal directions and averaged across the entire volume of the LV geometry.

2.7.2. Finite Element Simulation of EHT Mechanics

To model the mechanical behavior of EHTs, a cylindrical geometry was created with:

Length: 4000 μm

Radius: 300 μm

Cardiac fibers were assigned along the longitudinal axis of the cylinder to mimic the alignment of cardiomyocytes. A Robin-type boundary condition was applied at both ends to represent the interaction between the EHT and the supporting silicone posts.

Calibration and Control: The spring constant of the Robin boundary condition was calibrated to match experimental data, reproducing an observed ~15% systolic shortening under normal conditions.

Load Modulation Simulations:

1. Increased Load (Stiffened Posts):
    - The spring constant was increased by 10×, simulating stiffer silicone posts.
    - This resulted in a reduction of systolic shortening to ~11%.
2. Unloading (Reduced Resistance):
    - The spring constant was decreased by 10×, representing almost no resistance to shortening.
    - This allowed the EHT to shorten by approximately 20% during contraction.

For each condition, deviatoric Cauchy stresses were computed across the mesh and volume-averaged over a 300 μm-long segment of the cylinder to quantify mechanical stress distribution.

2.7.3. Significance of the Simulations

These simulations provide insights into:

The effects of mechanical unloading on the rodent LV, shedding light on stress redistribution under unloaded conditions.

The impact of load modulation on EHT contraction and stress distribution, offering a framework to study the interplay between mechanical forces and cellular function.

By integrating experimental data with computational modeling, these approaches bridge in vitro EHT studies with in vivo cardiac biomechanics, enabling more comprehensive investigations into cardiac physiology and disease.

2.8. Spatial Transcriptomics Analysis

Spatial transcriptomics was conducted on human cancer samples, following approval by the Ethical Committees of the University of Trieste and Centro Cardiologico Monzino. Tissue sections were prepared by cutting 5 μm slices from formalin-fixed paraffin-embedded (FFPE) tissue blocks and mounting them onto Superfrost slides (Thermo Fisher).

The transcriptomic analysis was performed using the NanoString GeoMx Digital Spatial Profiling (DSP) platform in Seattle, WA, USA. This advanced technique allows for high-resolution gene expression profiling of specific tissue regions while preserving spatial context.

Tissue Preparation and Marker Selection

Tissue sections were stained with cell-type-specific markers to identify regions of interest (ROIs) for downstream gene expression analysis:

Troponin I: To label cardiomyocytes (CMs).

Pan-cytokeratin: To identify lung and colorectal cancer cells.

PMEL: To mark melanoma cells.

2.8.1. Selection of Regions of Interest (ROIs)

ROIs were carefully selected based on the following criteria:

Each ROI contained at least 300 cells of the target cell type to ensure robust transcriptomic analysis.

Areas with fibrosis or necrosis were systematically excluded to maintain the integrity and relevance of the sampled regions.

This approach ensures precise spatial mapping of gene expression patterns within the tumor microenvironment and cardiac tissues, enabling a detailed understanding of the cellular and molecular interactions in these contexts.

2.9. Video-Optical Recording and Analysis of EHT Contraction

The contractile activity of Engineered Heart Tissues (EHTs) was recorded using an Andor Neo sCMOS camera integrated into a Nikon Eclipse Ti microscope equipped with Plan UW objectives (1X or 2X). EHTs were maintained in a humidified incubator (OkoLab) set to 37°C and 7% CO_2 to preserve physiological conditions during live imaging. Recordings were performed for either 5 or 10 seconds at a high frame rate of 100 frames per second, ensuring sufficient temporal resolution for detailed analysis of contractility.

For stimulated contraction measurements, EHTs were subjected to electrical stimulation at a frequency of 4 Hz using a Hugo Sachs Elektronik Stimulator C Type 224, as previously described. This setup allowed precise assessment of both spontaneous and stimulated contractile activity under controlled experimental conditions.

To quantify contractile force, the deflection of the silicone posts anchoring the EHTs was measured. Using known geometric properties of the posts, the elastic modulus of Sylgard 184 silicone (2.6 kPa), and the post deflection distance, force was calculated based on a previously published equation:

$$F = \frac{3EI\delta}{L^3} = \frac{3\pi ER^4\delta}{4L^3}$$

where:

R: Radius of the post,

L: Length of the post,

E: Elastic modulus of the material,

δ: Measured post deflection,

I: Moment of inertia of the post, given by I=14R4I=41R4.

This equation provides a precise method for converting post deflection into force, enabling accurate quantification of mechanical properties and contractile performance of the EHTs.

This advanced imaging and analytical approach facilitates the study of mechanical dynamics and functional output in EHT models, contributing to our understanding of cardiac and cancer cell behavior under various biomechanical conditions.

2.10. Image Analysis

Image acquisition was conducted using a Nikon Eclipse Ti microscope equipped with an Andor Neo sCMOS camera. Quantitative analysis of acquired images was performed using ImageJ software (NIH, Bethesda).

2.10.1. DNA Compaction Analysis

To evaluate chromatin compaction, the coefficient of variation (CV) of DAPI intensity within individual nuclei was calculated. The CV was determined using the formula:

$$\mathrm{CV} = \frac{\sigma}{\mu}$$

where:

σ: Standard deviation of DAPI intensity values within the nucleus,

μ: Mean intensity value of the nucleus.

Highly condensed chromatin, characterized by bright chromocenters, results in a broader intensity distribution and a higher standard deviation, yielding a higher CV compared to decondensed heterochromatin, which displays more uniform DAPI staining.

2.10.2. Densitometric Analysis of H3K9me3 Intensity

The intensity of H3K9me3 staining was quantified through densitometric analysis. The integrated density of H3K9me3 staining was measured within nuclear regions of interest (ROIs) identified based on DAPI signal. This approach allowed precise quantification of histone methylation levels as an indicator of chromatin state.

2.10.3. Proliferating Cancer Cell Analysis

The number of proliferating cancer cells and the density of cancer cells within cross-sectional areas were calculated using the Cell Counter plugin in ImageJ. Proliferating cells were identified based on immunostaining for specific markers, such as Ki67 or phospho-Histone H3 (Ser10), and their nuclear localization was confirmed using DAPI counterstaining.

This comprehensive image analysis approach enables precise evaluation of chromatin organization, histone modifications, and cellular proliferation, providing valuable insights into the molecular and structural dynamics of cancer and cardiac cells within engineered tissue models.

2.11. Statistical Analysis

All results are presented as mean ± standard error of the mean (SEM). Statistical comparisons were performed using GraphPad Prism 6 software (GraphPad Software, La Jolla, California, USA).

Comparison of Two Groups: Student's *t*-test was applied to evaluate statistical differences between two groups.

Comparison of Multiple Groups: One-way ANOVA followed by Bonferroni's post-hoc test was used for comparisons between multiple sample groups and a single control group.

Comparison Across Multiple Independent Groups: Ordinary one-way ANOVA followed by Dunnett's multiple comparisons test was employed to analyze differences among multiple independent sample groups.

Statistical significance was determined based on the following *P* values:

$P \leq 0.05$ (*),

$P \leq 0.01$ (**),

$P \leq 0.001$ (***).

This rigorous statistical framework ensures reliable analysis of experimental data, enabling robust interpretation of the results.

3. Results

3.0. An in vivo heterotopic transplantation model to achieve cardiac unloading

Thanks to the experience gained at the Daniel Swarovski Research Laboratory in Innsbruck, and in particular to the expert surgical knowledge imparted to me by Ann-Vu Nguyen, I was able to dedicate myself to developing microsurgical techniques under stereoscopic guidance. This allowed me to successfully explant and subsequently transplant a murine heart from donor to recipient into the laterocervical anatomical site, specifically the jugular-carotid system of the animal.

Figure 3-01. Daniel Swarovski Forschungslabor – Innsbruck.

3.0.1. Procedural aspects developed during this experience and now considered crucial for the correct execution of the technique

3.0.1.1. During the Phase of Donor Explant

The initial stages focused on the correct, rapid, and exceedingly precise isolation of the ascending aorta and pulmonary artery, severing them to a sufficient (and necessary) length for subsequent implantation in the recipient animal. The tissue plane between the two vessels is extremely thin, almost virtual, and must be carefully separated through gentle and incremental dilations performed with specialized, very fine surgical forceps, as shown in the accompanying image.

Figure 3-02. Surgical instruments.

The aortic arterial wall is relatively robust and easily dissected from the surrounding tissues, whereas the pulmonary artery wall is softer and prone to retraction. Therefore, it is crucial to remain acutely aware of this difference during the pulmonary artery dissection phase to ensure the maximum possible length is harvested. During the final transplantation phase, this length will be a decisive factor in determining the ease or complexity of wrapping the prepared jugular cuff.

3.0.1.2. During the Phase of Vessel Preparation in the Recipient Animal

If, during the previous phase, each step is to be considered "important," in the subsequent phase, every detail of each step becomes critical for the outcome. The successful completion of the two anastomoses—aorto-carotid and pulmonary-jugular—must be achieved without any bleeding, ultimately resulting in a transplanted, beating heart (albeit without internal blood volume).

The positioning of the animal on the operating table is crucial: the mouse must be placed so that all four limbs are kept separated from the body. Specifically, a slight rotation of the animal's neck towards the left must be performed to expose the right laterocervical region as widely as possible.

Additionally, the traction applied to the thread holding the animal's teeth anchored to the upper part of the plate on which it rests serves as another method to orient and fully expose the right laterocervical area for the surgical procedure. Combined with the aforementioned considerations, this setup ensures optimal accessibility and visualization of the surgical site.

Preparation of the External Jugular Vein

The jugular vein is skeletonized and isolated first, as it is located on a more superficial plane. All venous collaterals draining into it—usually no fewer than five—are ligated and severed following cauterization. Particular attention must be paid to a larger collateral emerging from the posterolateral plane. In some cases, for a safer and more controlled section, it is advisable to ligate the vessel proximally and distally before cutting, rather than relying solely on cauterization.

Regarding the external jugular vein, its eversion onto the cuff is more accommodating in terms of length, owing to the slightly greater extensibility of venous tissue. This property facilitates the procedure and minimizes the risk of technical complications.

The most critical aspect of the vein cuffing phase is the precise identification of the lumen after severing the cranial ligature. For this step, the use of high-quality forceps with undamaged, sharp tips is highly recommended, as it ensures accurate handling and clean exposure of the vessel's lumen.

Figure 3-03. External jugular vein cuffing.

Traditional Method for Preparing the Common Carotid Artery

According to this traditional microsurgical method [58], the first step involves the sectioning of the sternocleidomastoid muscle, following extensive cauterization in order to prevent bleeding.

This step is performed to create a surgical window that provides access to the underlying planes. These planes contain the neurovascular bundle, which includes the common carotid artery and the vagus nerve. The bundle is located along the anteromedial aspect of the muscle and is enveloped in a delicate network of fibrous connective tissue trabeculae. By carefully sectioning the sternocleidomastoid muscle and exposing the neurovascular structures, this approach ensures precise and convenient visualization and access to the common carotid artery for subsequent procedures while minimizing the risk of damage to the surrounding anatomy.

Once the carotid artery has been identified, its separation from the thin venous branches surrounding it, and especially from the vagus nerve, is performed through careful blunt dissection. Subsequently, the vessel should be encircled from below in a medio-lateral direction using a blunt surgical clamp, and a ligature should be placed cranially, slightly proximal to its bifurcation (internal and external branches). By maintaining traction on the carotid artery using the pre-bifurcation ligature just applied, the artery is tied again one millimeter (at most two) more proximally, ensuring that it can then be sectioned between the ligatures.

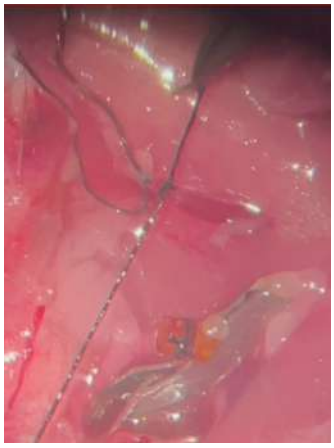

Figure 3-04. Proximal ligation 1-2 mm from the distal one, followed by sectioning.

Achieving a proper and well-skeletonized segment of the common carotid artery: thanks to the sectioning of the sternocleidomastoid muscle and the resulting space created, it is possible to extend the isolation down to the emergence of the common carotid artery from the muscle itself. Obtaining this length is essential to ensure a sufficient segment of the vessel that can be everted onto the cuff.

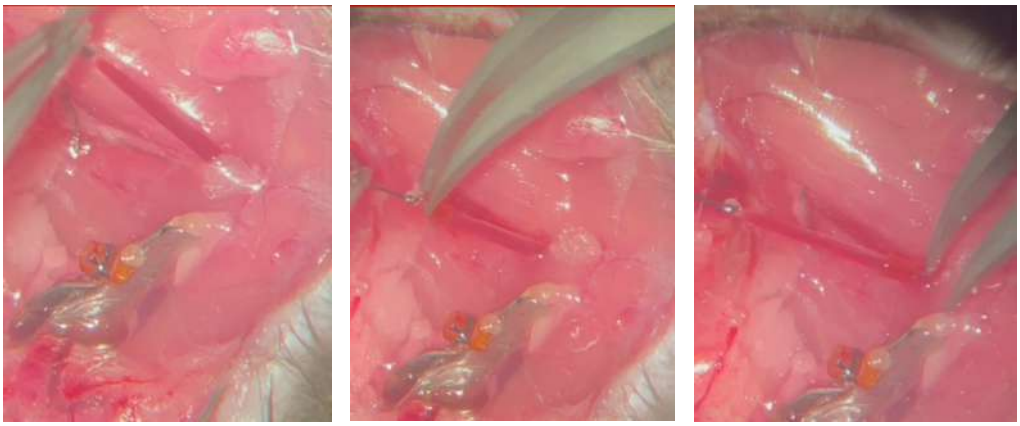

Figure 3-05. Achieving the correct length of the carotid segment through traction and tissue dissection from below.

The cuff is then inserted from above, using the proximal ligature thread as a guide, and slid along the body of the common carotid artery. The artery is clamped proximally to the cuff (at its flat portion) with a clamp that is more robust than the one used for the external jugular vein. The clamping must ensure not only that the length of the carotid artery is sufficient but also that the cuff remains unaltered in its flat portion.

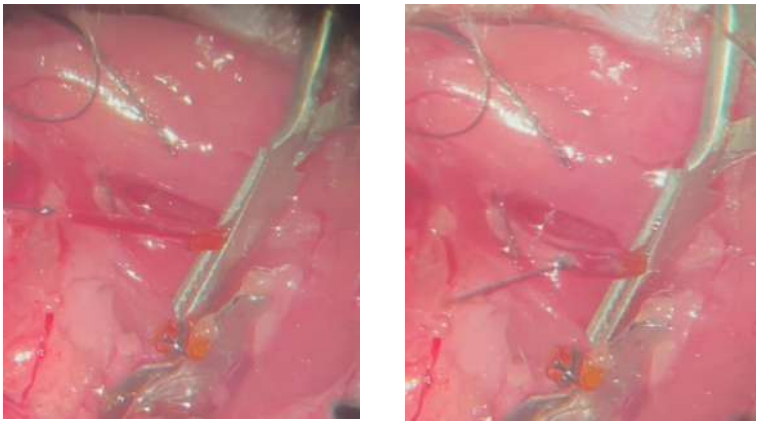

Figure 3-06. Clamping of the common carotid artery. Note the different length of the vessel after releasing it with the left clamp.

An additional critical step, which I learned directly during my experience in Innsbruck, involves securing the clamping component of the clamp under the skin on the medial aspect of the wound, first rotating it slightly upwards. This ensures stability and prevents movement when the carotid artery is everted onto the cuff. Furthermore, this technique aligns the eversion plane parallel to the microscope's field of view, facilitating precise visualization.

Figure 3-07. Clamping of the common carotid artery and upward rotation of the clamp to secure it under the animal's skin. Note the different position of the clamp compared to the previous arrangement.

Dilation of the common carotid artery is performed to facilitate its eversion onto the cuff

Using ultra-fine-tipped instruments, the vessel must be stabilized with the left hand while the right hand performs a modest dilation of the lumen to overcome the retractability of the most distal portion extending beyond the clamp.

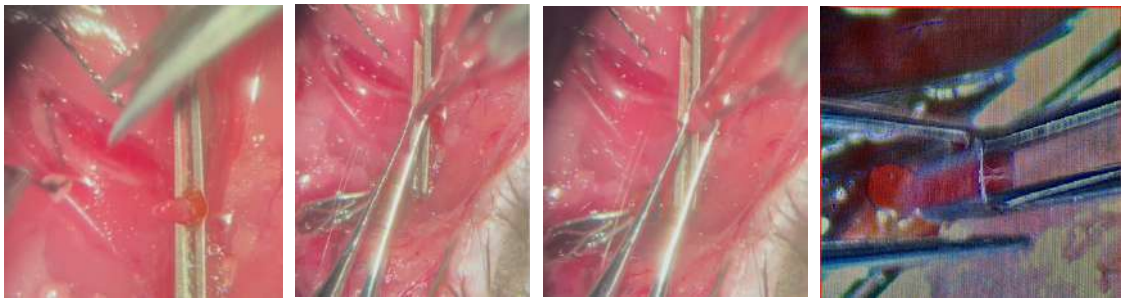

Figure 3-08. Manipulation and dilation of the common carotid artery to make it evertible onto the cuff.

This allows the lumen's rim to be securely grasped with two fine forceps and the vessel to be stretched downward to successfully perform the eversion maneuver. Once the vessel has been everted, the pre-prepared knot must be applied immediately, ensuring that it falls on the posterior plane of the cuff. This arrangement allows the second knot to be tied on the anterior plane, completing the process with precision and stability.

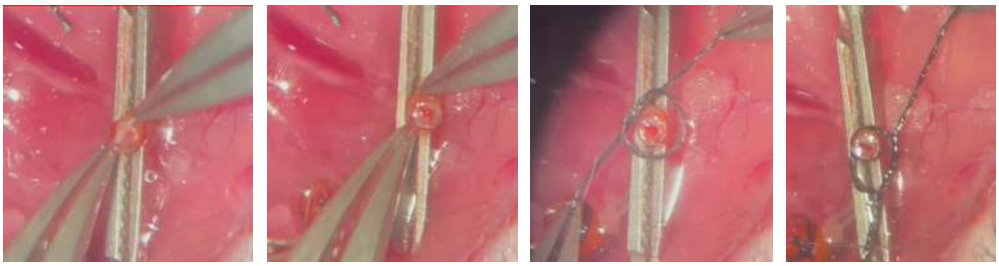

Figure 3-08. The most delicate phase of all: grasping the rim of the common carotid artery to invert it outward over the cuff. The clamp must remain in a stable position during this step. Stabilization with two knots (the first posteriorly, the second anteriorly).

The preparation of the common carotid artery carried out in this way will allow it to be wrapped with the donor ascending aorta segment, ensuring it is positioned below the knot securing the carotid artery to the cuff. From the outside, it will then be locked with an even more proximal knot, which will definitively hold together the aorta, the common carotid artery, and the cuff, thus establishing direct communication between the two lumens: that of the receiving common carotid artery and the donor ascending aorta.

3.0.1.3. During the Transplantation Phase on the Recipient Animal

This third and final phase addresses all the aspects considered previously during the heart explant and vessel preparation.

Placement and Anastomosis of the Donor Heart

The explanted heart is removed from the Custodiol solution, and a circular knot is prepared on the emergent section of the pulmonary artery. At this point, the heart is

positioned upside down on the operating field, so that the severed aorta and pulmonary artery face the common carotid artery and the external jugular vein, respectively. A key aspect of this phase is the focus of the microscope. It must be accepted that it is impossible to have the same focal plane for both the cuffed vessel and the donor vessel. It is necessary to bring the pulmonary artery as close as possible to the jugular vein so that the lumens of both vessels can be visualized, although not perfectly aligned.
At this point, the lumen of the pulmonary artery can be manipulated and pulled down to embrace the cuffed jugular vein. The prepared knot is then slid under the knot holding the jugular vein cuff in place (viewed through the wall of the pulmonary artery that encircles it) and tightened.

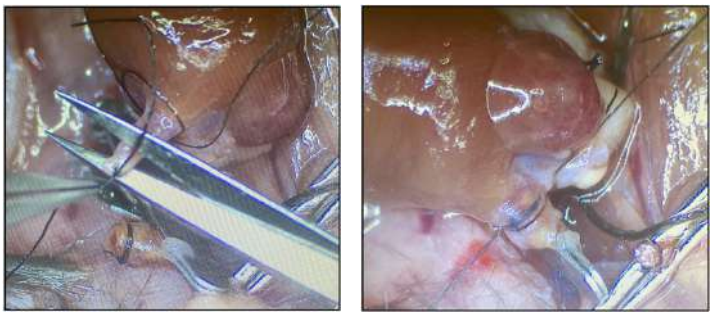

Figure 3-09. Pulmonary artery preparation and section (left). Pulmonary Artery - External Jugular Vein anastomosis (center). Note that the securing knot of the artery on the jugular cuff is placed beneath the knot holding the jugular vein to the cuff: this ensures a sealed anastomosis and guarantees hemostasis.

This pulmonary portion is more challenging due to the difficulty in identifying the lumen and establishing the correct orientation. The pulmonary artery has thinner, more collapsible walls compared to the common carotid artery, making the lumen less visible and harder to access. Proper traction and cuff wrapping may require more time than expected, as the surrounding tissues may adhere tightly or be fragile, requiring extreme precision to avoid damage to the pulmonary artery's wall.
The pulmonary artery is always anastomosed first. Subsequently, the aorta is anastomosed, in a similar manner, on the carotid artery, more medially.

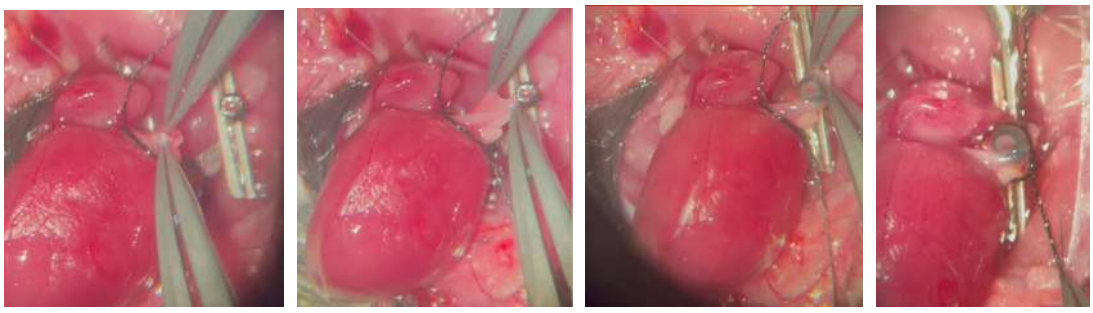

Figure 3-10. From left to right: lumen identification, downward traction, wrapping of the receiving vessel, and aorto-carotid anastomosis.

Great attention must be paid to avoid the two vessels crossing each other. The declamping is performed almost simultaneously and very gently, first removing the jugular clamp to create an outflow path, and then the carotid clamp to provide blood flow to the myocardial tissue and the right cardiac chamber, which can be drained directly through the jugular. The mitral floor does not allow blood to fill the left ventricle.

Essential Elements for Considering the Transplantation Successful

At declamping, it may take only a few seconds for the heart to appear vascularized. However, during this time, there should absolutely be no significant bleeding at the arterial or venous anastomotic sites. If some minor venous bleeding occurs, it can be controlled with gentle tamponade using a cotton swab while waiting for the heart to expand. As the heart begins to enlarge, the auricles start to swell, taking on a red-violet parenchymal appearance. The coronary vessels begin to become identifiable. At this point, the heart usually begins to contract as if it were pumping normally, though it is only being perfused through its myocardium, while the left ventricular chamber remains empty.

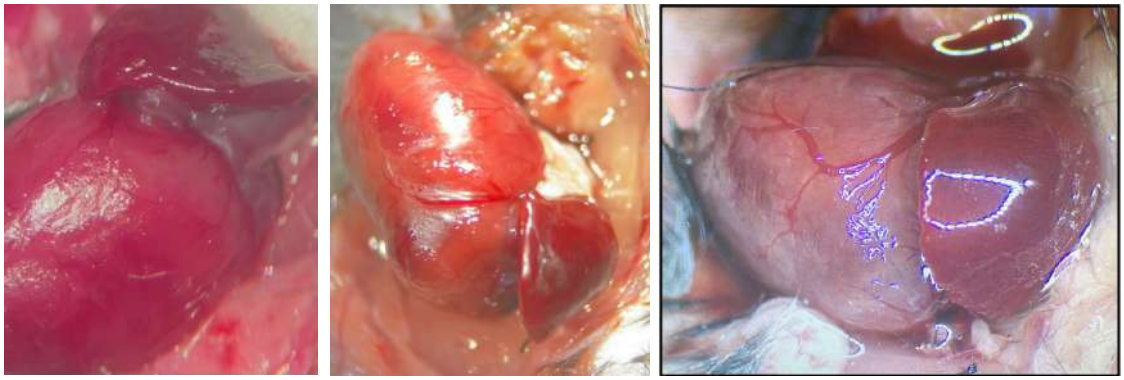

Figure 3-11. Myocardial perfusion upon declamping. Note the increase in volume and the vascularized appearance of the ventricle (coronary vessels) and atria. On the right, the heart cervically transplanted is contracting.

3.0.2. Personally developed improvements in carotid isolation

3.0.2.1. Minimally invasive carotid isolation

The sectioning of the sternocleidomastoid (SCM) muscle inevitably often caused bleeding from small vessels near the cauterized area, which required continuous control during subsequent phases. Furthermore, the muscle trauma induced by the sectioning of the SCM is significant, and despite optimal management through subcutaneous

analgesic injections in the immediate postoperative period and during monitoring, the animal could experience discomfort.
I considered avoiding the sectioning of the SCM by creating space between it and the sternothyroid muscle (located near the midline of the mouse's body) through blunt dissection. The right forceps should be used to medially separate the sternothyroid muscle while simultaneously creating a slit along the medial aspect of the vascular-nervous bundle, creating a breach between its delicate connective trabeculations. The left forceps should be used to carefully traction the belly of the SCM laterally, thereby creating the appropriate surgical window.

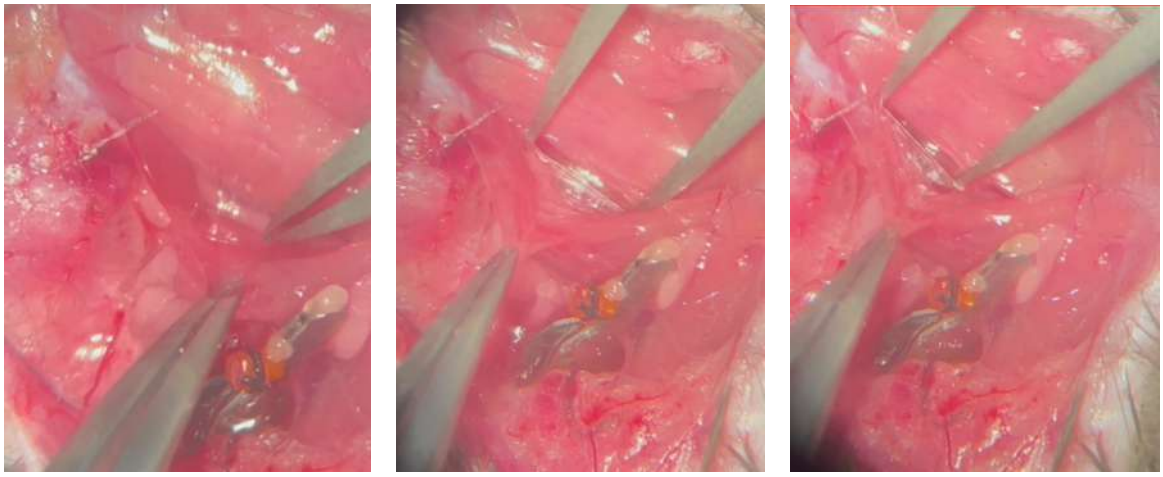

Figure 3-12. Blunt dissection and longitudinal separation of tissue planes between the medial aspect of the SCM (sternocleidomastoid) and the lateral aspect of the sternothyroid muscle.

The next step involves finding a plane to be obtained longitudinally, medial to the carotid artery, using right forceps to separate the structures. In this way, the structures can be gently detached without causing vascular or nerve damage (the vagus nerve runs postero-laterally to the common carotid artery).

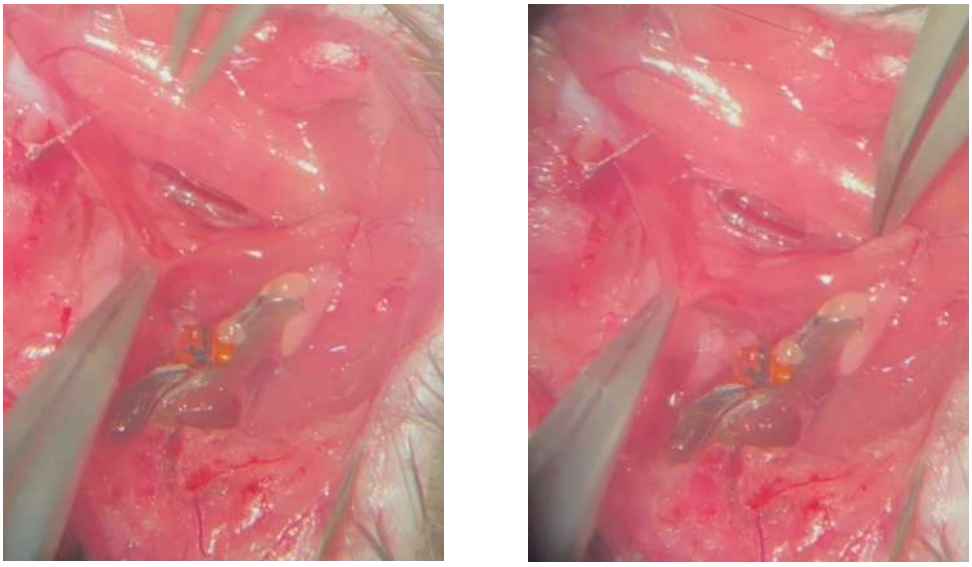

Figure 3-13. Creation of a vascular plane along the medial aspect of the vascular-nervous bundle. In the left image, note a thin, whitish longitudinal structure located laterally to the common carotid artery: the vagus nerve. It must be carefully separated from the artery and excluded from the subsequent ligation (as described earlier) to prevent postoperative digestive issues in the animal.

Once the vascular plane is lightly touched, the tip of the right forceps should be advanced slightly in depth, without losing sight of it, in a medio-lateral direction, while keeping the SCM in tension with the left forceps. At this point, the common carotid artery must be displaced from beneath, and only then, while keeping the tip of the forceps in sight (which should remain closed during this phase), can the tip be directed upwards along the lateral side of the carotid artery, gently spreading the forceps' tips to create space by breaking the thin connective trabeculae that bind it to the vagus nerve and the underlying planes.

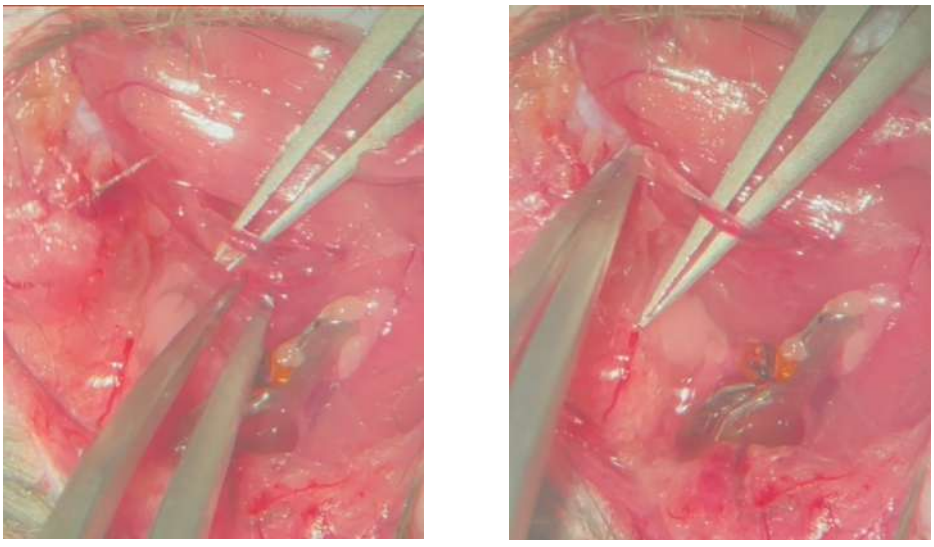

Figure 3-14. Isolation of the common carotid artery after detachment from below. At this stage, sparing the vagus nerve is crucial: it must remain in a postero-lateral plane, adhered to the underlying structures. Note that only at this point can the clamp held by the left hand release the medial side of the SCM.

With careful and successive spreading movements, more space can be created to isolate the artery and pass the first wire. At this point, the medial belly of the SCM can be released from the left forcep, and the procedure proceeds as described above.

3.0.2.2. Endpoints achieved through this Procedural Improvement

The minimally invasive isolation of the carotid artery, as described above, significantly impacts several key aspects of the surgical procedure.

1) First, there is a marked decrease in bleeding, particularly from small vessels near the cauterized area, minimizing the need for constant monitoring and hemostatic intervention. This avoidance of the sternocleidomastoid muscle sectioning not only streamlines the dissection but also reduces tissue trauma.
2) As a result, it notably reduces the overall operative time, with the isolation process taking approximately 5-10 minutes less compared to traditional method.
3) Furthermore, the technique leads to a better postoperative recovery for the animal, with a reduced incidence of pain and muscle-related discomfort. The refined approach enhances the overall success of the procedure by promoting quicker healing and lessened complication rates, contributing to a smoother recovery process.

3.1. Cardiac Unloading in Vivo Enhances Cancer Cell Proliferation

Cardiac metastases, while rare, are also typically smaller compared to extra-cardiac lesions, particularly in the case of hematogenous metastases within the myocardium. This observation is consistent even in patients with highly aggressive cancers that disseminate extensively to other organs. For example, in a case of aggressive uveal melanoma, the tumor exhibited widespread invasion of the liver and lungs but only minimal involvement of the myocardium (figure 3-1).

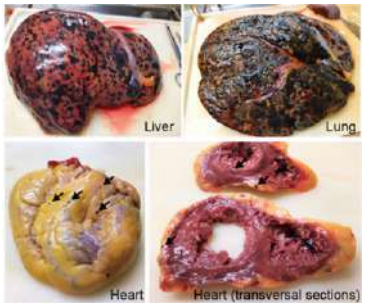

Figure 3-1. Gross appearance of en bloc resection of liver, lung and heart from a patient affected by a highly aggressive metastatic uveal melanoma. Black arrows indicate small metastatic spots mainly in the pericardial fat and minimally within the myocardium.

3.1.1. Mechanical unloading in vivo produces a significant increase in CM proliferation after one month

To investigate the potential role of mechanical load in the low incidence and limited growth of cancer in the heart, we employed an in vivo model of cardiac unloading through heterotopic heart transplantation. In this model, a donor heart is transplanted into the cervical region of a syngeneic recipient mouse, as schematically illustrated in Figure 3-2, the aorta and pulmonary artery of the donor heart are surgically connected to the carotid artery and external jugular vein of the recipient, respectively. This surgical configuration restores perfusion to the transplanted heart while eliminating mechanical load within the left ventricle (LV) [58-62].

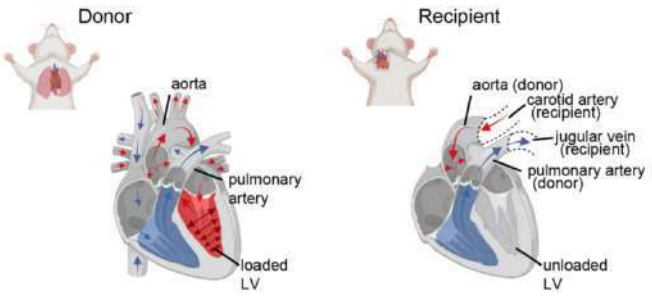

Figure 3-2. Schematic representation of the circulation following heterotopic heart transplantation. The heart is removed from the thorax of a donor mouse (left) and anastomosed to the neck vessels of a recipient mouse (right). In the transplanted heart, the oxygenated blood from the carotid artery bumps into the closed aortic valve and enters the coronary tree. The venous blood is drained back through the pulmonary artery into the jugular vein, in the absence of blood flow into the left ventricle (LV).

Cardiac unloading was confirmed by echocardiographic analysis, which demonstrated a marked reduction in key myocardial strain metrics, including velocity, displacement,

longitudinal strain, and strain rate, in the unloaded hearts compared to native hearts (Figure 3-3).

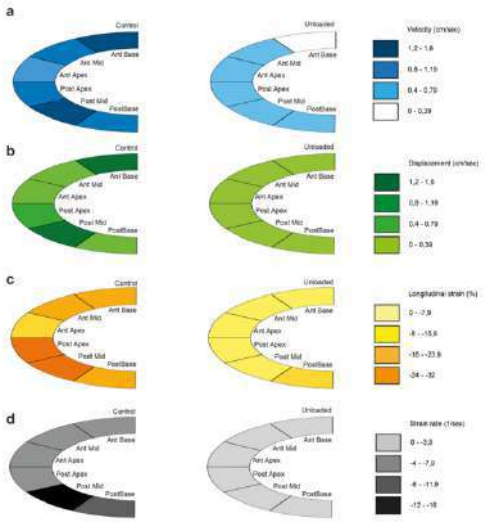

Figure 3-3. Graphical representation of regional velocity (a), displacement (b), longitudinal strain (c) and strain rate (d) of control and unloaded hearts.

These findings validated the efficiency of the unloading model in reducing cyclic mechanical stress within the myocardium. After one month of in vivo unloading, we observed a significant increase in the number of proliferating cardiomyocytes (EdU+ CMs) in the transplanted hearts. This result is consistent with previous evidence showing increased CM regeneration in human hearts mechanically unloaded through left ventricular assist device (LVAD) implantation [3], (Figure 3-4 and 3-5).

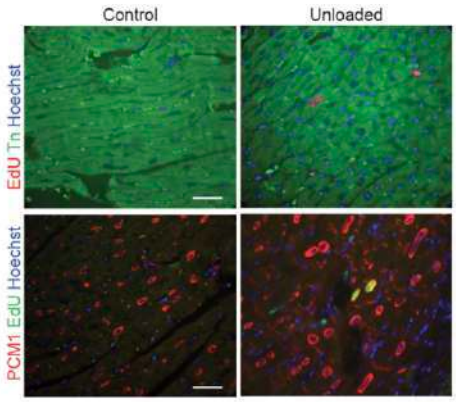

Figure 3-4. Representative immunofluorescence of control and unloaded hearts, in which CMs are stained for either troponin (Tn, upper panels) or the CM-specific nuclear marker pericentriolar material 1 (PCM 1, lower panels) antibodies. Proliferating nuclei are labelled by EdU incorporation. Scale bar: 50 µm.

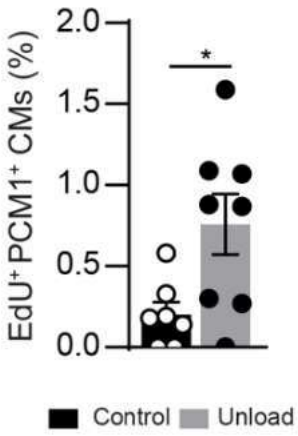

Figure 3-5. Quantification of EdU+PCM1+ proliferating CMs in control and unladed hearts.

To evaluate the impact of mechanical load on tumor cell proliferation, 1×10^5 LG1233 lung adenocarcinoma cells, stably expressing Green Fluorescent Protein (GFP), were injected intramyocardially into the LV of both native and unloaded hearts. Lung cancer was selected as the model due to its relatively high propensity to metastasize to the heart, particularly targeting the outer cardiac layers such as the epicardium and pericardium [8].

In native hearts, cancer cells exhibited limited growth, occupying less than 20% of the LV area two weeks after injection, consistent with previous findings. Conversely, in unloaded hearts, cancer cells proliferated extensively, infiltrating the myocardium and leading to an almost complete replacement of healthy cardiac tissue by two weeks post-injection (Figure 3-6 and 3-7).

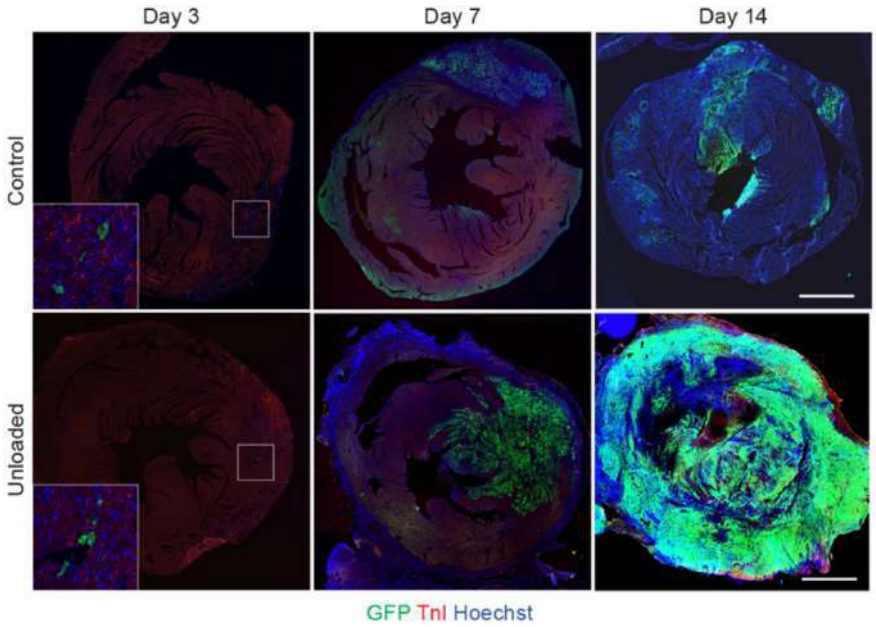

Figure 3-6. Transversal sections of control and unloaded hearts injected with LG1233 GFP+ cancer cells at the indicated time points. CMs are stained for Troponin I (TnI). Insets show high magnification images of engrafted cells at day 3.

.

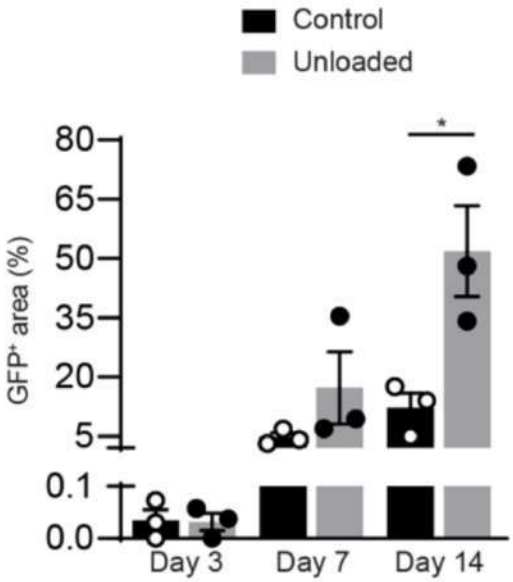

Figure 3-7. Quantification of the area occupied by GFP+ cancer cells in control and unloaded hearts at the indicated time points.

.

The enhanced proliferation of cancer cells in unloaded hearts was not attributable to differences in initial engraftment, as the number of GFP+ cells observed three days post-injection was comparable between the two groups (Figure 3-8, top). Analysis of cell death using TUNEL and cleaved Caspase-3 (cCASP3) staining revealed no GFP+TUNEL+ or GFP+cCASP3+ cells in either native or unloaded hearts at day 3, indicating that tumor size differences observed at day 14 were not due to differential rates of cell death (Figure 3-8, bottom).

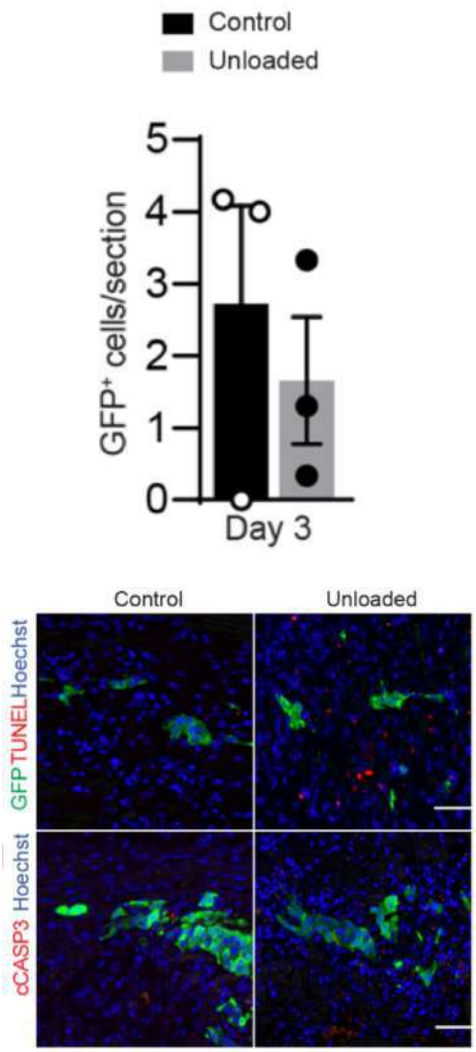

Figure 3-8. Quantification of GFP+ cancer cells in control and unloaded hearts at day 3 [top]. Representative images of control and unloaded hearts stained for TUNEL and GFP. Representative images of control and unloaded hearts stained for cleaved Caspase 3 (cCASP3) and GFP at day 3 [bottom].

3.1.2. Cancer cells grow very poorly in native hearts, but they massively infiltrate the unloaded ones

Cell proliferation was assessed by quantifying the number of cells positive for Ki67 and phosphorylated histone H3 (pHH3), which serve as markers for all active phases of the cell cycle and mitosis/late G2 phase, respectively. Analysis revealed a two-fold increase in the number of proliferating cancer cells in unloaded hearts compared to native hearts at both 7 and 14 days post-injection (Figure 3-9; 3-10; 3-11).

These findings demonstrate that lung cancer cells form larger tumor masses in mechanically unloaded hearts than in native hearts, and this difference can be attributed to an increase in cell proliferation under unloaded conditions.

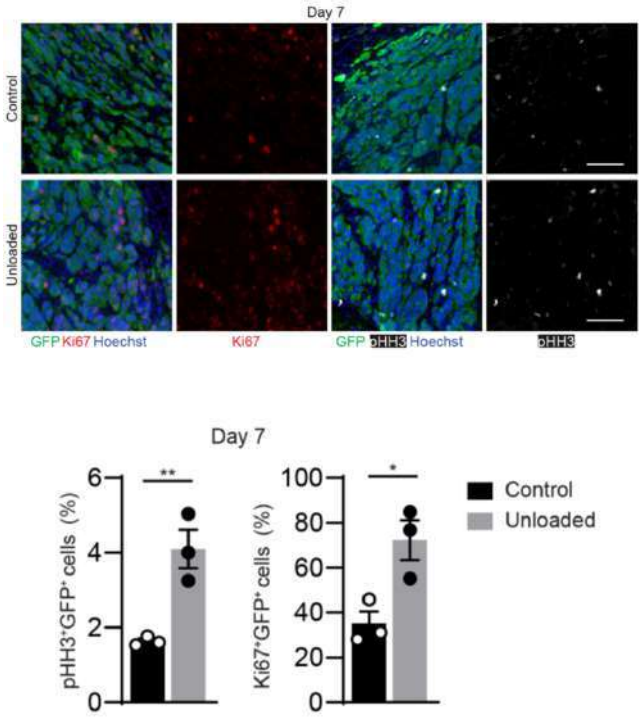

Figure 3-9. Representative images of control and unloaded hearts stained for the proliferation markers phospho-Histone H3 (pHH3) and Ki67, together with GFP, at day 7 (top). Quantification of pHH3+ and Ki67+ cancer cells in control and unloaded hearts at day 7 (bottom).

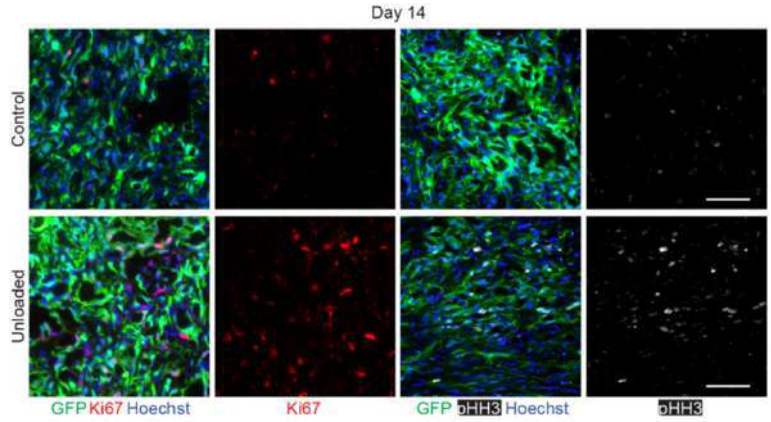

Figure 3-10. Representative images of control and unloaded hearts stained for the proliferation markers phospho-Histone H3 (pHH3) and Ki67, together with GFP, at day 7. Scale bar: 10μm.

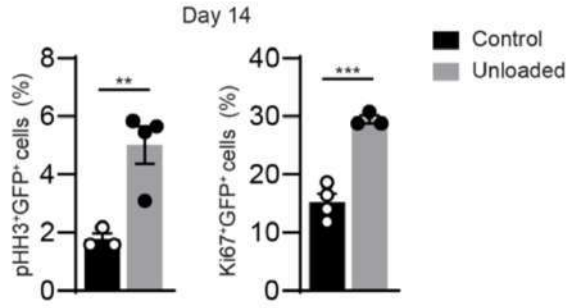

Figure 3-11. Quantification of pHH3+ and Ki67+ cancer cells in control and unloaded hearts at day 14.

3.2. Mechanical Load Modulates Cancer Cell Proliferation in Engineered Heart Tissues

To investigate the role of mechanical load on cancer cell proliferation in a controlled environment, the Engineered Heart Tissue (EHT) system was adapted to include neonatal rat cardiomyocytes (CMs) and fibroblasts. The setup was further modified by incorporating two adjustable metal braces that allowed precise regulation of mechanical load. By rotating these braces, the stiffness of the silicone posts anchoring the tissue could be increased to simulate conditions of elevated mechanical load. Alternatively, the braces could be adjusted to reduce the distance between the tissue's ends, effectively mimicking a mechanically unloaded state (Figure 3-12).

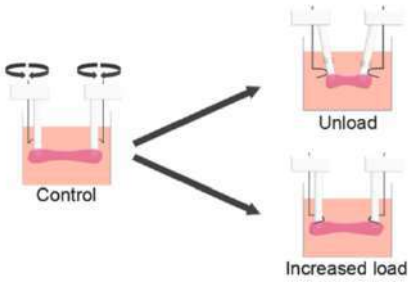

Figure 3-12. Schematic representation of control EHT (left) and its adaptation to induce either unload (top right) or increased load (bottom right).

To assess the suitability of EHTs for studying the effects of mechanical load variations on cell proliferation, experiments were first conducted on CMs.

3.2.1. Mechanical load affects CM proliferation and maturation in EHTs

Mechanical unloading led to an increase in CM proliferation at 3 days, as shown by EdU incorporation and the expression of proliferation markers Ki67 and phospho-histone H3 (pHH3) (Figure 3-13; 3-14; 3-15). These findings are consistent with the results observed in heterotopically transplanted hearts in vivo.

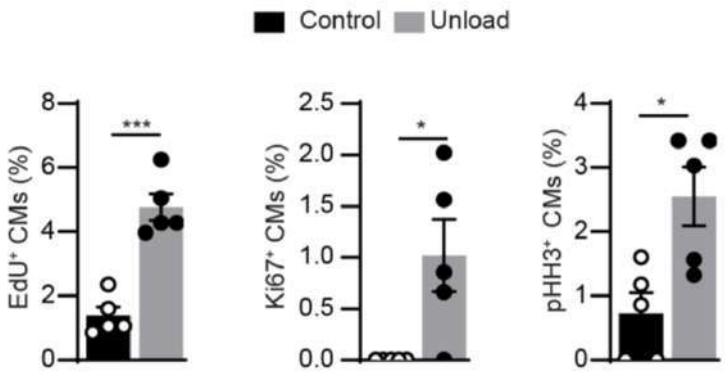

Figure 3-13. Quantification of CM proliferation in control and unloaded EHTs, assessed by EdU incorporation and staining for both Ki67 and phospho-histone H3

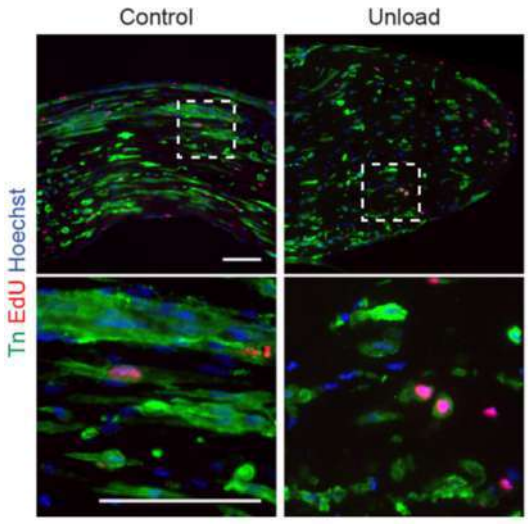

Figure 3-14. Representative immunofluorescence of control and unloaded EHTs in which CMs are stained for troponin (Tn) and proliferating nuclei are labelled by EdU. Lower panels are high magnification images of the dashed square drawn on upper panels.

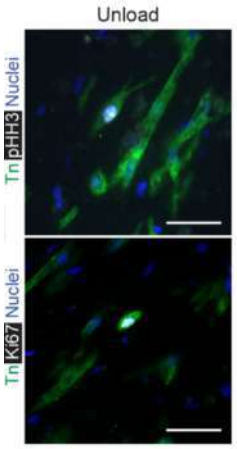

Figure 3-15. Representative immunofluorescence of an unloaded EHT in which CMs are stained for troponin (Tn) and proliferating nuclei for phospho-histone H3. d. Representative immunofluorescence of an unloaded EHT in which CMs are stained for troponin (Tn) and proliferating nuclei for phospho-histone H3. Representative immunofluorescence of an unloaded EHT in which CMs are stained for troponin (Tn) and proliferating nuclei for Ki67.

In contrast, prolonged mechanical loading for 2 weeks resulted in reduced CM proliferation, as indicated by Ki67 and pHH3 staining (Figure 3-16, top). EdU incorporation was slightly increased under conditions of elevated mechanical load (3-16, bottom left). However, the EdU+ nuclei primarily corresponded to bi-nucleated CMs (3-16, bottom right), which aligns with enhanced CM maturation.

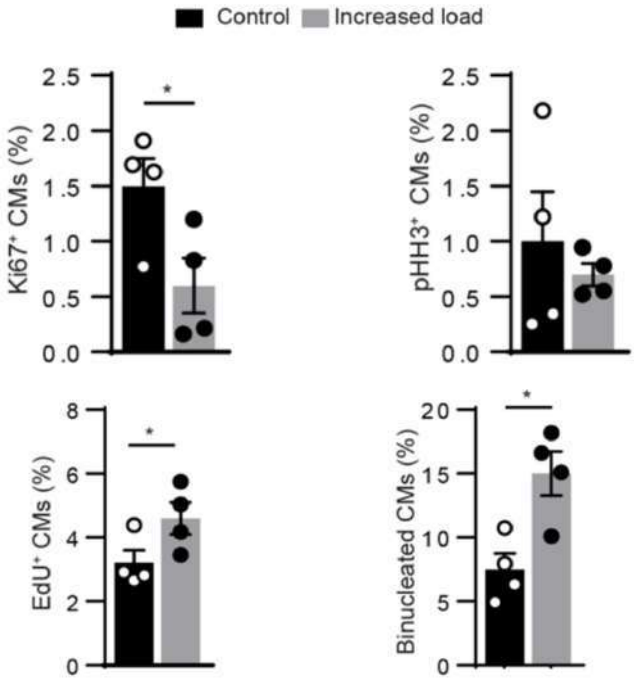

Figure 3-16. Quantification of CM proliferation in EHTs in conditions of control and increased overload, assessed by staining for Ki67 (top left) and phospho-histone H3 (top right). Quantification of EdU incorporation in EHTs in conditions

of control and increased overload (bottom left). Quantification of CM binucleation in EHTs in conditions of control and increased overload (bottom right).

This was further supported by a significant increase in CM cross-sectional area and contractile force under conditions of increased load (Figure 3-17).

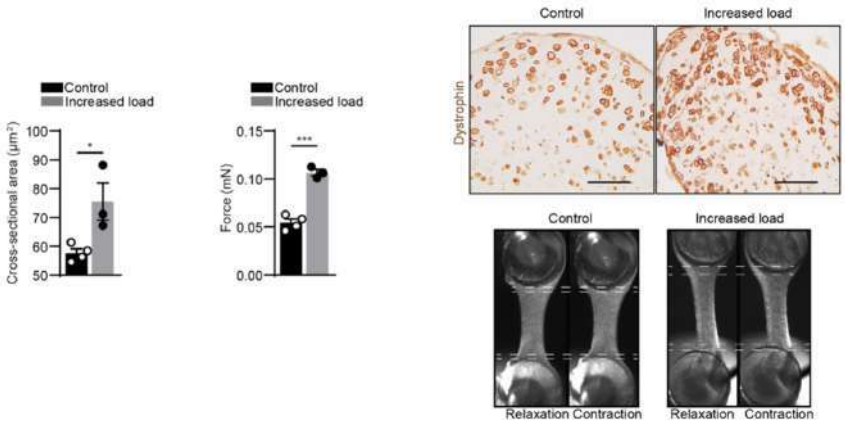

Figure 3-17. Quantification of CM cross-sectional area in EHTs in conditions of control and increased overload (left). Quantification of force generated by EHTs in conditions of control and increased overload (right). Representative immunohistochemistry of EHTs in conditions of control and increased overload, stained for dystrophin (right top). Representative images of EHTs in conditions of control and increased overload (right bottom) [white dashed lines indicate the displacement of silicon posts from relaxation to contraction].

These results indicate that mechanical unloading promotes CM proliferation, while increased mechanical load reduces proliferation and favors CM maturation.

3.2.2. Mechanical load regulates cancer cell proliferation in EHTs, which mimic the nature and magnitude of mechanical forces present in a functioning, beating heart

Engineered Heart Tissues (EHTs) were constructed incorporating GFP+ lung cancer cells (Figure 3-18).

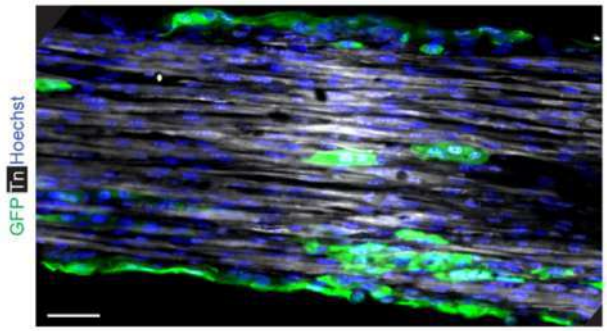

Figure 3-18. Representative immunofluorescence image of an EHT composed of both Troponin (Tn)+ CMs and GFP+ cancer cells.

After 7 days, a period sufficient for cardiomyocyte maturation and the establishment of synchronized contractions, the metal braces were adjusted to either reduce or increase the mechanical load for an additional 3-day period. Unloading conditions resulted in an increase in cancer cell proliferation within the EHTs, whereas increased loading conditions led to a reduction in their proliferation (Figure 3-19).

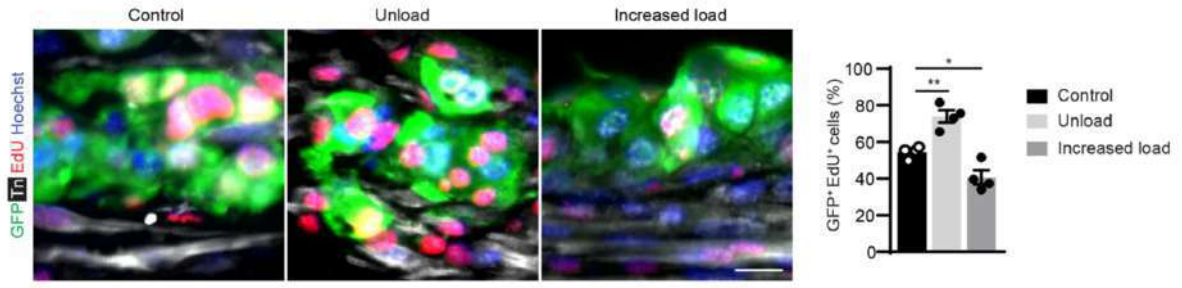

Figure 3-19. Immunofluorescence images of EHTs exposed to control load, unload and increased load, stained for GFP, Troponin (Tn) and EdU (left). Quantification of the percentage of proliferating EdU+ cancer cells in EHTs exposed to control load, unload and increased load (right).

These findings align with the results observed in vivo, where heterotopic heart transplantation (HHT) influenced cancer cell proliferation under unloaded conditions.

3.2.3. Validated quality of the EHT model

To assess whether the EHT system accurately replicates the primary mechanical forces present in a beating heart, mathematical simulations of cardiac mechanics were performed. Figure 3-20 illustrates an idealized rodent LV, where myofiber orientation transitions transmurally from the endocardium (+60°, shown in red) to the epicardium (-60°, shown in blue).

Figure 3-20. Simulated LV geometry and imposed fiber fields.

This LV model was simulated contracting under either a standard systolic cavity pressure or, in the unloaded condition, with no cavity pressure (Figure 3-21).

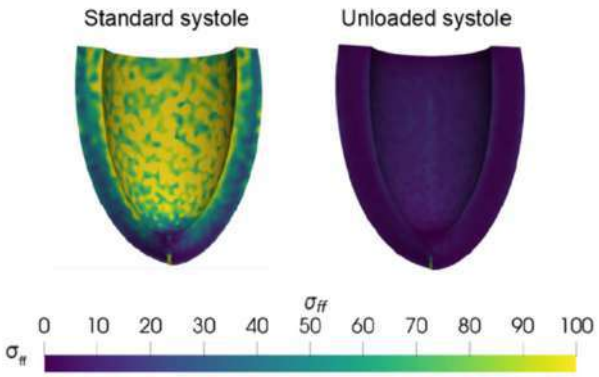

Figure 3-21. Graphical representation of end systolic fiber direction Cauchy stresses on the endocardial surface for a standard systolic load (15 kPa) and in the absence of load.

The removal of pressure significantly reduced calculated stress magnitudes across all three principal directions: the myofiber direction (σff), the sheet-aligned direction (σss), and the normal direction (σnn) (Figure 3-22). These results align with the strain parameters obtained experimentally, as shown in Figure 3-3.

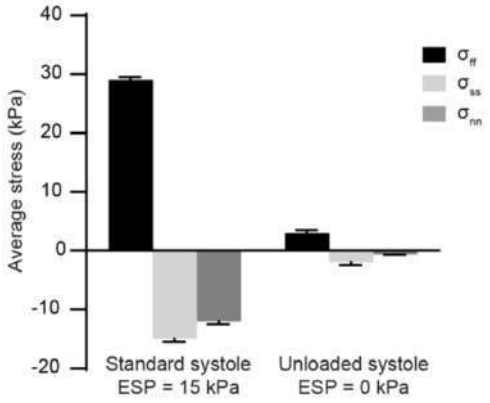

Figure 3-22. Calculated average peak stress in the fiber (σff), cross fiber (σss) and cross sheet direction (σnn) in the myocardium for standard and unloaded simulations.

A model was then developed to represent the EHT, assuming a cylindrical geometry. The contraction of the EHT was simulated against a spring constant that closely approximates the experimentally measured contraction at peak systole (~15%), as depicted in Figure 3-23. Mechanical stresses were computed for the three configurations described in Figure 3-12: standard contraction (control), unloaded, and increased load conditions. As shown in Figure 3-23, the EHT exhibited stress patterns consistent with those observed in the LV simulation, particularly for fiber-aligned stresses (σff) and

orthogonal normal stresses, both circumferential (σc) and radial (σr). Increasing the mechanical load resulted in a marked rise in the magnitude of all stress components, whereas stresses were largely absent under unloaded conditions.
These findings demonstrate that mechanical load modulation in EHTs effectively mirrors the effects observed during cardiac unloading in vivo. Additionally, the modulation of mechanical forces in both systems results in comparable outcomes on the proliferation of both cardiac and cancer cells.

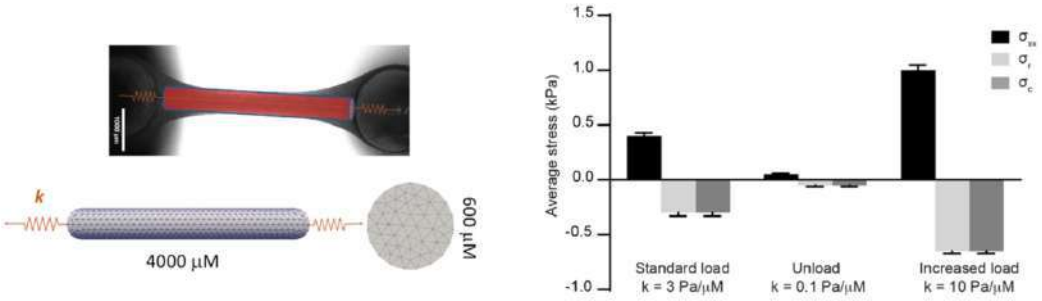

*Figure 3-23. EHT cylindrical geometry and imposed Robin boundary conditions for finite element method (FEM) simulation (left). Calculated average EHT stress in standard conditions, and in unloaded and increased load conditions, via altering Robin boundary stiffness (right). Scale bar:100μm in **b**;20μm in **c**.*

3.3. Cancer cells preferentially grow in EHT regions exposed to low mechanical pressure

3.3.1. Calcium addition to obtain beating EHT systems

3.3.1.1. GFP+ cancer cells grew significantly more and occupied a larger area in static than beating EHTs

The unloading system for EHTs described in Figure 3-12 is not suitable for long-term experiments, as tissues subjected to unloading undergo extensive remodeling and lose their original 3D structure over time. To investigate the effects of prolonged cardiac unloading on cancer cell growth, an alternative model was used in which cardiomyocyte contractility was controlled by the presence or absence of calcium in the culture medium. GFP+ lung cancer cells were incorporated into EHTs cultured in either calcium-free medium (static EHTs) or calcium-containing medium (beating EHTs), as illustrated in Figure 3-24. Consistent with prior observations, GFP+ cancer cells exhibited significantly greater growth and occupied a larger area in static EHTs compared to beating EHTs, as demonstrated and quantified in Figure 3-24 and 3-25 for whole tissues and in Figure 3-26 and 3-27, for cross-sectional analysis.

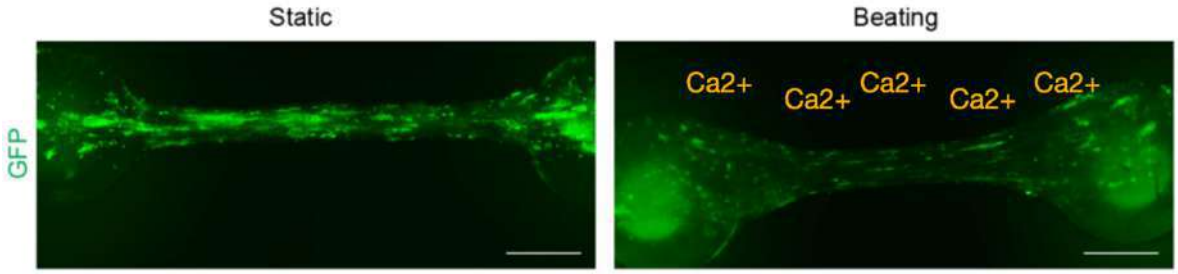

Figure 3-24. Representative low magnification images of EHTs composed by both CMs and LG1233 GFP+ cancer cells, cultured in the absence (static) or presence (beating) of calcium.

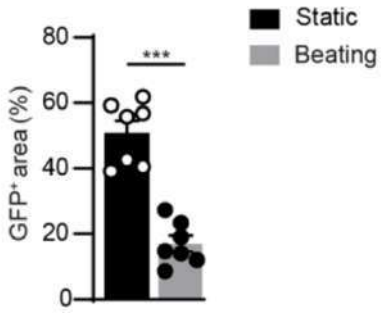

Figure 3-25. Quantification of the area occupied by LG1233 GFP+ cancer cells in static and beating EHTs.

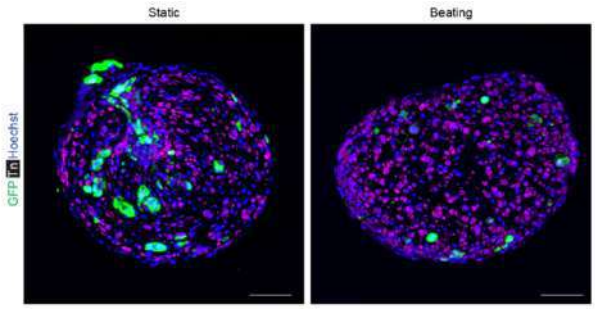

Figure 3-26. Representative cross-sections of static and beating EHTs stained for Troponin (Tn) and GFP.

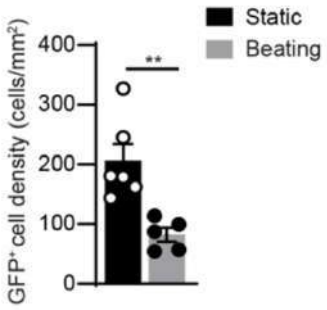

Figure 3-27. Quantification of LG1233 GFP+ cancer cell density in static and beating EHTs.

This difference was accompanied by a notable reduction in cancer cell proliferation in beating EHTs (Figure 3-28 and 3-29).

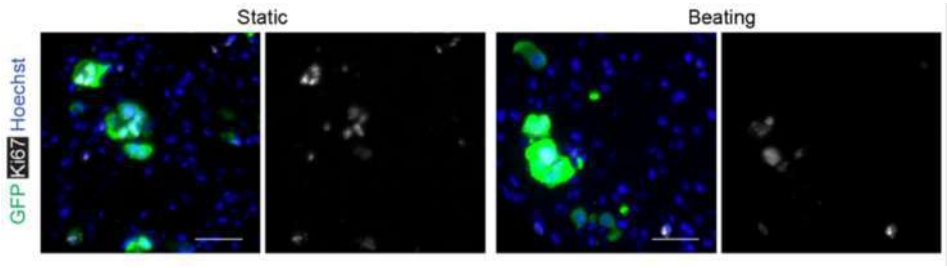

Figure 3-28. Representative immunofluorescence staining of static and beating EHTs stained for Ki67 and GFP.

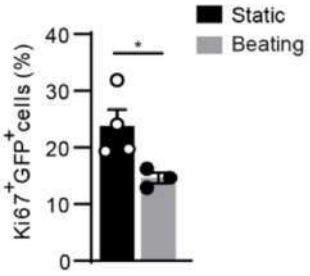

Figure 3-29. Quantification of Ki67+ proliferating LG1233 GFP+ cancer cells in static and beating EHTs.

Figure 3-30 confirms that the absence of calcium did not affect the proliferation of LG cells cultured in standard 2D conditions.

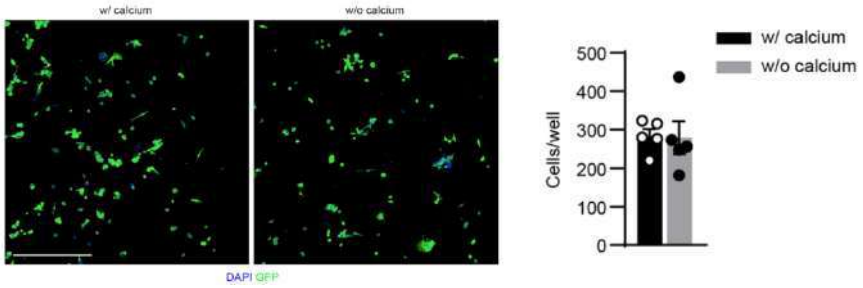

Figure 3-30. Quantification of the number of LG1233 cells after 5 days of culture in EHT medium with or without calcium supplementation (left). Representative images of LG1233 cells cultured in EHT medium with or without calcium supplementation (right). Scale bar: 100 µm.

3.3.1.2. In beating EHTs, cancer cell density forms a gradient that is inversely related to the gradient of hydrostatic pressure

Cancer cells were found to preferentially localize in the outer layers of beating EHTs, avoiding the central regions, while in static EHTs, they were evenly distributed throughout the tissue (Figure 3-26). Using the simulated EHT model presented in Figure 3-31 (right), the beating EHT was analyzed along the radial direction over a full simulated twitch. This analysis considered the higher density of myocytes in the outer layers of the EHT, as observed microscopically. The simulation results, shown in Figure 3-31 (left), indicated elevated hydrostatic pressure in the internal regions of the EHT at peak systole. Quantification of cancer cell distribution across multiple concentric layers within each EHT confirmed an even distribution in static EHTs. In contrast, in beating EHTs, cancer cell density displayed a gradient that inversely correlated with the gradient of hydrostatic pressure (Figure 3-32), suggesting that increased compressive forces in the central regions of the tissue inhibit cancer cell proliferation.

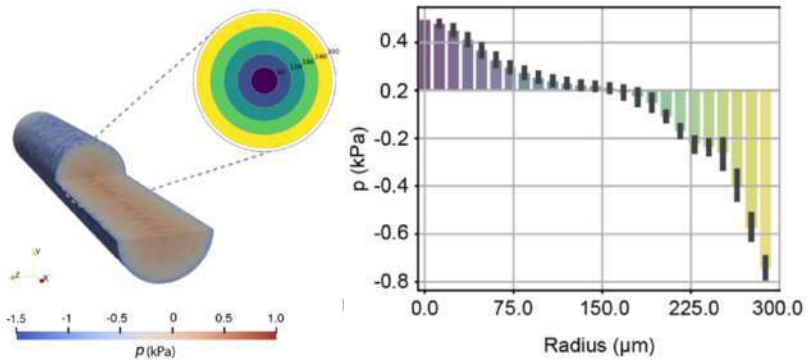

Figure 3-31. Graphical depiction of calculated hydrostatic pressure throughout the simulated EHT at peak systole with inset showing the cross section divided into 5 radial layers for reference (left). Quantification of simulated hydrostatic pressure as a function of radial distance from the centerline of the modelled EHT (right).

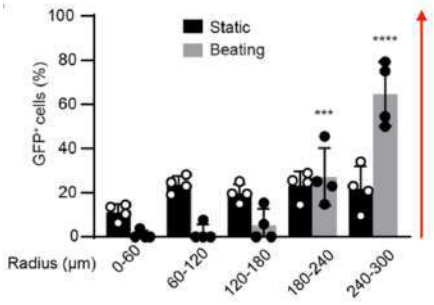

Figure 3-32. Distribution of GFP+ cancer cells in the radial layers depicted in g. Scale bar: 1mm in a,100μm in c, 50μm in e

.

These findings indicate that both mechanical load and the compressive forces generated by cardiomyocyte contraction play a significant role in reducing cancer cell proliferation within EHTs.

3.4. Transcriptome analysis on human cardiac cancer cells

3.4.1. The most highly overexpressed genes in cardiac metastases belong to the "Histone demethylation" enzymatic pathway

To investigate the molecular mechanisms through which cancer cells detect mechanical stimuli in the beating heart and translate them into reduced cell proliferation, we analyzed the transcriptional profile of cancer cells that naturally grow in the myocardium, specifically within human cardiac metastases. Samples were obtained from patients with three distinct primary tumors (lung adenocarcinoma, colon carcinoma, and cutaneous melanoma) that had metastasized to both the heart and other organs, as illustrated in Figure 3-33. Using spatial transcriptomics with GeoMX technology, cancer cells were identified based on specific markers: anti-pan-cytokeratin antibodies for lung and colon carcinoma cells, and anti-PMEL antibodies for melanoma cells (Figure 3-34). The transcriptional profiles of cancer cells in cardiac metastases were compared with those from extra-cardiac sites, including primary tumors and non-cardiac metastases.

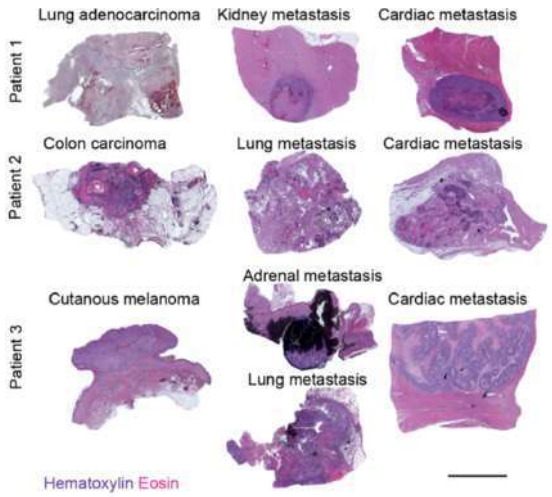

Figure 3-33. Hematoxylin/eosin staining of primary cancers that disseminated to both the heart and extra- cardiac sites.

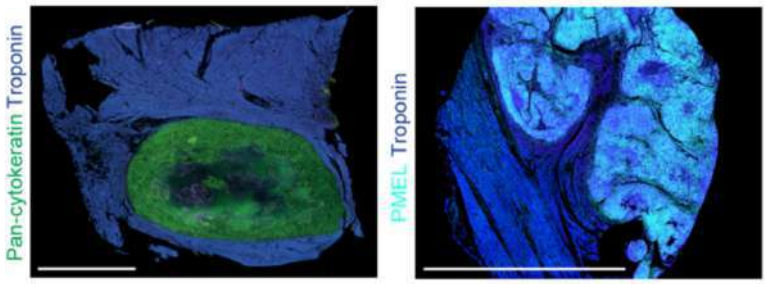

Figure 3-34. Representative immunofluorescent staining of cardiac metastases, in which carcinoma cells are stained for pan-cytokeratin, melanoma cells for PMEL and CMs for Troponin.

Unsupervised hierarchical clustering, based on the most differentially expressed genes (DEGs, n = 1753, ANOVA P < 0.01), revealed a shared transcriptional profile among cardiac metastases, irrespective of the tumor's origin (Figure 3-35, left). Gene ontology analysis identified "Histone Demethylation" as the most enriched pathway in cardiac metastases, characterized by the highest number of DEGs and the most significant upregulation of associated genes (Figure 3-35, right).

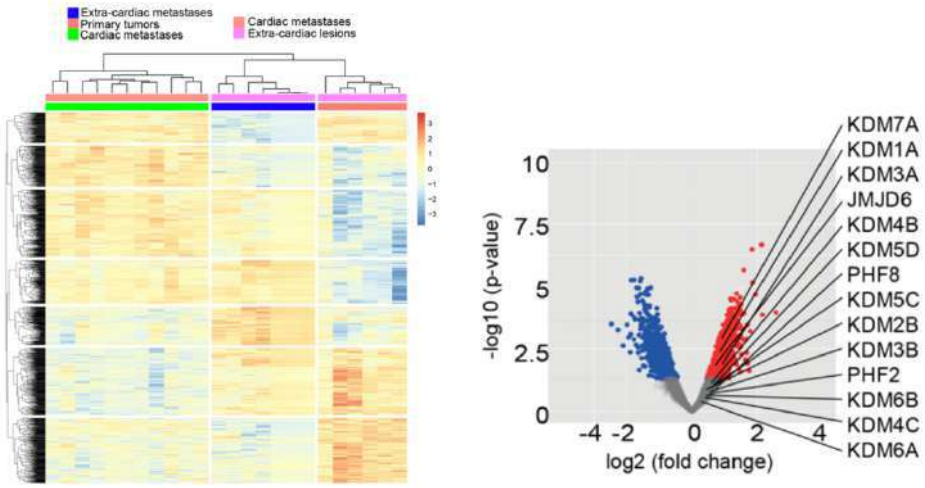

Figure 3-35. Heatmap showing unsupervised clustering based on most differentially expressed genes. Gene expression level was expressed as normalized value after row standardization and displayed as gradient colors from higher (dark red) to lower (dark blue) – [left]. Volcano plot of differential gene expression analysis, comparing cardiac metastases and extra-cardiac metastases, with indication of the most upregulated genes belonging to the Histone Demethlyation pathway in cardiac metastases. The log2(fold-change) and the -log10(p-value) are represented in x-axis and y-axis, respectively. Red and blue dots denote genes significantly overexpressed or silenced in cardiac metastases, respectively (p < 0.05), while grey dots represent genes without difference in expression between the two groups [right].

3.4.2. The levels of H3K9 tri-methylation were lower in the nuclei of cardiac metastases compared to those detected in extra-cardiac metastases

In line with the observed upregulation of multiple histone demethylases, the levels of H3K9 tri-methylation were found to be reduced in the nuclei of cancer cells within cardiac metastases when compared to those in primary tumors and extra-cardiac metastases (Figure 3-36 and 3-37).

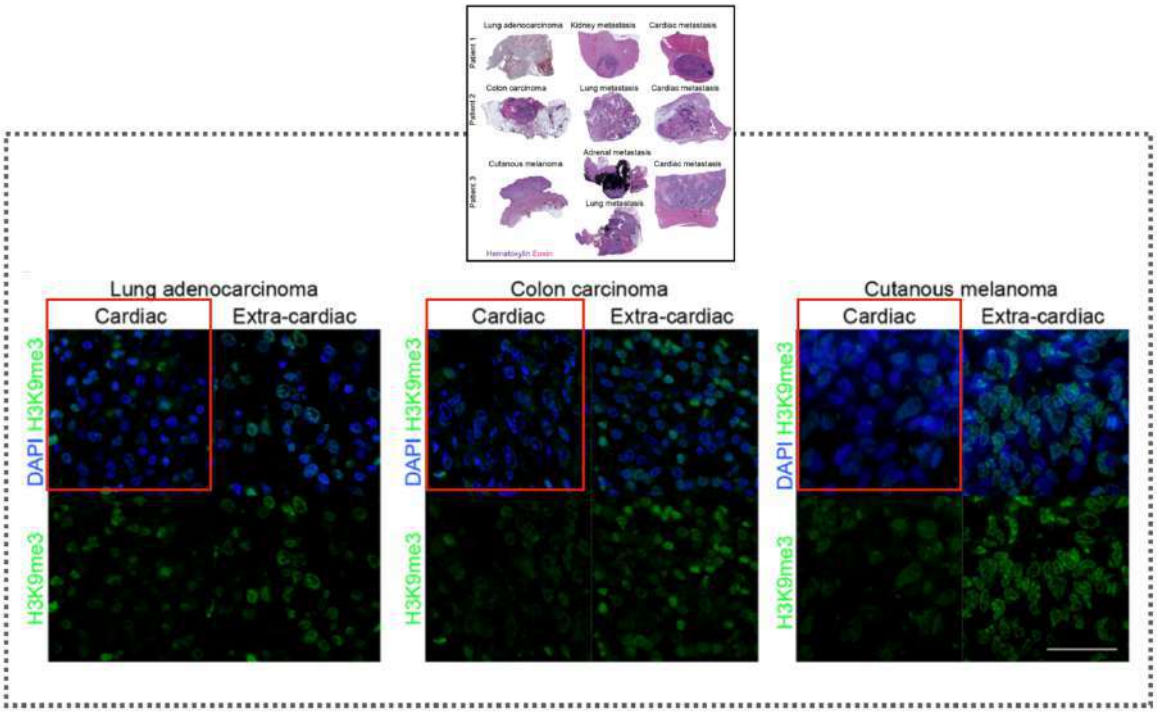

Figure 3-36. Representative images of H3K9me3 in the nucleus of cardiac and extra-cardiac lesions from the samples analyzed by spatial transcriptomics.

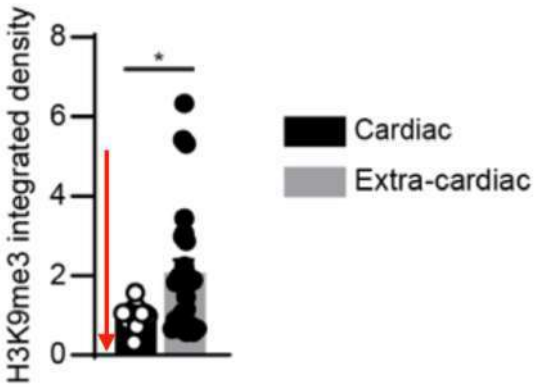

Figure 3-37. Quantification of the levels of H3K9me3 in the nucleus of cardiac and extra-cardiac lesions from the samples analyzed by spatial transcriptomics.

3.4.3. The chromatin state results less compact in cardiac metastases than in extra-cardiac lesions

The observed reduction in H3K9 tri-methylation levels was accompanied by changes in chromatin organization, with chromatin appearing less compact in cardiac metastases compared to extra-cardiac lesions. As illustrated in Figure 3-38 and 3-39, the coefficient of variation (CV) of DNA compaction, a standard metric for evaluating chromatin condensation [63-65], was significantly lower in cardiac metastases than in extra-cardiac lesions.

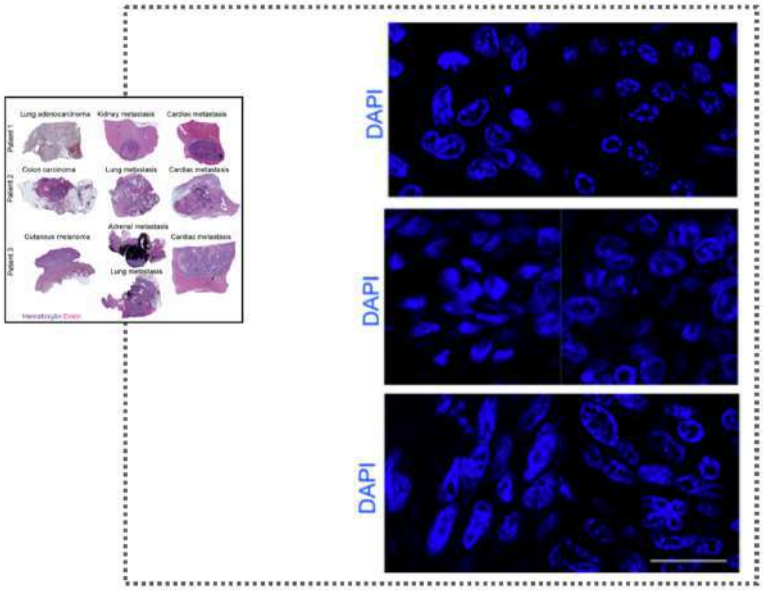

Figure 3-38. Representative images of chromatin compaction in the nucleus of cardiac and extra-cardiac lesions from the samples analyzed by spatial transcriptomics. Scale bar: 20µm.

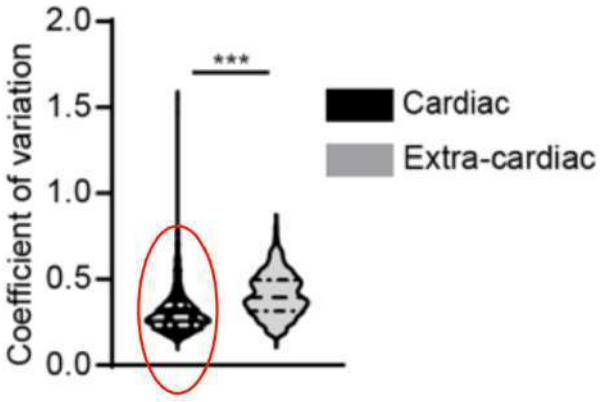

Figure 3-39. Coefficient of variation calculated based on the DAPI fluorescent images represented (top).

These findings indicate that cancer cells located in the human heart exhibit increased expression of histone demethylases, leading to decreased H3K9 tri-methylation levels and reduced chromatin compaction.

3.5. The effect of mechanical load on chromatin

To confirm the impact of mechanical load on histone methylation and chromatin structure, we examined these parameters within our experimental models of cardiac unloading.

3.5.1. Assessing the H3K9me Level and Chromatin Compaction in our Experimental Models In Vivo

3.5.1.1. H3K9me Level

Initially, we analyzed histone methylation in both native and unloaded hearts, observing that cardiac unloading led to a notable increase in H3K9 tri-methylation levels (Figure 3-40).

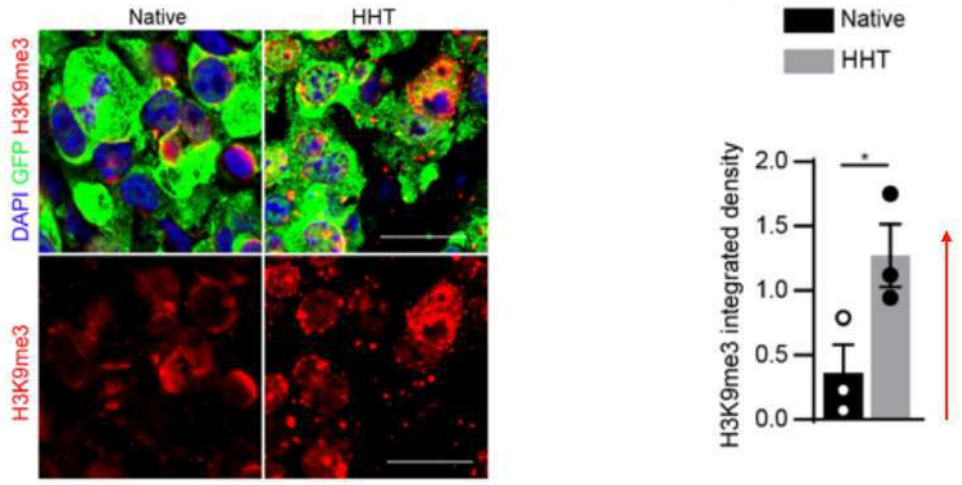

Figure 3-40. Representative images (left) and quantification (right) of H3K9me3 in the nucleus of LG1233 GFP+ cancer cells in native hearts and in hearts unloaded by heterotopic transplantation.

3.5.1.2. Chromatin Compaction

This increase was accompanied by enhanced chromatin compaction (Figure 3-41).

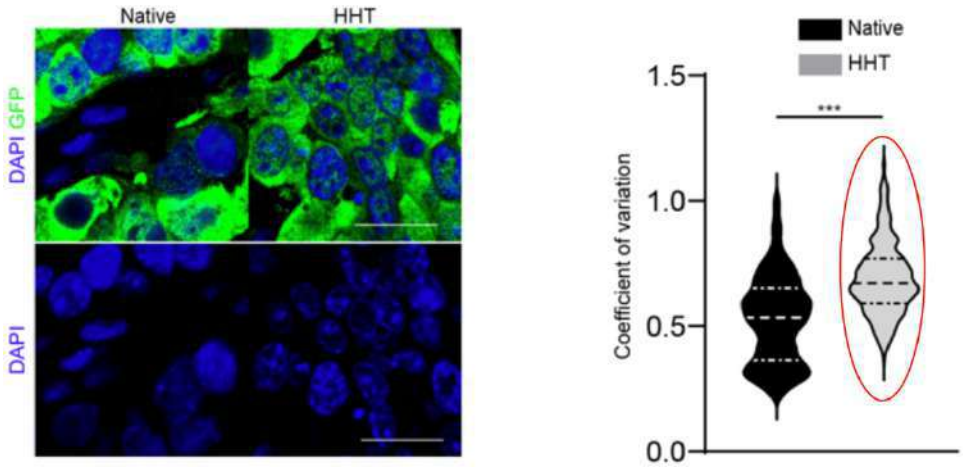

Figure 3-41. Representative images (left) and quantification (right) of chromatin compaction by DAPI staining of LG1233 GFP+ cancer cells in native hearts and in hearts unloaded by heterotopic transplantation.

3.5.2. Assessing the H3K9me Level and Chromatin Compaction in our Experimental Models Ex Vivo

3.5.2.1. H3K9me Level

Subsequently, we examined beating and static EHTs, finding elevated levels of H3K9 tri-methylation under static conditions compared to beating EHTs (Figure 3-42).

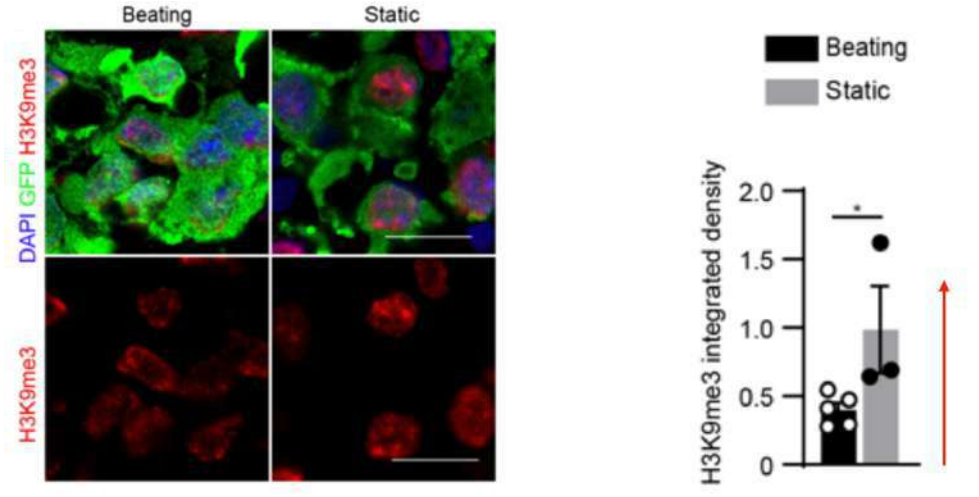

Figure 3-42. Representative images (left) and quantification (right) of H3K9me3 in the nucleus of LG1233 GFP+ cancer cells in static and beating EHTs.

3.5.2.2. Chromatin Compaction

We also observed a significant chromatin compaction under static conditions (Figure 3-43).

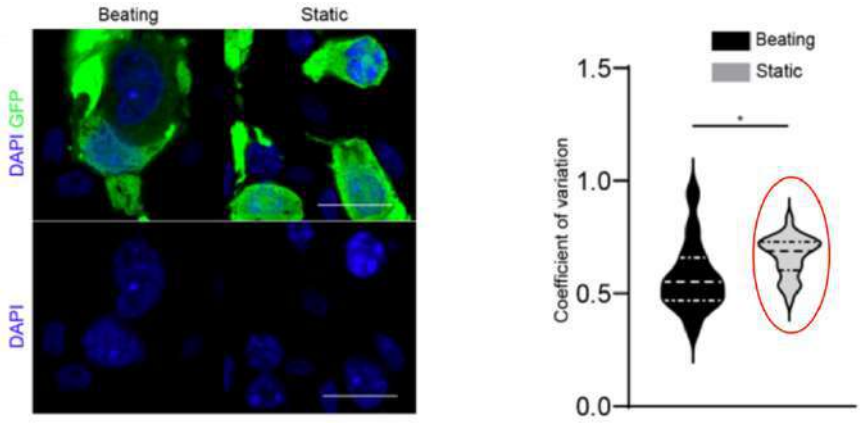

Figure 3-43. Representative images (lesft) and quantification (right) of chromatin compaction by DAPI staining of LG1233 GFP+ cancer cells in static and beating EHTs.

To determine whether H3K9 tri-methylation is not only associated with but also causally linked to cancer cell proliferation, we silenced the main lysine-specific demethylases (KDMs) that target H3K9 and were found to be upregulated in human cardiac metastases. The silencing of KDM4C, KDM4D, or both in combination, in LG1233 cells prior to their incorporation into EHTs, led to an increase in the area occupied by GFP+ cancer cells and an elevated density of LG1233 cells within beating EHTs (Figure 3-44).

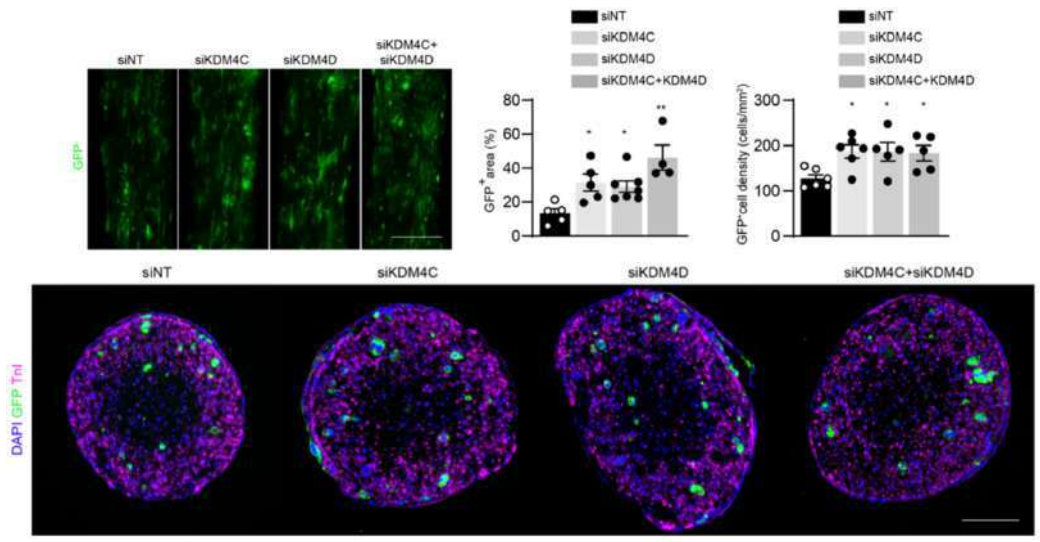

Figure 3-44. Representative low magnification images of EHTs containing LG1233 GFP+ cancer cells treated with the indicated siRNAs (top, left). Quantification of the area occupied by LG1233 GFP+ cancer cells upon treatment with the indicated siRNAs (top, center). Quantification of the density of LG1233 GFP+ cancer cells in EHT cross-sections, upon treatment with the indicated siRNAs (top, right). Representative cross-sections of EHTs containing LG1233 GFP+ cancer cells treated with the indicated siRNAs (bottom). Scalebar: 300µm (top, left),100 µm (bottom).

3.6. Does the LINC complex play a role?

Mechanical forces can influence chromatin condensation through specific mechanotransduction pathways. One such key mechanotransducer is the Linker of Nucleoskeleton and Cytoskeleton (LINC) complex, which consists of four Nesprin proteins and two Sun proteins [66]. To determine whether components of the LINC complex are necessary for cancer cells to detect mechanical load and mediate its effects on cell proliferation, we silenced each LINC complex member individually using specific siRNAs in LG1233 cells and evaluated their proliferation within beating EHTs.

3.6.1. Silencing LINC Members with Specific siRNA

3.6.1.1. Silencing of both Nesprin-2 and Nesprin-4 significantly increased the area occupied by LG1233 cells

As illustrated in Figure 3-45, the silencing of Nesprin-2 and Nesprin-4 led to a notable increase in the area occupied by LG1233 cells.

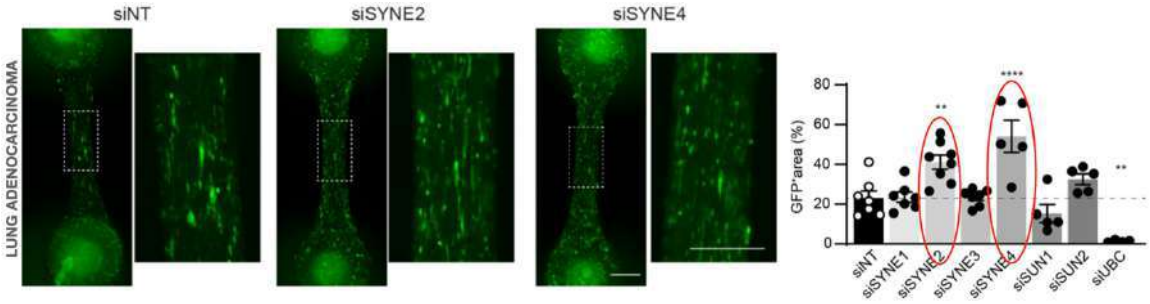

Figure 3-45. Representative low magnification images of EHTs containing LG1233 GFP+ cancer cells treated with the indicated siRNAs. A higher magnification of the squared region is shown on the right for each EHT (left). Quantification of the area occupied by LG1233 GFP+ cancer cells upon treatment with the indicated siRNAs (right). Scale bar: 300 µm.

3.6.1.2. Silencing of both Nesprin-2 and Nesprin-4 significantly increased the LG1233 cell density in EHT cross-section

Silencing of both Nesprin-2 and Nesprin-4 led to a significant increase in LG1233 cell density within EHT cross-sections (Figure 3-46).

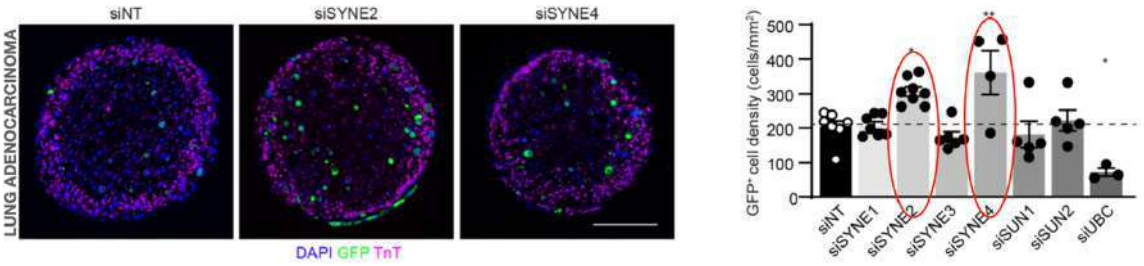

Figure 3-46. Representative cross-sections of EHTs containing LG1233 GFP+ cancer cells treated with the indicated siRNAs (left). Quantification of the density of LG1233 GFP+ cancer cells in EHT cross-sections, upon treatment with the indicated siRNAs (right). Scale bar: 100 µm.

However, none of the LINC complex components influenced cell proliferation when assessed in two-dimensional pure cell cultures (Figure 3-47)

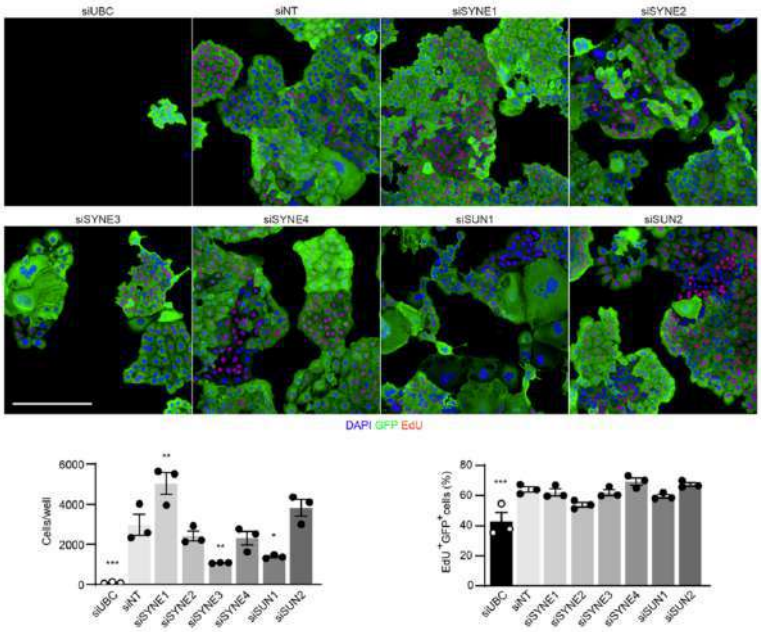

Figure 3-47. Representative images of LG1233 cells upon transfection with the indicated siRNAs. Proliferating nuclei are labelled by EdU. Scale bar: 100 µm (top). Quantification of the number of LG1233 cells after 5 days of culture upon transfection with the indicated siRNAs (bottom left). Quantification of EdU+ LG1233 cells after 5 days of culture upon transfection with the indicated siRNAs (bottom right).

3.6.1.3. For colon cancer cells (CT26) and melanoma cancer cells (B6-F10), silencing of Nesprin-2 resulted in increased proliferative capacity and cell density

Subsequently, Nesprin-2 and Nesprin-4 were silenced in additional cancer cell lines that corresponded to the tumor types analyzed in the spatial transcriptomics of cardiac metastases, specifically CT26 colon cancer cells and B16-F10 melanoma cells. Proliferation was then evaluated in beating EHTs. The silencing of Nesprin-2 led to an

increase in both the area occupied by cancer cells and cell density within EHT cross-sections for CT26 cells (Figure 4-38) and B16-F10 cells (Figure 3-49).

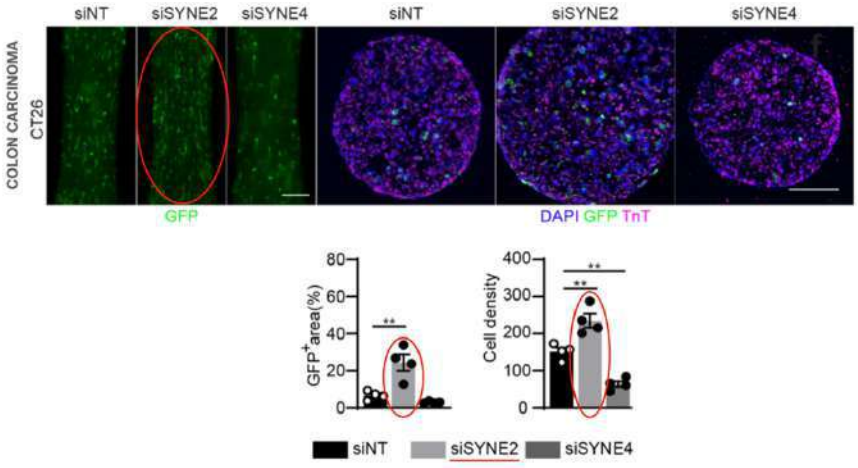

Figure 3-48. Representative low magnification images and cross sections of EHTs containing CT26 GFP+ colon cancer cells treated with the indicated siRNAs (top). Quantification of the area occupied by CT26 GFP+ cancer cells upon treatment with the indicated siRNAs (bottom left). Quantification of the density of CT26 GFP+ cancer cells in EHT cross-sections, upon treatment with the indicated siRNAs (bottom right). Scale bar: 100 µm.

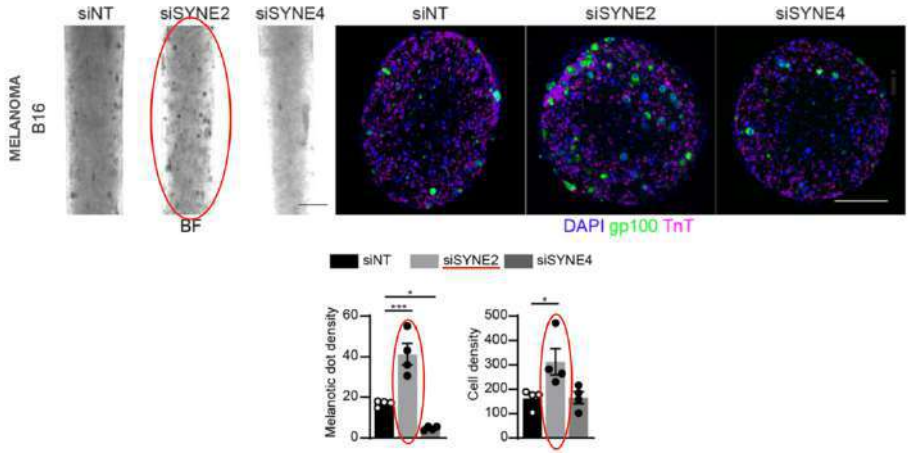

Figure 3-49. Representative low magnification bright-field images and cross sections of EHTs containing B16 melanoma cells, stained for gp100, treated with the indicated siRNAs (top). Quantification of the density of melanotic dots density upon treatment with the indicated siRNAs (bottom left). Quantification of the density of B16 gp100+ melanoma cells in EHT cross-sections, upon treatment with the indicated siRNAs (bottom right). Scale bar: 100 µm.

These findings indicate that Nesprin-2 functions as a critical mechanotransducer in regulating the proliferation of various cancer cell types within beating heart tissues.

3.6.1.4. Nesprin-2 is required to mediate chromatin decompaction in contracting EHT cells

We further examined whether Nesprin-2 was necessary to modulate chromatin structure in response to mechanical load. Figures 3-50 illustrate that Nesprin-2 silencing in LG1233 cells led to a marked increase in chromatin compaction within beating EHTs.

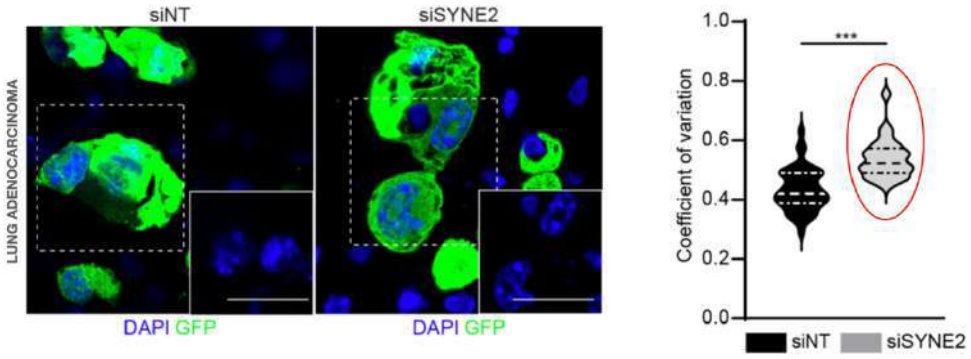

Figure 3-50. Representative images of chromatin compaction by DAPI staining of LG1233 GFP+ cancer cells in and EHTs treated with indicated siRNA (left). Coefficient of variation calculated based on the DAPI fluorescent images (right).

3.6.2. Nesprin-2 under Overloading Conditions

To delve deeper into the role of Nesprin-2 in cardiac mechanotransduction, we conducted experiments under both static and overloaded EHT conditions.

Across all cell types, the effect of Nesprin-2 silencing was more pronounced under conditions of increased mechanical load (Figure 3-51 for LG1233 cells – left and center), with many cells proliferating in the central region of the EHT, an area characterized by elevated hydrostatic compressive pressure (0–120 mm, Figure 3-51 - right).

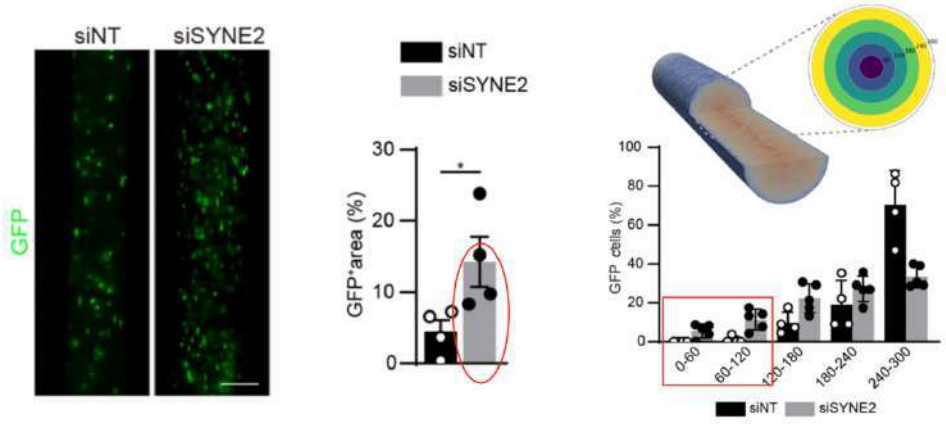

Figure 3-51. Representative low magnification images of overloaded EHTs containing LG1233 GFP+ cancer cells treated with the indicated siRNAs (left). Quantification of the area occupied by LG1233GFP+ cancer cells within overloaded EHTs upon treatment with the indicated siRNAs (center). Distribution of GFP+ cancer cells in the EHT radial layers depicted in different colors (right). Scale bar: 300 µm.

In static EHTs, by contrast, silencing Nesprin-2 did not affect the area occupied by any cell type. (Figure 3-52 for LG1233 cells).

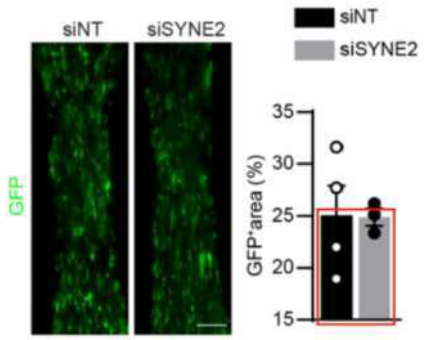

Figure 3-52. Representative low magnification images of static EHTs containing LG1233 GFP+ cancer cells treated with the indicated siRNAs (left). Quantification of the area occupied by LG1233 GFP+ cancer cells within static EHTs upon treatment with the indicated siRNAs (right). Scale bar: 300 µm.

Therefore, by increasing loading forces, the silencing effect of Nesprin-2 is further amplified.

3.6.3. Silencing Nesprin-2 in Vivo

3.6.3.1. Silencing of Nesprin-2 allows cancer cells to extensively expand and proliferate within the myocardium

Nesprin-2 was silenced in LG1233 cells prior to their in vivo implantation into beating hearts. In agreement with the observations from EHT experiments, Nesprin-2 silencing enabled cancer cells to expand significantly and proliferate within the myocardium (Figure 3-53).

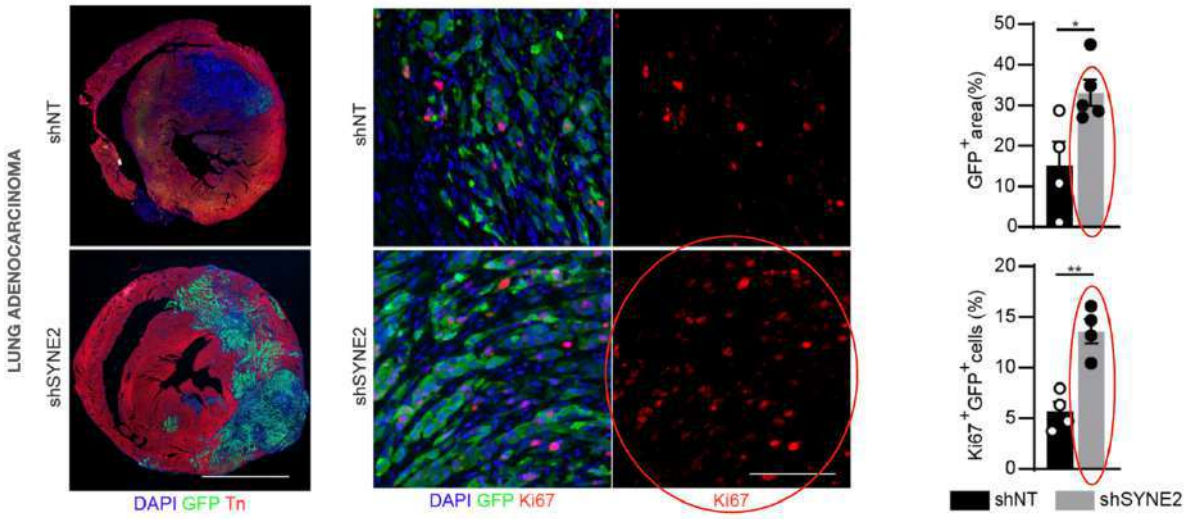

Figure 3-53. Representative immunofluorescence images of hearts injected with LG1233 GFP+ cancer cells transduced with lentiviral vectors expressing the indicated shRNAs (left). High magnification images of GFP+ LG1233 cells transduced with the indicated shRNAs and injected in the heart, stained for the proliferation marker Ki67 (center). Quantification of the area occupied by GFP+ LG1233 cells transduced with the indicated shRNAs and injected in vivo into the cardiac muscle (center). Quantification of proliferating GFP+ Ki67+ LG1233 cancer cells transduced with the indicated shRNAs and injected in vivo into the cardiac muscle (right). Scale bar: 1 mm (left), 50 µm (center).

3.6.3.2. Chromatin compaction is more pronounced in Nesprin-2 silenced cells

Similarly, consistent with earlier findings, Nesprin-2 silencing resulted in increased chromatin compaction in LG1233 cells implanted into beating hearts (Figure 3-54).

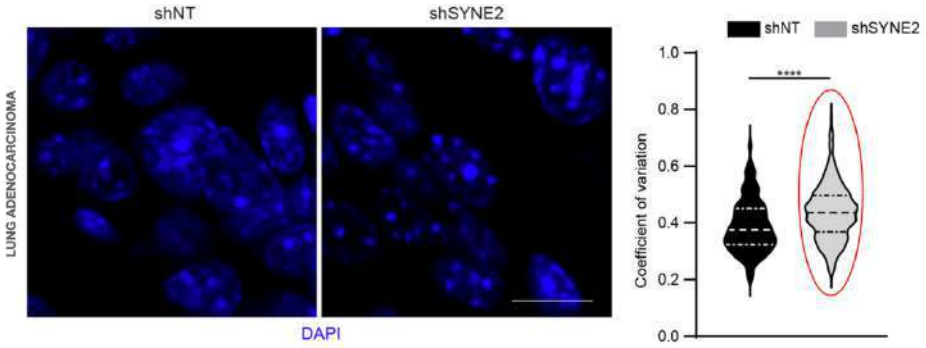

Figure 3-54. Coefficient of variation and representative images of chromatin compaction by DAPI staining of GFP+ LG1233 cancer cells transduced with the indicated shRNAs. Scale bar: 20 µm.

In summary, our findings demonstrate that mechanical load within beating heart tissue leads to a decrease in histone methylation and chromatin compaction in cancer cells, thereby limiting their proliferation. This process of mechanotransduction, which suppresses cancer cell growth in the heart, is critically mediated by Nesprin-2.

4. Discussion

The primary finding and novelty of this manuscript lies in demonstrating that variations in mechanical load have a pronounced impact on cancer cell growth within cardiac tissue. Specifically, mechanical load acts as an inhibitor of cancer cell proliferation both *in vivo* within beating hearts and *ex vivo* in engineered heart tissues (EHTs). In contrast, conditions of mechanical unloading promote cancer cell proliferation, effectively restoring their proliferative capacity. This is a significant insight as it sheds light on the interplay between mechanical forces and cancer biology in the heart, a relatively underexplored area.

4.1. The Importance of an Unloading Model

The use of an in vivo heterotopic transplantation model, as detailed in the previous sections, was crucial in validating the results of this study. The heterotopic model allowed for the accurate simulation of mechanical loading and unloading conditions, providing invaluable insights that would not have been as reliable if only in vitro models had been used. These models offered a more complex, dynamic system where the effects of mechanical load on cancer cell proliferation could be studied within the natural, highly structured environment of the heart.

In vitro models, while valuable for controlled experiments, cannot replicate the complexity of living organisms, particularly in terms of how mechanical forces influence cellular behavior within a tissue. The heterotopic transplantation approach, by transplanting the donor heart into the recipient's cervical region, simulated the mechanical forces that would be present in a living heart, such as compression and stretching during each heartbeat. This method allowed for the observation of cancer cell behavior in response to these forces in a living system, showing results with far greater physiological relevance.

Additionally, the heterotopic model demonstrated a significant enhancement in the applicability and consistency of the findings. While mechanical unloading was shown to promote cancer cell proliferation in isolated in vitro conditions, only within the heterotopic transplantation model did the effect of mechanical load inhibition become clearly evident. This model also proved essential in confirming the mechanistic insights uncovered, particularly with the influence of histone modifications and mechanotransduction pathways on cancer cell proliferation.

4.1.1. Considerations on the Key Stages of HHT

This experience aims to highlight the importance of precision in each phase of the transplantation, as even minor adjustments in the surgical process—such as suture placement or tissue manipulation—directly influence the viability of the graft and its functional outcomes.

During the explantation phase: each micro-movement, suture placement, and adjustment directly influences the viability of the graft and the functional outcome of the procedure.
During the vessel preparation phase: based on my personal experience, the dilation of the common carotid artery is by far the most critical step, essential for the successful eversion of the common carotid artery onto the cuff. Given the arterial nature of the vessel, its extensibility is significantly lower compared to the external jugular vein, whereas its retractability is extremely high. Any minor miscalculation of the length previously obtained will impact this step, potentially preventing the artery from wrapping around the cuff. Further optimization of the eversion technique for the common carotid artery could reduce the risks associated with minor miscalculations during artery length measurements, which can impede the successful wrapping of the artery around the cuff.
During the implantation phase: the goal is not just technical completion but the establishment of a stable and functional connection between the donor heart and the recipient's vascular system. The beating of the transplanted heart is a testament to the surgical accuracy and the success of the procedure.

4.1.2. The Minimally Invasive Approach to Common Carotid Artery Isolation

The surgical refinement introduced by avoiding the sectioning of the sternocleidomastoid (SCM) muscle played a pivotal role in enhancing the success of the procedure. By creating space between the SCM and the sternothyroid muscle through blunt dissection, the procedure not only reduced tissue trauma but also shortened the operative time and minimized bleeding, contributing to a smoother recovery for the animal. This improvement, as described in the Results section, significantly optimized the overall surgical efficiency, reinforcing the importance of minimizing muscle damage during the operation. The reduction in complications provided a more stable foundation for the transplantation, ultimately increasing the stability of the outcomes.

4.1.3. Limitations of the Procedure

However, it is important to recognize the limitations of the heterotopic transplantation methodology. One key challenge is the extremely complex and lengthy learning curve associated with the procedure. Mastery of the necessary microsurgical techniques takes significant practice and experience. Moreover, even when the procedure is well-executed, the mortality rate can still be relatively high, posing a significant obstacle to the model's consistency and reliability.
Enhanced techniques in these areas would improve the overall efficiency of the procedure, minimizing complications and maximizing graft success.

4.2. Impact of Mechanical Load on Proliferation

The inhibitory effect of mechanical load on cardiomyocyte (CM) proliferation has been previously observed in other contexts, such as patients implanted with left ventricular

assist devices (LVADs) and mouse models of myocardial infarction, where unloading conditions were shown to promote CM proliferation [3; 67]. However, this study offers the first evidence that a similar mechanism may also suppress cancer cell proliferation in the heart, potentially serving as a protective barrier against cardiac metastases. This novel discovery bridges the fields of cancer biology and mechanobiology, offering fundamental insights into the unique environment of the heart.

We initially focused on lung adenocarcinoma cells to explore this phenomenon. This choice was motivated by the fact that the lung, like the heart, is continuously exposed to mechanical stimulation. However, the nature of the mechanical forces differs significantly between the two organs. The heart experiences compressive forces due to cardiomyocyte contraction, as demonstrated in the study's models, whereas the lung is subject to stretching forces from diaphragm and intercostal muscle activity. Additionally, lung cancer ranks mid-level in terms of metastatic dissemination to the heart, making it an appropriate model for evaluating the effects of mechanical loading and unloading [8]. To generalize their findings, we extended our research to melanoma and colon cancer cells, which exhibit high and low frequencies of heart metastases, respectively [8; 68-69]. This comparative approach strengthened the conclusion that mechanical load influences cancer cell proliferation across various cancer types.

4.3. Mechanobiology and Cancer Proliferation

Mechanobiology has primarily focused on how cells sense alterations in matrix stiffness and other extracellular physical properties, translating these cues into modified behaviors such as proliferation and invasiveness [70-71]. The current study advances this field by providing robust evidence for the inhibitory effects of compressive forces, like those generated in a beating heart, on cancer cell proliferation. This finding aligns with previous studies, where compressive forces exerted by cancer-associated fibroblasts were shown to suppress proliferation via altered localization of YAP protein. Similarly, volumetric compression induced by osmotic pressure was reported to inhibit melanoma cell proliferation and migration [72-73].

In this study, transcriptomic analysis revealed that histone demethylases were among the most upregulated genes in cardiac metastases, irrespective of the tumor's origin. These enzymes, which dynamically regulate histone methylation, are known to play critical roles in various cancer progression processes, including proliferation, migration, invasiveness, and drug resistance [74-77]. We focused specifically on H3K9 trimethylation (H3K9me3), a hallmark of heterochromatin associated with chromatin compaction and gene expression regulation. We observed that mechanical loading decreased H3K9me3 levels and chromatin compaction across all experimental settings, including native versus heterotransplanted hearts, overloaded versus unloaded EHTs, and human cardiac metastases versus extra-cardiac lesions [78-84].

4.4. Experimental Validation of Mechanistic Insights

To validate the causal relationship between H3K9 trimethylation and cancer cell proliferation under mechanical load, we silenced key histone demethylases, KDM4C and KDM4D, in cancer cells. This intervention resulted in increased proliferation, confirming that these enzymes play a critical role in the observed mechanoresponse. This mechanistic insight is highly relevant, especially in light of recent clinical trials targeting histone-modifying enzymes like KDMs and lysine methyltransferases (KMTs) for cancer therapy [85]. The findings raise the intriguing possibility that such therapies might inadvertently influence the incidence of cardiac cancers, warranting further investigation.

4.5. Role of Nesprin-2 in Mechanotransduction

A critical component of the mechanotransduction pathway identified in this study is the LINC (Linker of Nucleoskeleton and Cytoskeleton) complex, particularly Nesprin-2. This molecule was shown to be essential for halting cancer cell proliferation in response to mechanical load, as its silencing allowed cancer cells to proliferate even in beating EHTs and in vivo hearts. This observation aligns with Nesprin-2's documented role in regulating nuclear architecture, chromatin organization, and the transcription of cancer-associated genes in response to mechanical forces [86]. By identifying Nesprin-2 as a key mediator, this study provides a molecular link between mechanical load and epigenetic regulation, adding a new dimension to our understanding of cancer cell biology.

5. Conclusions

The findings from this study underscore the importance of mechanical forces in regulating cancer cell behavior, particularly in the heart, a site that traditionally experiences low rates of metastasis. By employing a heterotopic transplantation model, the study moved beyond the limitations of in vitro models, providing more robust and applicable results. This model not only validated the hypothesis that mechanical loading inhibits cancer cell proliferation but also revealed key molecular mechanisms, such as histone demethylation and chromatin compaction, that could be targeted therapeutically.

The results suggest a protective role for the mechanical environment of the heart against metastasis, potentially explaining the rarity of cardiac tumors despite the heart's high blood flow. Importantly, the study opens new avenues for therapeutic interventions that could harness mechanical forces to suppress tumor growth in other tissues. By mimicking the mechanical forces experienced in the heart, it may be possible to develop novel mechanical therapies for cancer, particularly in tissues prone to metastatic invasion.

In future research, further refinements to the surgical techniques employed in the heterotopic transplantation model could optimize short-term survival rates for the recipient animals. These improvements would contribute to the reproducibility and consistency of results, enhancing the overall success of the procedure.

The insights gained from this research contribute to our understanding of cancer cell behavior in response to mechanical forces and open avenues for targeted therapies that utilize mechanical stimuli. Future studies should explore the broader applications of these findings in other tissues and cancer types, with the potential for clinical applications to improve cancer treatments and reduce metastasis.

References

1. Giacca, M. et al., "Harnessing the micro-RNA pathway for cardiac regeneration," 2015.
2. Puente, B. N. et al., "Oxygen increases oxidative stress and halts cardiomyocyte cell cycle," 2014.
3. Canseco, D. C. et al., "Human mechanical unloading induces cardiomyocyte proliferation," 2015.
4. Kocijan, T. et al., "Genetic lineage tracing reveals poor angiogenic potential of cardiac endothelial cells," 2020.
5. Meschia, G. et al., "Fetal circulation and oxygen saturation levels," 2011.
6. Lopaschuk, G. D. & Jaswal, J. S., "Metabolic adaptations in postnatal cardiomyocytes," 2010.
7. Nolfi-Donegan, D. et al., "Mitochondrial ROS and DDR activation," 2020.
8. Bussani, R. et al., "Epidemiology of primary and secondary cardiac tumors," 2007.
9. Amano, J. et al., "Metastatic mechanisms in the heart," 2013.
10. Al-Mamgani, A. et al., "Cardiac metastases distribution and impact," 2008.
11. Bergmann, O. et al., "Annual cardiomyocyte renewal rate in adults," 2009.
12. Rubart, M. & Field, L. J., "Cellular composition of the heart," 2006.
13. Roberts, W. C., "Primary cardiac tumors arising in epicardium and atrial walls," 1997.
14. Burke, A. P. et al., "Classification of primary cardiac tumors," 1990.
15. Ekmektzoglou, K. A. et al., "Cardiac tumors: benign and malignant," 2008.
16. Lestuzzi, C., "Clinical features of cardiac myxomas," 2016.
17. Burke, A. & Virmani, R., "Rhabdomyomas and their clinical significance," 2008.
18. Nwachukwu, N. et al., "Fibromas in pediatric cardiology," 2011.
19. Shu, J. et al., "Clinical features of cardiac lipomas," 2021.
20. Maleszewski, J. et al., "Hamartomas in the cardiac context," 2018.
21. Joshi, P. et al., "MDM2 expression in undifferentiated sarcomas," 2020.
22. Taguchi, T., "Prognosis and progression of angiosarcomas," 2018.
23. Tischoff, I. & Tannapfel, A., "Clinical aspects of pericardial mesotheliomas," 2017.
24. Zhao, Y. et al., "B-cell cardiac lymphomas," 2021.
25. Lee, J. et al., "Mechanobiology: cellular response to mechanical stimuli," 2011.
26. Szczesny, S. E. & Mauck, R. L., "Advances in mechanotransduction mechanisms," 2017.
27. Liu, Y. et al., "Mechanotransduction and cellular adaptation," 2023.
28. Zacchigna, S. & Giacca, M., "Mechanical load and subepicardial growth," 2014.
29. Kikuchi, K. et al., "Regenerative capacity in vertebrate cardiac chambers," 2010.
30. Sun, J. et al., "Nuclear mechanics in disease progression," 2020.

31. Schreiner, S. M. et al., "Nuclear mechanotransduction pathways," 2015.
32. Pajerowski, J. et al., "Nuclear deformation in cancer cells," 2007.
33. Roberts et al. 2021.
34. Enyedi et al., "Nuclear membrane stretch and its role in mechanotransduction", 2016.
35. Neelam et al., "Direct force measurements on the cell nucleus using optical tweezers", 2015.
36. Friedl et al., "Classifying collective cancer cell invasion", 2011.
37. Li et al., "Nuclear lamin A/C as a mechanotransducer mediating cellular mechanoadaptation and mechanotransduction", 2015.
38. Zullo et al., "DNA sequence-dependent compartmentalization and silencing of chromatin at the nuclear lamina", 2012.
39. Dahl et al., "Power-law rheology of isolated nuclei with deformation mapping of nuclear substructures", 2005.
40. Feinberg et al., "Assessing the stiffness of biological materials and tissues using atomic force microscopy", 2016.
41. Tajik et al., "Transcription upregulation via force-induced direct stretching of chromatin", 2016.
42. Elosegui-Artola, A. et al., "Mechanosensitive gene expression via LINC," 2017.
43. Davidson et al. "Nuclear deformability constitutes a rate-limiting step during cell migration in 3-D environments", 2014.
44. Alam, S. et al., "LINC complex in tumor invasion and metastasis," 2016.
45. Gundersen, G. G. & Worman, H. J., "Role of LINC in mechanotransduction," 2013.
46. Janota et al., "The LINC complex: ushering the nucleus into position", 2017.
47. Nie et al., 2016.
48. Harada, T. et al., "Nuclear deformability and migration," 2014.
49. Razafsky, D. et al., "LINC-mediated genomic stability," 2013.
50. Matsumoto, A. et al., "Downregulation of nesprins in breast cancer," 2015.
51. Sjöblom, T. et al., "Mutations in LINC components in gastrointestinal cancers," 2023.
52. Guilluy, C. et al., "Force transmission in cancer cell migration," 2014.
53. Stewart-Hutchinson et al., "Structural requirements for the assembly of LINC complexes and their function in cellular mechanical stiffness", 2008
54. g et al., "A new mouse model of heterotopic heart transplantation to study graft arteriosclerosis", 1991.
55. Wang et al., "A novel murine model of heterotopic heart transplantation for the study of transplant arteriosclerosis", 2002.
56. Yasura et al., "A new technique for heterotopic cardiac transplantation in mice", 1991;
57. A. K. Nowocin et al., "An extraperitoneal technique for murine heterotopic cardiac transplantation", 2015.

58. Oberhuber et al., “Murine cervical heart transplantation model using a modified cuff technique”, 2014.
59. Eschenhagen, T. et al., "Development of engineered heart tissues," 2002.
60. Hansen, A. et al., "Miniaturization and scalability of EHTs," 2010.
61. Janmey, P. A. et al., "Fibrin as a biopolymer in tissue engineering," 2009.
62. Ratschiller, T. *et al., “*Heterotopic Cervical Heart Transplantation in Mice”, 2015.
63. Dupont, C. *et al. “*Evidence for low nanocompaction of heterochromatin in living embryonicstem cells”, 2023.
64. Ramirez-Cuellar, J. *et al. “*LATS1 controls CTCF chromatin occupancy and hormonal response of 3D-grown breast cancer cells”, 2024.
65. Salinas-Pena, M. e al., “Imaging analysis of six human histone H1 variants reveals universal enrichment of H1.2, H1.3, and H1.5 at the nuclear periphery and nucleolar H1X presence”, 2024.
66. Mejat, et Al., “LINC complexes in health and disease”, 2010.
67. Suzuki, R. *et al., “*The reduction of hemodynamic loading assists self-regeneration of the injured heart by increasing cell proliferation, inhibiting cell apoptosis, and inducing stem-cell recruitment”, 2007.
68. Bussani, R. *et al., “*Cardiac Tumors: Diagnosis, Prognosis, and Treatment”, 2020.
69. Nova-Camacho, L. M. *et al., “*Cardiac Metastasis From Solid Cancers: A 35-Year Single-Center Autopsy Study”, 2023.
70. Bertolio, R. *et al*., “Dynamic links between mechanical forces and metabolism shape the tumor milieu”, 2023.
71. Mohammadi, H. *et al*., “Mechanisms and impact of altered tumour mechanics”, 2018.
72. Barbazan, J. *et al. “*Cancer-associated fibroblasts actively compress cancer cells and modulate mechanotransduction”, 2023.
73. Zhang, X. *et al. “*Compression drives diverse transcriptomic and phenotypic adaptations in melanoma”., 2023.
74. An, X. *et al*., “ Histone modification: Biomarkers and potential therapies in colorectal cancer”, 2023.
75. Audia, J. E. *et al*. “Histone Modifications and Cancer”, 2016.
76. Chen, Y. *et al*. “ The role of histone methylation in the development of digestive cancers: a potential direction for cancer management”, 2020.
77. Zhuang, J. *et al*., “Perspectives on the Role of Histone modification in Breast Canter Progression and the Advanced Technological Tools to Study Epigenetic Determinants of Metastasis”, 2020.
78. Sterling, J. *et al*. “Histone lysine demethylases and their functions in cancer”, 2021.
79. Black, J. C. *et al*., “Histone lysine methylation dynamics: establishment, regulation, and biological impact”, (2012).

80. Yokoyama, Y. *et al., "*Cancer-associated upregulation of histone H3 lysine 9 trimethylation promotes cell motility in vitro and drives tumor formation in vivo", 2013.
81. Gaggioli, V. *et al., "* Dynamic de novo heterochromatin assembly and disassembly at replication forks ensures fork stability", 2023.
82. Lam-Ubol, A. *et al*., Distinct histone H3 modification profiles correlate with aggressive characteristics of salivary gland neoplasms", 2022.
83. Keung, E. Z. *et al., "*Increased H3K9me3 drives dedifferentiated phenotype via KLF6 repression in liposarcoma", 2015.
84. Chen, M. W. *et al., "*H3K9 histone methyltransferase G9a promotes lung cancer invasion and metastasis by silencing the cell adhesion molecule Ep-CAM", 2010.
85. Yu, X. *et al., "*Cancer epigenetics: from laboratory studies and clinical trials to precision medicine", 2024.
86. Li Mow Chee, F. *et al., "* Mena regulates nesprin-2 to control actin-nuclear lamina associations, trans-nuclear membrane signalling and gene expression", 2023.

Acknowledgements

Prof. Serena Zacchigna
Prof. Gabriele Stocco
Prof. Marianna Lucafò
Giulio Ciucci, PhD
Roman Vuerich, PhD
Simone Vodret, PhD
Andrea Colliva, PhD
Ann-Vu Nguyen, PhD

Table of contents

Abbreviations

CAF	Cancer-associated fibroblasts
CM	Cardiomyocytes
DDR	DNA Damage Response
EdU	5-ethynyl-2'-deoxyuridine
ECM	Extracellular Matrix
EHT	Engineered Heart Tissue
ERK	Extracellular Signal-Regulated Kinases
FAK	Focal Adhesion Kinase
GFP	Green Fluorescent Protein
HA	Hyaluronic Acid
HHT	Heterotopic Heart Transplant
IF	Intermediate Filaments
INM	Inner Nuclear Membrane
KDM	Lysine-Specific Demethylases
LAD	Lamina-Associated Domains
LINC	Linkers of the Nucleoskeleton to the Cytoskeleton
LOX	Lysyl Oxidase
LV	Left Ventricle
LVAD	Left Ventricular Assist Device
MAPK	Mitogen-Activated Protein Kinase
MT	Microtubules
NE	Nuclear Envelope
NPC	Nuclear Pore Complex
ONM	Outer Nuclear Membrane
PBS	Phosphate-Buffered Saline
ROCK	Rho-Associated Protein Kinase
ROS	Reactive Oxygen Species
siRNA	Small Interfering RNA
SUN	Sad1 and UNC-84 Domain-Containing Protein
SYNE	Spectrin Repeat-Containing Nuclear Envelope Protein
TAZ	Transcriptional Co-Activator with PDZ-Binding Motif
TME	Tumor Microenvironment
UPS	Undifferentiated Pleomorphic Sarcoma
YAP	Yes-Associated Protein

1. Introduction

1.1. Cardiomyocytes and the Heart's Regenerative Capacity

1.1.1. Starting points

Lower vertebrates, such as fish and amphibians, are able to regenerate the myocardium after damage, a capacity that contrasts sharply with the limited regenerative ability observed in mammals. The mammalian heart has long been viewed as a post-mitotic organ, meaning it lacks the ability to regenerate significantly in adult life. This belief is supported by the common understanding that myocardial damage heals through scarring rather than new tissue growth. However, recent evidence challenges this notion by revealing that the heart retains a modest regenerative capacity. For example, studies using ^{14}C-dating and imaging mass spectrometry have shown that cardiomyocytes renew at a rate of about 1% per year, translating to the formation of 30-40 million new cells annually. This renewal rate, although low, is not insignificant and appears to increase after myocardial infarction [1;11].

The limited regenerative potential of adult cardiomyocytes is closely tied to their behavior during development. Cardiomyocytes actively proliferate during embryogenesis, contributing to heart growth, but they exit the cell cycle shortly after birth. This developmental shift is thought to result from postnatal changes such as increased oxygen levels, heightened oxidative stress, and mechanical strain, which collectively inhibit cell division [2-3].

The origin of new cardiomyocytes in the adult heart remains debated. Some researchers suggest that existing cardiomyocytes may divide, while others highlight the role of endogenous cardiac progenitor cells. These progenitor cells, identified by markers like Sca-1 or c-Kit, have been shown in animal studies to generate not only cardiomyocytes but also vascular cells. However, the clinical relevance of these findings, especially in humans, is still uncertain.

This modest yet demonstrable regenerative capacity of the heart has spurred interest in developing therapies to enhance it. Inspired by the remarkable regenerative abilities of lower vertebrates, scientists aim to uncover mechanisms that could overcome the barriers imposed by postnatal changes, potentially unlocking the heart's latent regenerative potential. Such advancements offer hope for innovative treatments for heart disease and myocardial repair [1].

1.1.2. Loss of angiogenic potential after birth in cardiac endothelial cells

Using Apelin-CreER mice to genetically trace sprouting endothelial cells, some study observed a notable divergence in angiogenic behavior between skeletal and cardiac muscle [4]. Both tissue types responded similarly to pro-angiogenic stimuli, such as VEGF, by activating Apelin expression, a key marker of endothelial activation. However,

only skeletal muscle endothelial cells progressed beyond this activation phase. In skeletal muscle, Apelin-positive cells were able to sprout, form elongated vascular structures, activate Notch signaling, and incorporate into newly forming arteries. This robust angiogenic response underscores the tissue's regenerative and vascular adaptability.

In contrast, cardiac endothelial cells exhibited a profound limitation in their angiogenic potential. Despite expressing Apelin in response to the same stimuli, these cells failed to initiate sprouting or form functional vascular networks. Apelin-positive endothelial cells in the heart transiently persisted but did not contribute to new vessel formation, effectively stalling angiogenesis at an early stage. This inability to progress further reflects the heart's intrinsic challenges in both regenerative vascularization and tumor-induced angiogenesis. Tumor cells, which typically induce robust angiogenesis to sustain their growth and metastasis in other tissues, encounter resistance in the cardiac microenvironment. Consequently, tumors grow less in the heart than in the skeletal muscle: cardiac endothelial cells do not adequately respond to tumor-driven pro-angiogenic signals, a phenomenon potentially linked to their specialized biology and the postnatal loss of angiogenic and regenerative potential.

These findings suggest that skeletal muscle endothelial cells possess an intrinsic ability to fully execute the angiogenic program, a capability that is markedly deficient in cardiac endothelial cells. This disparity not only illustrates the heart's limited capacity for regeneration but also its unique resistance to tumor-associated vascular remodeling, driven by a developmental decline in angiogenic capacity after birth [4].

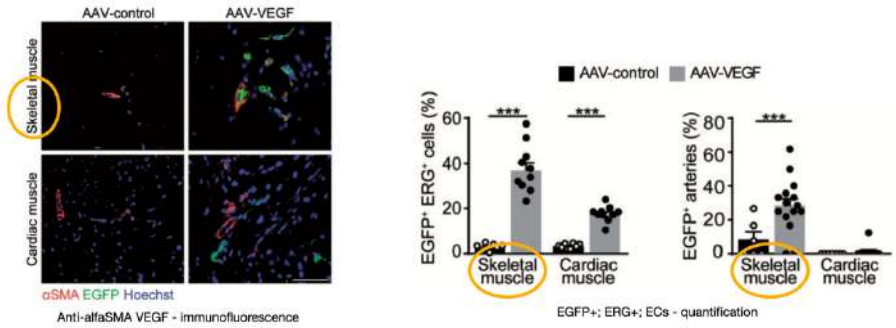

Figure 1-1. Representative immunofluorescence staining of skeletal and cardiac muscle of Apln-CreER; R26mT/mG mice injected with either AAV-control (left) or AAV-VEGF (right), labelled with anti-a-SMA antibodies [left image].

Quantification of the number of EGFPþ ERGþ endothelial cells (% of ERGþ cells) and quantification of the number of ar- teries containing EGFPþ endothelial cells (% of total arteries)- [right image].

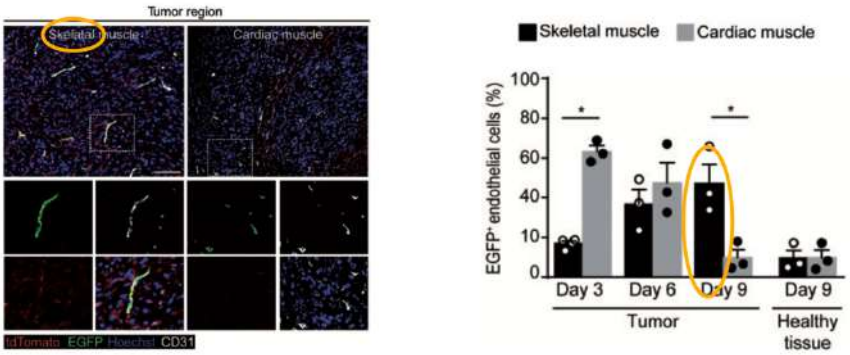

Figure 1-2. Representative immunofluorescence staining of skeletal and cardiac muscle of Apln-CreER; R26mT/mG mice injected with LG cells, labelled with anti-CD31 antibodies 9 days after cancer cell in- jection. Panels on the left show regions highly infiltrated by cancer cells, whereas panels on the right show the surrounding, healthy tissue. Boxed regions are magnified in the lower panels to show split channels [left image]. Quantification of the number of EGFPþ endothelial cells (% of CD31þ cells) at the indi- cated time points in either the tumour region or the surrounding, healthy tissue [right image].

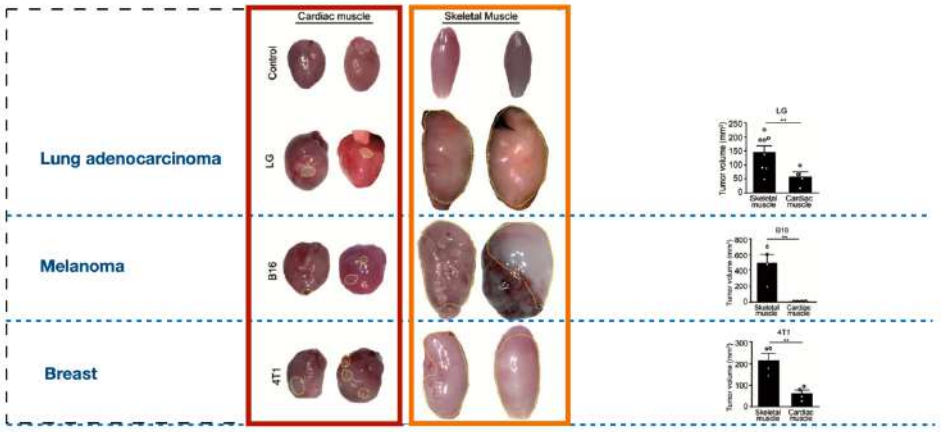

Figure 1-3. Representative whole organ pictures of hearts and skeletal muscle not treated or injected with LG lung adenocarcinoma (left). Relative quantification (right).

1.2. The Role of Hyperoxic Stress and Reactive Oxygen Species (ROS) in Cardiomyocyte Proliferation Arrest

Recent investigations emphasize the pivotal role of reactive oxygen species (ROS) and DNA damage response (DDR) in cardiomyocyte proliferation arrest during the early postnatal period. This shift is marked by a surge in ROS production and DDR markers within the first week after birth, correlating with a sharp decline in the proliferative ability

of cardiomyocytes [2]. The findings suggest a causal link between oxidative stress and cardiomyocyte cell-cycle exit.

In utero, fetal circulation is characterized by specialized shunts—ductus venosus, foramen ovale, and ductus arteriosus—that prevent a clear segregation of venous and arterial blood. This system results in moderate oxygen saturation levels, with umbilical venous blood reaching approximately 80-90% oxygenation and left ventricular output around 65% [5]. Following birth, the closure of these shunts establishes a distinct arterial-venous separation, exposing cardiomyocytes to an oxygen-rich environment. This postnatal hyperoxia triggers a metabolic transition from anaerobic glycolysis to oxidative phosphorylation in mitochondria [6]. While this adaptation enhances energy efficiency, it concurrently increases ROS production, leading to oxidative DNA damage and DDR activation [7].

The study by Canseco et al. (2015) [3] further elaborates on these processes, highlighting mitochondrial biogenesis as a central component of ROS generation and DDR activation postnatally. Mitochondrial proliferation amplifies oxidative stress, which inhibits cardiomyocyte proliferation by activating the DDR pathways. However, evidence from left ventricular assist device (LVAD) studies reveals that mechanical unloading can reverse this cascade. In patients undergoing LVAD implantation, reductions in mitochondrial content and DDR markers, such as phosphorylated ATM protein, were observed. This was associated with a re-entry of cardiomyocytes into the cell cycle, suggesting that metabolic and mechanical stresses jointly regulate cardiomyocyte quiescence and proliferation. So, prolonged mechanical unloading induces adult human cardiomyocyte proliferation, possibly through prevention of mitochondria-mediated activation of DDR.

This interplay underscores the complexity of cardiomyocyte development and the intrinsic limitations of the postnatal heart's regenerative capacity. ROS-driven oxidative damage, exacerbated by hyperoxic stress and mechanical load, establishes a cellular environment resistant to regeneration. However, therapeutic interventions like LVADs provide insights into potential pathways for enhancing cardiac regeneration through targeted modulation of these stressors.

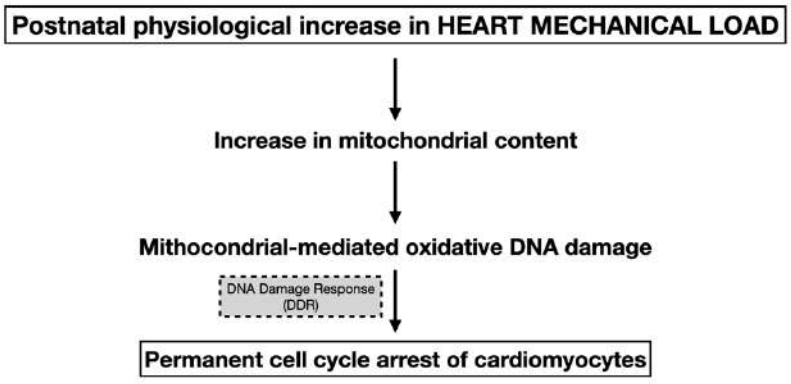

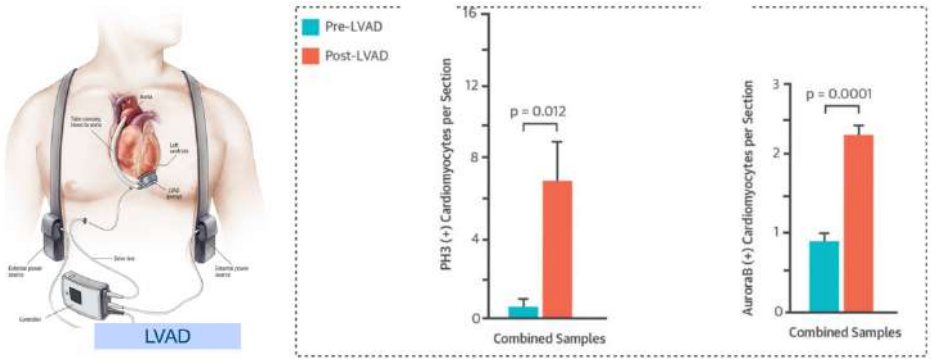

Figure 1-4. Cardiomyocyte Proliferation in LVAD Patients: Prolonged Mechanical Unloading Results in a Switch From Hypertrophic to Hyperplastic Cardiomyocyte Growth: Post-LVAD, cardiomyocytemitosis, shown by increased pH3-positive cardiomyocytes (left), and cardiomyocytecytokinesis, shown by increased Aurora B localization to cytokinetic furrows (right), were both significantly increased in the combined samples.

1.3. Heart cancers

1.3.1. Epidemiology

Primary and secondary cardiac tumors exhibit distinct characteristics in terms of incidence and pathogenesis. Primary cardiac tumors are exceptionally rare, with post-mortem studies reporting frequencies ranging from 0.001% to 0.28% [8]. These tumors are predominantly benign, such as myxomas, lipomas, and fibroelastomas, with malignant forms like sarcomas being far less common. Secondary cardiac tumors, however, are more prevalent, as the heart can serve as a metastatic site for any malignant neoplasm capable of distant spread [9]. The incidence of cardiac metastases, while more frequent than primary tumors, remains lower than in other organ systems. This is paradoxical given the heart's extensive vascularization, which theoretically should facilitate metastatic seeding.

When cardiac metastases occur, they primarily affect the pericardium, large vessels, and coronary arteries, with limited infiltration of the myocardium [10]. Tumors such as melanoma, lung cancer, breast cancer, and mesothelioma are particularly likely to metastasize to the heart. Despite the heart's susceptibility to metastatic involvement, its intrinsic protection against primary tumorigenesis and limited tumor growth capacity reflect unique biological constraints.

The rarity of primary cardiac tumors may be explained by the negligible proliferative capacity of mature CMs. Studies suggest that only 1% of CMs divide annually in adulthood [1; 11]. Although CMs are not the sole cell type in the heart—fibroblasts, smooth muscle cells, vascular endothelial cells, peripheral neurocytes, and myocardial interstitial cells also contribute to its cellular composition—tumors originating from these other cell types are equally uncommon [12]. This raises intriguing questions about

the heart's unique microenvironment and its resistance to tumorigenesis, highlighting the need for further exploration into the mechanisms underlying its tumor biology.

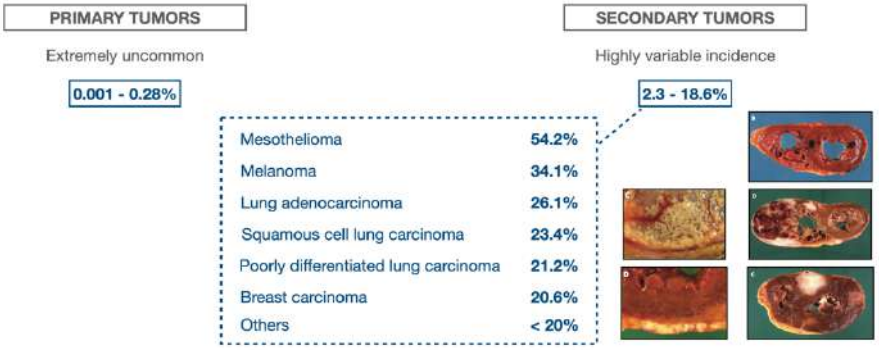

Figure 1-5. A schematic representation of heart's tumor epidemiology.

1.3.2. Primary Cardiac Neoplasms

Primary cardiac tumors predominantly arise in the epicardium and atrial walls, areas subject to lower mechanical stress [13]. These neoplasms can be benign or malignant.

1.3.2.1. Benign Primary Cardiac Neoplasms

Approximately 75% of primary cardiac tumors are benign, including myxomas, lipomas, fibroelastomas, rhabdomyomas, fibromas, and angiomas [14-15].

Myxomas are the most frequently encountered benign cardiac tumors, originating from the endocardium and projecting into the cardiac chambers. They are most commonly found in the left atrium and typically manifest between the fourth and sixth decades of life. These tumors exhibit a slight predominance in females and are predominantly sporadic in nature, with no established genetic or underlying conditions linked to their occurrence [16]. Myxomas are known for their potential to cause symptoms related to obstruction or embolization, necessitating prompt surgical intervention in most cases.

Rhabdomyomas, on the other hand, are congenital hamartomas that represent the most prevalent cardiac tumors in pediatric populations. These lesions generally present in neonates within the first two weeks of life and are frequently multiple, often localized in the ventricles or the interventricular septum. A significant proportion of rhabdomyomas are associated with tuberous sclerosis, indicating a genetic basis for their development. Unlike other tumors, rhabdomyomas often regress spontaneously over time, with surgical intervention reserved for severe or symptomatic cases where critical cardiac function is compromised [17].

Fibromas are another type of benign cardiac tumor, originating from connective tissue and predominantly seen during childhood, with a notable male predominance. These tumors often arise in the interventricular septum or the left ventricle. Clinically, they can present with a variety of symptoms, including arrhythmias, syncope, chest pain, or signs

of heart failure, depending on their size and location. In symptomatic cases, surgical resection may be required to alleviate these complications and restore normal cardiac function [18].

Lipomas, by contrast, tend to occur in elderly, overweight females and are typically located in subendocardial, subepicardial, or endocardial regions. These tumors are often asymptomatic and discovered incidentally. As a result, treatment is generally unnecessary unless the lipoma becomes symptomatic, in which case surgical resection may be considered to address the patient's symptoms and prevent further complications [19].

Hamartomas of mature cardiac myocytes are a distinct form of cardiac tumor, characterized by solitary lesions composed of disorganized and hypertrophic cardiomyocytes. These tumors are more commonly observed in males, approximately twice as often as in females, and typically present during the second decade of life. Although relatively rare, their identification is critical to differentiating them from other cardiac pathologies and managing potential complications associated with their presence [20]. Together, these tumors highlight the diverse nature of benign cardiac neoplasms, each with unique clinical presentations, prognoses, and management strategies.

1.3.2.2. Malign Primary Cardiac Neoplasms

Malignant primary cardiac tumors are exceptionally rare, accounting for only 25% of all primary cardiac neoplasms, with sarcomas representing the vast majority. Other malignancies in this category include mesotheliomas, lymphomas, and tumors associated with Li-Fraumeni syndrome, highlighting the diverse but infrequent nature of these conditions [15].

Among malignant primary cardiac tumors, high-grade undifferentiated pleomorphic sarcoma (UPS) is the most common. This tumor typically arises in the posterior wall of the left atrium and has an average onset age of 47, with a slight predominance in females. UPS is composed of undifferentiated, mitotically active, and pleomorphic cells that often lack distinctive histological features, making diagnosis challenging. Immunohistochemistry is of limited utility in identifying UPS, with overexpression of the MDM2 gene and protein being the most consistent diagnostic marker [21]. Despite its rarity, the aggressive nature of UPS necessitates early recognition and intervention, although the prognosis remains guarded.

Angiosarcomas are the second most frequent malignant primary cardiac tumors, predominantly occurring in the right atrium or atrioventricular sulcus. These tumors are generally sporadic and are characterized by their highly vascular nature, which often leads to symptoms such as chest pain, weight loss, dyspnea, and cardiac tamponade. Prognosis is poor, with a five-year mortality rate of approximately 87%, reflecting the aggressive progression and limited treatment options available for this malignancy [22].

Pericardial mesothelioma, while exceedingly rare, represents 50% of all primary pericardial tumors. This malignancy arises from either the visceral or parietal pericardium and is notable for its lack of strong correlation with asbestos exposure, a factor commonly linked to pleural mesotheliomas. Clinically, pericardial mesotheliomas present with pericardial effusion, tamponade, and chest discomfort, and the prognosis is dismal, with a median survival time typically under six months [23]. The rarity of this condition, coupled with its nonspecific symptoms, often delays diagnosis, further complicating management.

Cardiac lymphomas, while constituting only 1–2% of all cardiac tumors, are more frequently observed in immunocompromised patients. The majority of these malignancies are B-cell lymphomas that primarily involve the right atrium and pericardium. Patients with cardiac lymphomas often present with systemic symptoms such as fever, fatigue, and weight loss, in addition to localized manifestations including chest pain and, in rare cases, pulmonary embolism [24]. The diagnosis and treatment of cardiac lymphomas require a multidisciplinary approach due to their systemic nature and involvement of critical cardiac structures.

Collectively, malignant primary cardiac tumors are rare but aggressive entities that pose significant diagnostic and therapeutic challenges. The limited regenerative capacity of cardiac tissues and the unique biology of cardiac cells may contribute to their low incidence but also hinder effective therapeutic responses, emphasizing the need for continued research into these complex conditions.

1.3.2.3. Cardiac metastases

Cardiac metastases are significantly more common than primary cardiac tumors, with reported incidences ranging from 0.7% to 3.5% in the general population and up to 14.2% in individuals with advanced malignancies. Despite this, cardiac metastases are less frequently observed compared to metastases in other organs, such as the liver or lungs. The relative rarity of cardiac involvement is intriguing, given the heart's extensive vascularization, which would theoretically make it a prime target for metastatic spread.

When cardiac metastases do occur, they typically affect the pericardium, large vessels, and coronary arteries, with myocardial infiltration being relatively uncommon. This distribution reflects the pathways through which malignant cells can reach the heart: hematogenous dissemination, lymphatic spread, direct extension from adjacent structures (such as the lungs), or venous invasion via the vena cava. The specific tumor types most likely to metastasize to the heart include carcinomas of the breast and lung, hematological malignancies (such as lymphomas and leukemias), and melanomas. In contrast, slower-growing neoplasms, such as prostate cancer, rarely metastasize to the heart [8].

The cardiac microenvironment poses intrinsic barriers to metastasis. Tumor cells that reach the heart may encounter challenges such as the high mechanical stress of cardiac contractions and the unique properties of cardiac endothelial cells, which exhibit limited

angiogenic potential. This contrasts with endothelial cells in other tissues, which are more responsive to pro-angiogenic stimuli. The inability to establish a robust vascular network in cardiac tissues likely contributes to the restricted growth of metastases in this organ.

Clinically, cardiac metastases often present with nonspecific symptoms or remain asymptomatic, making diagnosis challenging. When symptomatic, patients may experience pericardial effusion, tamponade, arrhythmias, or heart failure, depending on the location and extent of the metastatic involvement. Pericardial involvement is the most common and is frequently associated with effusions that can progress to tamponade, requiring urgent intervention [8].

1.4. Mechanobiology

Mechanobiology is the study of how cells sense and respond to mechanical stimuli [25]. Recent advancements in mechanobiology have enhanced our understanding of mechanotransduction mechanisms [26].

Mechanotransduction is the process by which mechanical signals from the extracellular matrix (ECM) or cytoskeleton are converted into intracellular biochemical signals, triggering cellular responses. This process involves the ECM, cytoskeleton, LINC (linker of nucleoskeleton and cytoskeleton) complexes, and the nucleus. Mechanotransduction enables cells to rapidly adapt to changes in their physical environment, playing critical roles in cell differentiation, tissue function, and disease development [27].

1.4.1. The Role of Mechanical Forces

Various studies suggest that elevated mechanical load in the heart inhibits cardiomyocyte proliferation. First, during postnatal development, subendocardial myocardial cells experience higher mechanical loads and proliferate less compared to subepicardial cells [28]. Second, lower vertebrates capable of heart regeneration in adulthood have low-pressure cardiac chambers [29]. Third, an inverse relationship between mechanical load (increased cavity pressure and volume, resulting in cardiomyocyte stretching) and proliferation has been observed in patients with end-stage heart failure treated with LVADs, which bypass the left ventricle and pump blood directly into the aorta. Post-mortem analyses of hearts from LVAD-implanted patients revealed increased cardiomyocyte replication [3].

Reducing mechanical stimuli, such as cavity pressure and volume, allowed cardiomyocytes to re-enter the cell cycle. These findings suggest that mechanical forces may inhibit cardiomyocyte duplication.

1.4.2. Nuclear Mechanotransduction: Structure, Function, and Key Components

The nucleus, the largest and most rigid organelle in the cell, plays a central role in mechanotransduction, where mechanical stimuli are converted into biochemical signals that influence various cellular processes. The structural organization and mechanical properties of the nucleus are crucial for functions such as gene expression, cell division, differentiation, apoptosis, and disease progression, including cancer metastasis [30-34]. The mechanical properties of the nucleus not only reflect its structural integrity but also mediate interactions with the extracellular environment, making nuclear mechanics a key indicator of cellular responses to mechanical stimuli [35].

1.4.2.1. Structural Organization of the Nucleus and Mechanotransduction Pathways

The nucleus is composed of the nuclear envelope (NE), nuclear lamina, chromatin, and nucleoplasm, with the nuclear lamina and chromatin being the primary contributors to nuclear mechanics [27]. As a semi-permeable barrier, the nuclear envelope encapsulates the genome and serves as a dynamic interface for mechanical and biochemical signal transmission between the cytoskeleton and the chromatin. The nuclear lamina, composed of type A and type B lamins, provides structural support, while chromatin, the complex of DNA and associated proteins, mediates genomic activities and contributes to nuclear stiffness.

1.4.2.2. Mechanisms of Nuclear Mechanotransduction

Mechanotransduction within the nucleus involves several mechanisms that allow the cell to sense and respond to external mechanical stimuli. These include the deformation of the nuclear envelope, conformational changes in associated proteins, and alterations in chromatin organization. These pathways operate synergistically to translate mechanical forces into biochemical signals, ultimately influencing cellular behavior [27].

<u>Nuclear Lamina and Its Role in Mechanotransduction</u>

The nuclear lamina, an elastic mesh located beneath the inner nuclear membrane, is primarily composed of type A and type B lamins, which are intermediate filaments critical for maintaining nuclear shape and mechanical stability. The lamina resists deformation during mechanical stress and supports cellular processes like migration and spreading [36-37]. Lamins also regulate chromatin organization by tethering chromatin domains, known as lamina-associated domains (LADs), to the nuclear periphery. The stability of these interactions is vital for maintaining nuclear integrity and influencing gene silencing or activation [38].

<u>Chromatin Dynamics in Response to Mechanical Forces</u>

Chromatin, which mediates DNA-centric activities such as transcription, replication, and repair, contributes significantly to nuclear stiffness. Unlike the elastic nuclear lamina, chromatin exhibits viscoelastic behavior under mechanical forces, with its compaction

state determining its stiffness and capacity to respond to stress [39]. Mechanical forces applied to the nucleus can alter chromatin compaction, reorganizing chromatin territories and influencing gene expression. These changes often involve LADs and the repositioning of chromatin to enable or restrict transcriptional activity [41]. The viscoelastic properties of chromatin also facilitate the absorption of mechanical stress, protecting nuclear integrity during deformation.

Nuclear Envelope and Pore Complexes in Signal Transmission

The nuclear envelope (NE) is a key structural and functional component in mechanotransduction. It houses nuclear pore complexes (NPCs), which regulate the bidirectional trafficking of molecules such as transcription factors, RNA, and ions. Under mechanical stress, the NE and NPCs undergo deformation, influencing the transport of signaling molecules like YAP/TAZ, which are critical regulators of mechanosensitive gene expression [42]. Stretching of the NE increases pore permeability, allowing the translocation of transcription factors into the nucleus to activate stress-responsive genes. Additionally, the NE connects to the cytoskeleton through the linker of nucleoskeleton and cytoskeleton (LINC) complex, enabling the direct transmission of extracellular mechanical forces to the chromatin.

1.4.2.3. Emerging Insights from Literature

Recent studies have expanded our understanding of how nuclear mechanics contribute to cellular function and pathology. For example, alterations in nuclear stiffness and mechanotransduction pathways have been linked to cancer progression and metastasis. Loss of lamin A/C or dysregulation of chromatin organization has been implicated in enhanced nuclear deformability, enabling cancer cells to navigate through dense extracellular matrices during metastasis [43-44]. Additionally, mutations in nuclear envelope proteins, such as lamins, can disrupt mechanotransduction, contributing to laminopathies and other diseases associated with defective nuclear mechanics [33].

The interplay between the nuclear lamina, chromatin, and the NE highlights the nucleus's role as a central hub for integrating mechanical and biochemical signals. Advances in high-resolution imaging and biomechanical assays continue to unravel the complexity of nuclear mechanotransduction, paving the way for targeted therapies in mechanopathologies, including cancer and fibrotic diseases.

In conclusion, nuclear mechanotransduction is a multifaceted process involving the structural and functional components of the nucleus. The nuclear lamina, chromatin, and nuclear envelope each play distinct but interconnected roles in sensing and transmitting mechanical signals, underscoring the nucleus's pivotal role in cellular mechanobiology.

1.4.3. The LINC Complex: A Critical Mediator of Nuclear Mechanotransduction

The Linker of Nucleoskeleton and Cytoskeleton (LINC) complex is an essential structural and functional mediator in the mechanotransduction pathway, facilitating the direct transmission of mechanical forces from the extracellular environment to the nucleus. By connecting the nuclear envelope (NE) to the cytoskeleton, the LINC complex serves as a dynamic interface that integrates signals from the extracellular matrix (ECM), cytoskeleton, and nucleus, thereby orchestrating cellular responses to mechanical stress [44-45; 66]. This connection enables cells to adapt to their physical surroundings and maintain structural integrity under various physiological and pathological conditions.

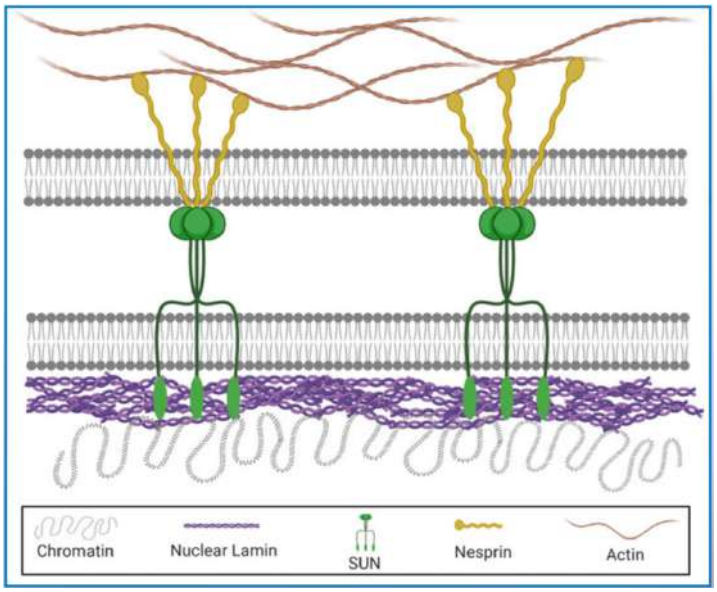

Figure 1-6. THE LINC complex: a schematic representation.

1.4.3.1. Structure and Composition of the LINC Complex

The LINC complex is primarily composed of nesprins and SUN (Sad1 and UNC-84 homology) proteins, which are transmembrane proteins located in the outer nuclear membrane (ONM) and inner nuclear membrane (INM), respectively. Nesprins extend into the cytoplasm and interact with cytoskeletal filaments, such as actin, microtubules, and intermediate filaments, creating a direct link between the cytoskeleton and the nuclear envelope [46]. Nesprins possess a conserved KASH (Klarsicht, ANC-1, and Syne Homology) domain that anchors them to SUN proteins within the perinuclear space. On the nuclear side, SUN proteins connect to the nuclear lamina, a dense network of intermediate filaments composed of lamin A/C and lamin B, which provides mechanical support to the nucleus and anchors chromatin [47].

1.4.3.2. Functional Roles of the LINC Complex

Force Transmission and Nuclear Deformation

The LINC complex plays a pivotal role in transmitting forces exerted on the ECM through the cytoskeleton to the nucleus. This force transmission causes nuclear deformation, which can alter chromatin organization, gene expression, and nuclear pore permeability, ultimately influencing cellular behavior. For example, during cell migration through confined spaces, the LINC complex enables the nucleus to respond to mechanical constraints by reorganizing its structure and reducing stiffness [48].

Nuclear Positioning and Shape Maintenance

The LINC complex ensures proper nuclear positioning within the cell, which is critical for cellular polarity, division, and migration. Disruption of nesprins or SUN proteins leads to misaligned nuclei, impaired migration, and altered cellular mechanics, as demonstrated in studies on laminopathies and other diseases associated with defective nuclear-cytoskeletal connectivity [49]. Furthermore, the LINC complex maintains the elliptical shape of the nucleus, ensuring optimal spatial organization for chromatin and nuclear processes.

Mechanotransduction and Gene Regulation

By transmitting mechanical signals, the LINC complex plays a central role in activating mechanosensitive pathways that regulate gene expression. For instance, mechanical stress transmitted through the LINC complex can lead to chromatin remodeling and activation of mechano-responsive genes, such as those involved in tissue remodeling and repair. This function is particularly important in cells exposed to dynamic mechanical environments, such as endothelial cells, fibroblasts, and osteocytes [42].

Pathophysiological Implications

Dysregulation of the LINC complex has been implicated in several diseases, including laminopathies, cancer, and cardiovascular disorders. In cancer, altered expression of nesprins and SUN proteins compromises nuclear stiffness and mechanotransduction, facilitating tumor cell invasion and metastasis [44]. In cardiac and skeletal myopathies, mutations in nesprin or SUN protein genes disrupt nuclear positioning and force transmission, contributing to disease progression.

1.4.3.3. Implication for tumorigenesis

The Linker of Nucleoskeleton and Cytoskeleton (LINC) complex serves as a critical structural and functional bridge between the nuclear envelope and the cytoskeleton. This intricate system enables the transmission of mechanical signals across cellular compartments, influencing processes such as mechanotransduction, nuclear integrity, and gene regulation. In the context of cancer, alterations in the LINC complex have profound effects, driving tumorigenesis, enhancing cellular plasticity, and facilitating invasive and metastatic behaviors.

Downregulation and Mutation of LINC Components

One of the key observations in cancer research is the consistent downregulation of LINC complex components in tumor cells. Proteins such as SUN1/2, located within the inner nuclear membrane, and nesprins, which span the outer nuclear membrane, exhibit significantly reduced expression in various malignancies. In breast cancer tissues and cell lines, SUN1/2 and nesprin-2 expression levels are markedly diminished, correlating with tumor aggressiveness and progression [50]. Additionally, mutations in nesprin genes, such as SYNE1 and SYNE2, are frequently identified in cancers of the breast, colon, and gastrointestinal tract [51]. These molecular disruptions impair nuclear-cytoskeletal connectivity, undermining the cell's ability to maintain structural stability and respond to mechanical stimuli.

Mechanotransduction Disruption and Tumor Plasticity

Mechanotransduction, the cellular process of sensing and responding to mechanical forces, is critically dependent on the functionality of the LINC complex. In cancer cells, the dysregulation of this system leads to significant impairments in force transmission from the extracellular matrix (ECM) to the nucleus. This loss of mechanosensitivity allows cancer cells to bypass mechanical constraints within the tumor microenvironment, enabling them to migrate and invade surrounding tissues more effectively [52]. Moreover, the disruption of the LINC complex alters chromatin organization and gene expression, promoting oncogenic signaling pathways that drive uncontrolled proliferation and survival.

Nuclear Mechanics and Genomic Instability

The LINC complex also plays a vital role in maintaining nuclear mechanics and genomic stability. The connection between nesprins and SUN proteins strengthens the nuclear envelope and supports chromatin organization. In cancer cells, the disruption of these interactions leads to nuclear deformation and fragility. During migration through confined spaces, such weakened nuclei are prone to rupture, resulting in DNA damage and genomic instability. This instability not only fuels tumor progression but also contributes to intratumoral heterogeneity, a hallmark of advanced cancers [49].

Enhanced Metastatic Potential

The loss of LINC-mediated nuclear-cytoskeletal connectivity enhances cancer cell adaptability, particularly in overcoming physical barriers during invasion and metastasis. Mechanosensitive transcription factors, such as YAP/TAZ, are hyperactivated in the absence of proper LINC function, driving gene expression programs associated with cell migration, proliferation, and survival [42]. These alterations allow tumor cells to detach from primary sites, invade distant tissues, and establish secondary tumors.

Therapeutic Implications

The critical role of the LINC complex in maintaining cellular and nuclear integrity highlights its potential as a therapeutic target in cancer. Restoring the expression or function of SUN proteins and nesprins may help reinforce nuclear stability and reduce metastatic capabilities. Additionally, targeting downstream pathways activated by LINC dysfunction, such as YAP/TAZ signaling, represents a promising strategy for limiting

tumor progression. Small molecules, gene therapies, or biologics designed to modulate LINC complex components could potentially mitigate the invasive and metastatic behavior of cancer cells.

1.4.3.4. Future Directions

Recent studies highlight the versatility of the LINC complex in cellular mechanobiology. Advanced imaging techniques and biophysical tools have uncovered new roles for the LINC complex in nuclear shape adaptation and chromatin organization under varying mechanical conditions [53]. Additionally, therapeutic strategies targeting LINC complex components are being explored for diseases involving aberrant mechanotransduction, such as fibrosis and certain cancers.

1.5. Purpose of the Study and Experimental Research Methods

In this study, we propose that variations in mechanical load significantly influence the proliferation of cancer cells in the heart, potentially providing an explanation for the notably low incidence of cardiac tumors. To investigate this hypothesis, we employed a combination of *in vivo* and *ex vivo* experimental approaches to dissect the interplay between mechanical forces and cancer cell behavior within the myocardium. Specifically, we demonstrated that mechanical load suppresses, while tissue unloading enhances, cancer cell proliferation within the cardiac microenvironment.

1.5.1. Heterotopic Heart Transplantation (HHT)

To investigate the effects of mechanical forces on cancer cell proliferation within the myocardium, we utilized two complementary methodologies. The first involved the development of an *in vivo* model of cardiac unloading via heterotopic heart transplantation (HHT). In this model, a donor heart was transplanted into the cervical region of a syngeneic recipient mouse. While the donor heart remained perfused through the recipient's circulation, it was mechanically unloaded, allowing us to isolate the effects of reduced mechanical stress on cardiac tissue. This model preserved critical physiological characteristics such as cellular composition and vascularization while eliminating cyclic mechanical strain, providing a unique platform to study mechanical unloading in a living organism.

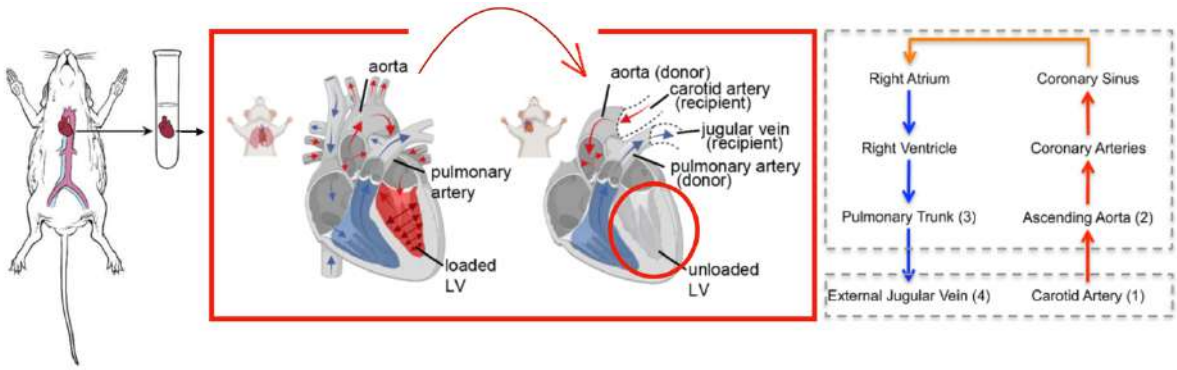

Figure 1-7. Heterotopic Heart Transplantation: a schematic representation.

Studies in humans have previously shown that mechanical unloading of the heart can restore the replicative capacity of terminally differentiated cells, such as cardiomyocytes [3]. This suggests that mechanical pressure, such as that caused by ventricular filling, may play a key role in inhibiting cellular proliferation. Given these insights, the HHT model emerged as a valuable tool for studying the effects of mechanical unloading, initially being developed to investigate immunological mechanisms during acute and chronic graft rejection [54-55].

The HHT model has traditionally involved transplanting a donor heart into an ectopic site in the recipient, typically the abdomen. In the abdominal HHT model for mice, the donor heart's ascending aorta is anastomosed to the recipient's abdominal aorta, and the pulmonary artery is connected to the inferior vena cava [56-57].

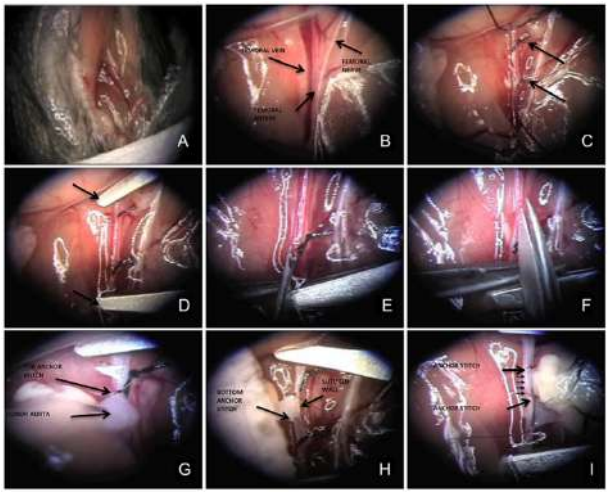

Figure 1-8. An Extraperitoneal Technique for Murine Heterotopic Cardiac Transplantation: surgical times.

However, our study employed a cervical heterotopic transplant model, wherein the donor heart is transplanted into the recipient's neck region. In this model, the recipient's external jugular vein and common carotid artery are anastomosed to the donor heart's pulmonary artery and aorta, respectively [58]. This configuration ensures the donor heart

receives oxygenated blood via the recipient's circulation while mechanically unloading the left ventricle.

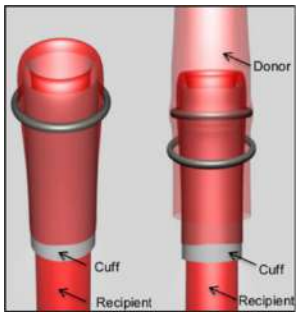

Figure 1-9. A schematic representation of cuffing: the recipient vessel is everted directly on the cuff to subsequently receive the donor vessel.

This model provided an exceptional opportunity to study how unloading influences cellular behavior, including proliferation and gene expression, in a controlled physiological context. Importantly, the heterotopically transplanted heart retained characteristics of a native heart, such as its cellular composition, extracellular matrix, contractile activity, and vascular integrity, while being subjected to significantly altered mechanical forces.

The implications of this model extend beyond basic research into cancer cell proliferation within the myocardium. By leveraging the HHT approach, we aim to elucidate how mechanical unloading can alter cellular and molecular pathways, with a particular focus on understanding how the absence of cyclic mechanical stress impacts cancer cell growth, chromatin remodeling, and gene expression.

1.5.2. Engineered Heart Tissues (EHTs)

Second, we employed Engineered Heart Tissues (EHTs), an advanced tissue engineering platform that allows the generation of three-dimensional (3D) cardiac tissues outside the body. EHTs mimic key structural and functional properties of the native myocardium, providing a highly controlled environment to investigate the effects of mechanical loading and unloading on cellular behavior. This system is particularly advantageous for modeling conditions such as volumetric compression and mechanical unloading, which are challenging to replicate in vivo.

1.5.2.1. Historical and Technical Advances in EHTs

EHT technology was first introduced in the early 2000s by Eschenhagen et al., who developed a method to construct functional cardiac tissues using neonatal rat cardiomyocytes embedded in a hydrogel composed of type I collagen and Matrigel. [59]. Over time, these constructs matured into contractile myocardial cultures, offering a platform to study cardiomyocyte behavior, contractile dynamics, and

mechanotransduction mechanisms. Subsequent refinements in 2010 further enhanced the technology, particularly by adapting the EHT system for high-throughput applications. By miniaturizing the hydrogel constructs into multi-well plate formats, researchers could assess contractile forces across multiple samples simultaneously, greatly increasing the reproducibility and scalability of experiments [60].

1.5.2.2. Methodological Improvements

Two pivotal improvements were introduced during this refinement. First, type I collagen was replaced with fibrinogen, a biopolymer that forms fibrin upon thrombin-mediated polymerization. Fibrin exhibits superior elasticity and softness, closely mimicking the mechanical properties of in vivo fibrin structures. Additionally, fibrin supports the covalent binding of growth factors and is biodegradable, making it an ideal scaffold for cardiac tissue engineering. However, aprotinin supplementation was required to prevent fibrin degradation during the culture period [61]. Second, silicone anchors and Teflon spacers were incorporated into the system. These modifications allowed the creation of molds within a 24-well plate format, where cardiomyocytes could attach to paired silicone posts to form 3D tissue constructs. These posts provided a stable framework for the developing tissues while enabling precise measurements of contractile forces under different experimental conditions [60].

1.5.2.3. Cultivation and Experimental Application

In practice, EHTs are cultured over 15–30 days under tightly regulated conditions, allowing for tissue maturation and functional development. This setup enables researchers to manipulate mechanical forces with high precision, making it possible to model mechanical loading and unloading scenarios observed in vivo.

1.5.2.4. Integration into this study

For this study, EHTs were instrumental in evaluating the role of mechanical forces on cancer cell proliferation within the cardiac microenvironment. By subjecting EHTs to controlled mechanical stress or unloading conditions, we could simulate the biomechanical environment of the heart and study its effects on cellular behavior in detail.

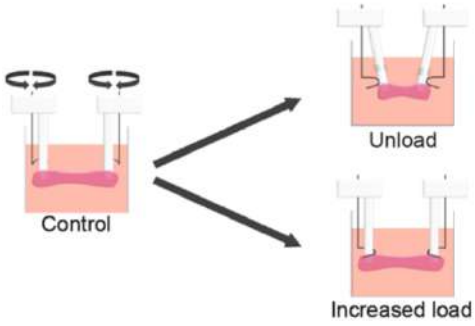

Figure 1-10. Schematic representation of control EHT (left) and its adaptation to induce either unload (top right) or increased load (bottom right).

1.5.3. Comparison Between Cardiac and Extra-Cardiac Metastases Derived from Human Samples

Furthermore, to deepen our understanding of the mechanisms underlying these effects, we analyzed human samples of cardiac metastases and compared them to extra-cardiac lesions from the same patients. This investigation aimed to unravel the molecular and cellular pathways that inhibit cancer cell proliferation within the heart, emphasizing the protective role of mechanical forces in this unique organ environment.

2. Methods

2.1. Cell Culture

In this study, two murine cell lines were utilized: LG1233 [160] and CT26-Cas9-hyg (GeneCopoeia). The LG1233 cells originate from a pulmonary adenocarcinoma and were genetically engineered to stably express green fluorescent protein (GFP). On the other hand, the CT26-Cas9-hyg cells are derived from a colorectal carcinoma and were engineered to stably express both GFP and the CRISPR-associated protein Cas9.
LG1233 cells were cultured in Dulbecco's Modified Eagle Medium (DMEM) supplemented with GlutaMAX (Gibco; glucose concentration: 1 g/L), whereas CT26-Cas9-hyg cells were maintained in Roswell Park Memorial Institute (RPMI) 1640 medium (Corning; glucose concentration: 4.5 g/L). Both media were enriched with 10% fetal bovine serum (FBS) and 0.2% penicillin/streptomycin.
For experimental procedures involving LG1233 cells, the same DMEM-based medium was used, but the glucose concentration was increased to 4.5 g/L to match the experimental requirements.
This standardized approach ensured the optimal growth and stability of the engineered cell lines while maintaining their functional characteristics throughout the study.

2.2. Isolation of Neonatal Rat Cardiomyocytes

Neonatal Wistar rat hearts (postnatal day 0 to 3) were minced into small fragments and subjected to enzymatic digestion using a DNase/Trypsin-based protocol to obtain single-cell suspensions. Following digestion, the collected cells were centrifuged to remove debris, filtered through a 100 µm cell strainer to ensure uniformity, and resuspended in a culture medium composed of:

DMEM (Biochrom F0415)
10% heat-inactivated fetal bovine serum (Thermo Fisher 26140-079)
1% penicillin/streptomycin (Thermo Fisher 15140-122)
1% L-glutamine (200 mM, Gibco)

This process ensured the generation of viable, high-quality cardiomyocytes suitable for subsequent experimental applications.

2.3. Comprehensive Protocol for Cardiac Mechanical Unloading Studies

2.3.1. Ethical Compliance and Animal Housing

All animal experiments were conducted in accordance with the Directive 2010/63/EU of the European Parliament on animal experimentation and in compliance with European and international guidelines (EC Council Directive 86/609, OJL 34, 12 December 1987). The study was approved by the ICGEB Animal Welfare Board, the Ethical Committee, and the Austrian Ministry of Education, Science, and Culture (BMWFW-66.011/0155-WF/V/3b/2017). Animals were housed in ventilated cages with a 12-hour light/dark cycle. Environmental conditions were controlled, maintaining a temperature of 20–22 °C and relative humidity between 45–65%.

2.3.2. Heterotopic Heart Transplantation

The study utilized a modified heterotopic heart transplantation (HHT) technique in which vessels are everted over synthetic cuffs for vascular anastomoses. This approach allowed precise modeling of cardiac mechanical unloading.

2.3.3. Heart Harvesting from the Donor Animal

Donor animals were anesthetized with an intraperitoneal injection of ketamine/domitor (75 mg/kg and 1 mg/kg) or ketamine/xylazine (100 mg/kg and 5 mg/kg). Complete immobilization and maintenance of respiration were confirmed. Sensitivity was tested by applying incremental pressure to a limb, while whisker movement was observed, initiating the procedure only after complete cessation.

The donor mouse was positioned supine on a heated platform at 37°C, and the abdomen was moistened with alcohol to prevent hair contamination. A transverse incision was made to expose the inferior vena cava, which was injected with 500 µL of heparinized saline (1:4 heparin-sodium ratio) to achieve circulatory anticoagulation. The thoracoabdominal cavity was opened along the costal margins, the diaphragm was severed, and the sternum was rotated cranially to expose the heart. The superior vena cavae were isolated and cut to induce venous bleeding, facilitating cardiac flushing with Custodiol® HTK solution at 4°C, either retrogradely (via the ascending aorta) or anterogradely (via the inferior vena cava). The heart was excised and preserved in cardioplegic solution until transplantation.

2.3.4. Cervical Cardiac Transplantation in the Recipient Animal

Recipient mice were anesthetized as described above, and their right cervical region was prepared for surgery. The external jugular vein and common carotid artery were isolated, and cuffs were attached to these vessels using an eversion technique. The harvested heart was placed in an inverted position (with the pulmonary artery oriented laterally and the aorta medially) in the cervical region. The pulmonary artery was anastomosed to the external jugular vein cuff, and the aorta was anastomosed to the carotid artery cuff.

Clamps were sequentially removed to restore perfusion, and the transplanted heart resumed sinus rhythm.
Postoperative analgesics, including carprofen (4 mg/kg) and buprenorphine (0.1 mg/kg), were administered subcutaneously every 12 hours for up to five days to minimize pain. The animals were housed in cages with access to soft food and water.

2.3.5. Carotid-Aortic and Jugulo-Pulmonary Anastomoses

The pulmonary artery of the graft was aligned with the cuffed external jugular vein and secured with a circumferential 8-0 silk ligature, completing the jugulo-pulmonary anastomosis. Similarly, the aorta of the graft was aligned with the cuffed common carotid artery and secured with a silk ligature, completing the carotid-aortic anastomosis. Once clamps on the recipient's vessels were removed, the grafted heart was perfused and resumed contractile activity.

2.3.6. Injection of Tumor Cells and Monitoring

Following recovery, a solution containing murine lung carcinoma cells (LG1233, 1×10^5 cells/animal) was injected tangentially into the myocardium of either the transplanted or native hearts. To label proliferating cells, 5'-ethynyl-2'-deoxyuridine (EdU) was administered intraperitoneally on days 1, 3, 7, 14, 18, 20, and 24 after tumor implantation. Animals were weighed weekly and monitored for clinical signs, including apathy, reduced nutritional intake, and weight loss exceeding 10–15%. If necessary, animals were humanely euthanized via isoflurane inhalation before reaching the experimental endpoint.

2.3.7. Integration with Experimental Goals

This study was conducted in collaboration with the Daniel Swarovski Research Laboratory (Innsbruck), which provided technical expertise and training for mastering these complex procedures. The use of heterotopic heart transplantation enabled the modeling of cardiac mechanical unloading, creating a unique system to study the effects of biomechanical forces on tumor proliferation.
In parallel, LG1233 murine lung carcinoma cells were used to explore whether mechanical unloading in the transplanted heart could create conditions conducive to tumor cell proliferation. By combining mechanical manipulation and tumor cell implantation, this protocol provided critical insights into the interplay between mechanical stress, cardiac biology, and cancer growth.

2.3.8. Significance of the Model

This comprehensive protocol bridges technical precision and biological inquiry, allowing for the reproducible study of cardiac unloading. The combination of HHT models, tumor cell implantation, and proliferative labeling with EdU facilitates detailed investigations into how mechanical forces regulate cancer cell behavior within the myocardium. These

findings hold potential implications for understanding cardiac resistance to cancer and may inform novel therapeutic strategies.

2.4. Generation and Modulation of Fibrin-Based Engineered Heart Tissues (EHTs)

Fibrin-based Engineered Heart Tissues (EHTs) provide a robust and reproducible platform for studying cardiac biology and tumor cell behavior under controlled mechanical conditions. By combining neonatal cardiomyocytes (CMs) and cancer cell lines (e.g., CT26, LG1233, B16), EHTs allow for the investigation of cell proliferation, biomechanical interactions, and load-dependent cellular responses. This protocol describes the preparation, maturation, and modulation of fibrin-based EHTs, along with a custom mechanical load system for precise experimental manipulation.

2.4.1. Cell Preparation and Reconstitution Mixture

CMs were isolated from neonatal Wistar rats (postnatal days 0–3) using the Neonatal Cardiomyocyte Dissociation Kit(Miltenyi, 130-098-373). The reconstitution mixture for EHTs was prepared with the following components:

Cardiomyocytes: 6×10^6 cells/EHT
Bovine fibrinogen: 5 mg/mL (Sigma-Aldrich F8630)
DMEM 10X: 20% (Fisher Scientific, 10134902)
Heat-inactivated horse serum: 10% (Thermo Fisher, 26050-088)
Penicillin/streptomycin: 1% (Thermo Fisher, 15140-122)
Thrombin: 3 µL of 100 U/mL (Merck T7513)

For cancer cell-containing EHTs, specific concentrations of tumor cells were added to the reconstitution mixture:

LG1233 cells: 2×10^5 cells/EHT
B16 melanoma cells: 2×10^5 cells/EHT
CT26 colon carcinoma cells: 3×10^5 cells/EHT

2.4.2. Preparation of Agarose Molds and Casting Setup

Molds were created by adding 1.5 mL of 2% agarose (Invitrogen, 15510-027) into the wells of a 24-well culture plate. Once the agarose solidified, Teflon spacers (12 × 3 × 4 mm) were removed, creating casting wells. Silicone posts were placed within the molds, and 30G needles (Meso-Relle) were bent into hook shapes and positioned near the anchoring areas of the silicone posts. This hook design was chosen to counteract the spontaneous reduction in EHT length that occurs during development due to fibroblast contraction.

The reconstitution mixture (100 µL) was carefully pipetted into the molds containing the silicone posts, and the setup was incubated in a humidified cell culture incubator at 37°C and 7% CO_2 for 2 hours to allow fibrinogen polymerization.

2.4.3. EHT Maturation and Maintenance

After fibrinogen polymerization, 300 µL of EHT culture medium was added to each well to facilitate the gentle removal of the constructs from the molds. The racks containing EHTs were transferred to fresh 24-well culture plates, and the culture medium was replaced every two days. The culture medium consisted of:

DMEM: Biochrom F0415
Horse serum: 10% (Thermo Fisher, 26050-088)
Penicillin/streptomycin: 1% (Thermo Fisher, 15140-122)
Insulin: 10 µg/mL (Sigma-Aldrich I9278)
Aprotinin: 33 µg/mL (Merck A1153)

EHTs were monitored daily, and maturation was confirmed 7–10 days post-casting by the appearance of consistent and synchronous beating. During this period, the hooks were intentionally kept free from contact with the silicone posts to avoid interference with the spontaneous reduction in EHT length.

2.4.4. Adjustable Mechanical Load System

A custom hook-based system was developed to allow precise modulation of mechanical load on EHTs. The design enabled three distinct configurations for mechanical loading:

1. Standard Load (Resting Position): The default configuration where the load was determined by the inherent elasticity of the silicone posts.
2. Unloaded Position: The convex side of the hook was rotated against the silicone posts, reducing the distance between the two ends of the EHT and minimizing tension.
3. Increased Load Position: The concave side of the hook was rotated around the silicone post, increasing stiffness and applying a higher mechanical load to the EHT.

The adjustable mechanical load system allowed precise control over tension, enabling the investigation of how load influences tissue development, CM behavior, and cancer cell proliferation.

2.4.5. Load Modulation Experiments

To study the effects of mechanical load on CM and tumor cell proliferation, EHTs were subjected to:

EdU pulse-labeling: Administered during load modulation experiments lasting 72 hours.
Unloading conditions: Simulated using calcium-free DMEM (Thermo Fisher, 21068028) for 5 days.

The custom hook system ensured consistent and reproducible application of mechanical forces, enabling detailed analysis of biomechanical effects.

2.4.6. Applications and Significance

This protocol provides a robust system for generating functional fibrin-based EHTs with tunable mechanical properties. It has several applications:

Cardiac Biology: Investigating the effects of load modulation on cardiomyocyte contractility, maturation, and survival.

Cancer Research: Exploring tumor cell proliferation, invasion, and interactions with cardiac tissue under varying mechanical stresses.

Drug Testing: Evaluating therapeutic efficacy in a 3D, physiologically relevant environment.

The integration of neonatal cardiomyocytes and cancer cells within fibrin-based scaffolds enables a deeper understanding of the interplay between biomechanical forces and cellular behavior. This system represents a valuable tool for advancing research in cardiac and oncological pathophysiology.

2.5. siRNA Transfection and Lentiviral Transduction in Cancer Cells

To investigate the role of specific genes in cancer cell behavior, siRNA transfection and lentiviral transduction were employed. Cancer cells (CT26, LG1233, or B16) were transfected using the “Lipofectamine RNAiMAX” reagent (Invitrogen, 13778-150), following the manufacturer’s protocol.

2.5.1. siRNA Transfection Protocol

siRNAs targeting specific genes were prepared using Horizon siGENOME SMARTpools, each containing four siRNAs per target. The genes targeted were:

Syne1, encoding Nesprin-1 (Cat # M-062644-00-0005)

Syne2, encoding Nesprin-2 (Cat # M-056764-02-0005)

Syne3, encoding Nesprin-3 (Cat # M-052180-01-0005)

Syne4, encoding Nesprin-4 (Cat # M-054687-01-0005)

Sun1, encoding SUN1 (Cat # M-040715-00-0005)

Sun2, encoding SUN2 (Cat # M-041247-01-0005)

Ubc, encoding Ubiquitin-C (positive control; Cat # M-019408-01-0010)

Kdm4c and Kdm4d, encoding lysine demethylases 4C and 4D, respectively (Cat # M-051504-00-0005, Cat # M-052542-01-0005)

Non-Targeting Control siRNA (NT4; D-001210-04-20), serving as a negative control.

siRNA solutions were diluted in opti-MEM medium (Life Technologies 31985-047) to a final concentration of 50 nMper siRNA and dispensed into 96- or 6-well plates. Lipofectamine RNAiMAX reagent was diluted in opti-MEM and added to the siRNA-containing wells. After 30 minutes, cancer cells were seeded onto the siRNA-laden wells at a concentration of 1.5×10^4 cells/cm^2.

For 2D cultures, the medium was replaced the day after transfection, and cells were fixed after 5 days for downstream analysis.

For EHT incorporation, transfected cells were harvested 12 hours post-transfection using trypsinization and introduced into the EHT casting mixture at a concentration of 3×10^4 CT26 or LG1233 cells per EHT.

2.5.2. Lentiviral Transduction Protocol

For stable gene silencing, cancer cells were transduced with lentiviral vectors containing short-hairpin RNAs (shRNAs) targeting Syne2 (Origene TL517485V) or a scramble shRNA control (Origene TR30021V) at a multiplicity of infection (MOI) of 1. Transduced cells were cultured for 48 hours, followed by selection with 1 µg/mL puromycin for 72 hours to ensure stable knockdown.

2.5.3. Incorporation into EHT Models

After transfection or transduction, cancer cells were introduced into the fibrin-based EHTs as previously described. The cells were added to the reconstitution mixture containing cardiomyocytes, and the EHTs were cultured under controlled conditions for maturation.

2.5.4. Controls and Experimental Validity

A pool of four siRNAs for each targeted gene ensured robust downregulation of the target. The inclusion of Ubc siRNAas a positive control and a non-targeting siRNA control (NT4) ensured specificity and validated the transfection efficiency.

This protocol allows efficient transient or stable knockdown of genes associated with the LINC complex and related pathways, enabling detailed analysis of the impact of mechanical cues and gene expression on cancer cell behavior within EHT models.

2.6. Histology and Immunostaining Protocol

Hearts and Engineered Heart Tissues (EHTs) were fixed in 10% formalin in PBS, embedded in paraffin, and sectioned at a thickness of 4 µm using a microtome (Leica). To prepare the sections for staining, paraffin was removed through a sequential process involving heat treatment (60°C for 1 hour) followed by two xylene baths (30 minutes each). Rehydration was achieved through a series of ethanol dilutions in descending concentrations.

2.6.1. Antigen Retrieval and Permeabilization

Antigen retrieval was performed by boiling the sections in a retrieval buffer containing 10 mM Tris base, 1 mM EDTA, and 0.05% Tween 20 at pH 9.0 for 20 minutes in a microwave. After retrieval, sections were rinsed three times in water and permeabilized for 20 minutes in PBS containing 0.25–0.5% Triton X-100.

2.6.2. EdU Detection

EdU incorporation was visualized using the Click-IT EdU 647 Imaging Kit (Thermo Fisher C10247), following the manufacturer's protocol.

2.6.3. Blocking and Primary Antibody Staining

To reduce non-specific binding, tissue sections were incubated in a blocking solution consisting of 10% horse serum and 0.25% Triton X-100 in PBS for 30 minutes. Following blocking, the sections were incubated overnight at 4°C with primary antibodies diluted 1:100 in the blocking solution. The primary antibodies used included:

Anti-cardiac troponin I (Abcam ab47003)
Anti-cardiac troponin T (Abcam ab8295)
Anti-phospho-Histone H3 (Ser10) (Merck 06-570)
Anti-Ki67 (Abcam ab15580)
Anti-PCM1 (Merck HPA023374)
Anti-Histone H3 (trimethyl K9) (Abcam ab176916)
Anti-Melanoma gp100 (Abcam ab137078)

2.6.4. Secondary Antibody Detection and Nuclear Staining

Primary antibody detection was performed using Alexa Fluor-conjugated secondary antibodies (Thermo Fisher). To visualize nuclei, sections were counterstained with DAPI (Thermo Fisher 62247), and slides were mounted with Fluoromount-GTM Mounting Medium (Thermo Fisher 00-4958-02).

2.6.5. Cross-Sectional Area Analysis

Cross-sectional area analysis was conducted on sections stained with an anti-dystrophin antibody (Abcam ab15277) using the VECTASTAIN ABC Kit (Vectorlabs PK-6100) and ImmPACT DAB substrate (Vectorlabs SK-4105). A minimum cross-sectional area threshold of 40 μm^2 was applied for quantification.

This comprehensive histology and immunostaining protocol enables precise localization and quantification of molecular markers and cellular structures in both cardiac tissues and EHTs, supporting investigations into cell proliferation, tissue architecture, and disease pathology.

2.7. Heart and EHT Mechanical Simulation

To investigate the mechanics of the heart under normal and unloaded conditions, as well as the mechanical properties of Engineered Heart Tissues (EHTs) under different loading scenarios, finite element models were developed for both systems.

2.7.1. Finite Element Simulation of Cardiac Mechanics

A finite element model of the rodent left ventricle (LV) was constructed using a simplified truncated prolate ellipsoid geometry with the following dimensions:

Wall thickness: 1.5 mm

Short-axis radius: 4 mm

Long-axis radius: 8 mm

Myofiber orientations were assigned to rotate from -60° to +60° between the endocardium and epicardium, while sheet orientations were orthogonal to both the fibers and the gradient direction spanning the epicardium to the endocardium.

Systolic contraction was simulated using a FEniCS-based solver for cardiac mechanics, employing P2 finite elementsfor displacement. The boundary conditions were:

Robin boundary condition applied at the epicardium.

Imposed endocardial pressure to simulate intracavity forces.

Fixed motion at the basal plane in the longitudinal direction.

The active contraction was modeled using an active strain approach, where the total deformation tensor was multiplicatively decomposed into active and passive components. Contraction along the fiber direction was controlled using an activation parameter (γ). The myocardium was represented as a transversely isotropic, slightly compressible hyperelastic material.

Simulations were conducted under two conditions:

1. Control (Normal Load): End-systolic pressure (ESP) was set to 15 kPa.
2. Unloaded: Cavity pressure was removed (ESP = 0 kPa).

For each case, deviatoric Cauchy stresses were computed in the fiber, sheet, and sheet-normal directions and averaged across the entire volume of the LV geometry.

2.7.2. Finite Element Simulation of EHT Mechanics

To model the mechanical behavior of EHTs, a cylindrical geometry was created with:

Length: 4000 μm

Radius: 300 μm

Cardiac fibers were assigned along the longitudinal axis of the cylinder to mimic the alignment of cardiomyocytes. A Robin-type boundary condition was applied at both ends to represent the interaction between the EHT and the supporting silicone posts.

Calibration and Control: The spring constant of the Robin boundary condition was calibrated to match experimental data, reproducing an observed ~15% systolic shortening under normal conditions.

Load Modulation Simulations:

1. Increased Load (Stiffened Posts):
    - The spring constant was increased by 10×, simulating stiffer silicone posts.
    - This resulted in a reduction of systolic shortening to ~11%.
2. Unloading (Reduced Resistance):
    - The spring constant was decreased by 10×, representing almost no resistance to shortening.
    - This allowed the EHT to shorten by approximately 20% during contraction.

For each condition, deviatoric Cauchy stresses were computed across the mesh and volume-averaged over a 300 μm-long segment of the cylinder to quantify mechanical stress distribution.

2.7.3. Significance of the Simulations

These simulations provide insights into:

The effects of mechanical unloading on the rodent LV, shedding light on stress redistribution under unloaded conditions.

The impact of load modulation on EHT contraction and stress distribution, offering a framework to study the interplay between mechanical forces and cellular function.

By integrating experimental data with computational modeling, these approaches bridge in vitro EHT studies with in vivo cardiac biomechanics, enabling more comprehensive investigations into cardiac physiology and disease.

2.8. Spatial Transcriptomics Analysis

Spatial transcriptomics was conducted on human cancer samples, following approval by the Ethical Committees of the University of Trieste and Centro Cardiologico Monzino. Tissue sections were prepared by cutting 5 μm slices from formalin-fixed paraffin-embedded (FFPE) tissue blocks and mounting them onto Superfrost slides (Thermo Fisher).

The transcriptomic analysis was performed using the NanoString GeoMx Digital Spatial Profiling (DSP) platform in Seattle, WA, USA. This advanced technique allows for high-resolution gene expression profiling of specific tissue regions while preserving spatial context.

Tissue Preparation and Marker Selection

Tissue sections were stained with cell-type-specific markers to identify regions of interest (ROIs) for downstream gene expression analysis:

Troponin I: To label cardiomyocytes (CMs).

Pan-cytokeratin: To identify lung and colorectal cancer cells.

PMEL: To mark melanoma cells.

2.8.1. Selection of Regions of Interest (ROIs)

ROIs were carefully selected based on the following criteria:

Each ROI contained at least 300 cells of the target cell type to ensure robust transcriptomic analysis.

Areas with fibrosis or necrosis were systematically excluded to maintain the integrity and relevance of the sampled regions.

This approach ensures precise spatial mapping of gene expression patterns within the tumor microenvironment and cardiac tissues, enabling a detailed understanding of the cellular and molecular interactions in these contexts.

2.9. Video-Optical Recording and Analysis of EHT Contraction

The contractile activity of Engineered Heart Tissues (EHTs) was recorded using an Andor Neo sCMOS camera integrated into a Nikon Eclipse Ti microscope equipped with Plan UW objectives (1X or 2X). EHTs were maintained in a humidified incubator (OkoLab) set to 37°C and 7% CO_2 to preserve physiological conditions during live imaging. Recordings were performed for either 5 or 10 seconds at a high frame rate of 100 frames per second, ensuring sufficient temporal resolution for detailed analysis of contractility.

For stimulated contraction measurements, EHTs were subjected to electrical stimulation at a frequency of 4 Hz using a Hugo Sachs Elektronik Stimulator C Type 224, as previously described. This setup allowed precise assessment of both spontaneous and stimulated contractile activity under controlled experimental conditions.

To quantify contractile force, the deflection of the silicone posts anchoring the EHTs was measured. Using known geometric properties of the posts, the elastic modulus of Sylgard 184 silicone (2.6 kPa), and the post deflection distance, force was calculated based on a previously published equation:

$$F = \frac{3EI\delta}{L^3} = \frac{3\pi ER^4\delta}{4L^3}$$

where:

R: Radius of the post,

L: Length of the post,

E: Elastic modulus of the material,

δ: Measured post deflection,

I: Moment of inertia of the post, given by I=14R4I=41R4.

This equation provides a precise method for converting post deflection into force, enabling accurate quantification of mechanical properties and contractile performance of the EHTs.

This advanced imaging and analytical approach facilitates the study of mechanical dynamics and functional output in EHT models, contributing to our understanding of cardiac and cancer cell behavior under various biomechanical conditions.

2.10. Image Analysis

Image acquisition was conducted using a Nikon Eclipse Ti microscope equipped with an Andor Neo sCMOS camera. Quantitative analysis of acquired images was performed using ImageJ software (NIH, Bethesda).

2.10.1. DNA Compaction Analysis

To evaluate chromatin compaction, the coefficient of variation (CV) of DAPI intensity within individual nuclei was calculated. The CV was determined using the formula:

$$\mathrm{CV} = \frac{\sigma}{\mu}$$

where:

σ: Standard deviation of DAPI intensity values within the nucleus,

μ: Mean intensity value of the nucleus.

Highly condensed chromatin, characterized by bright chromocenters, results in a broader intensity distribution and a higher standard deviation, yielding a higher CV compared to decondensed heterochromatin, which displays more uniform DAPI staining.

2.10.2. Densitometric Analysis of H3K9me3 Intensity

The intensity of H3K9me3 staining was quantified through densitometric analysis. The integrated density of H3K9me3 staining was measured within nuclear regions of interest (ROIs) identified based on DAPI signal. This approach allowed precise quantification of histone methylation levels as an indicator of chromatin state.

2.10.3. Proliferating Cancer Cell Analysis

The number of proliferating cancer cells and the density of cancer cells within cross-sectional areas were calculated using the Cell Counter plugin in ImageJ. Proliferating cells were identified based on immunostaining for specific markers, such as Ki67 or phospho-Histone H3 (Ser10), and their nuclear localization was confirmed using DAPI counterstaining.

This comprehensive image analysis approach enables precise evaluation of chromatin organization, histone modifications, and cellular proliferation, providing valuable insights into the molecular and structural dynamics of cancer and cardiac cells within engineered tissue models.

2.11. Statistical Analysis

All results are presented as mean ± standard error of the mean (SEM). Statistical comparisons were performed using GraphPad Prism 6 software (GraphPad Software, La Jolla, California, USA).

Comparison of Two Groups: Student's *t*-test was applied to evaluate statistical differences between two groups.

Comparison of Multiple Groups: One-way ANOVA followed by Bonferroni's post-hoc test was used for comparisons between multiple sample groups and a single control group.

Comparison Across Multiple Independent Groups: Ordinary one-way ANOVA followed by Dunnett's multiple comparisons test was employed to analyze differences among multiple independent sample groups.

Statistical significance was determined based on the following *P* values:

$P \leq 0.05$ (*),

$P \leq 0.01$ (**),

$P \leq 0.001$ (***).

This rigorous statistical framework ensures reliable analysis of experimental data, enabling robust interpretation of the results.

3. Results

3.0. An in vivo heterotopic transplantation model to achieve cardiac unloading

Thanks to the experience gained at the Daniel Swarovski Research Laboratory in Innsbruck, and in particular to the expert surgical knowledge imparted to me by Ann-Vu Nguyen, I was able to dedicate myself to developing microsurgical techniques under stereoscopic guidance. This allowed me to successfully explant and subsequently transplant a murine heart from donor to recipient into the laterocervical anatomical site, specifically the jugular-carotid system of the animal.

Figure 3-01. Daniel Swarovski Forschungslabor – Innsbruck.

3.0.1. Procedural aspects developed during this experience and now considered crucial for the correct execution of the technique

3.0.1.1. During the Phase of Donor Explant

The initial stages focused on the correct, rapid, and exceedingly precise isolation of the ascending aorta and pulmonary artery, severing them to a sufficient (and necessary) length for subsequent implantation in the recipient animal. The tissue plane between the two vessels is extremely thin, almost virtual, and must be carefully separated through gentle and incremental dilations performed with specialized, very fine surgical forceps, as shown in the accompanying image.

Figure 3-02. Surgical instruments.

The aortic arterial wall is relatively robust and easily dissected from the surrounding tissues, whereas the pulmonary artery wall is softer and prone to retraction. Therefore, it is crucial to remain acutely aware of this difference during the pulmonary artery dissection phase to ensure the maximum possible length is harvested. During the final transplantation phase, this length will be a decisive factor in determining the ease or complexity of wrapping the prepared jugular cuff.

3.0.1.2. During the Phase of Vessel Preparation in the Recipient Animal

If, during the previous phase, each step is to be considered "important," in the subsequent phase, every detail of each step becomes critical for the outcome. The successful completion of the two anastomoses—aorto-carotid and pulmonary-jugular—must be achieved without any bleeding, ultimately resulting in a transplanted, beating heart (albeit without internal blood volume).

The positioning of the animal on the operating table is crucial: the mouse must be placed so that all four limbs are kept separated from the body. Specifically, a slight rotation of the animal's neck towards the left must be performed to expose the right laterocervical region as widely as possible.

Additionally, the traction applied to the thread holding the animal's teeth anchored to the upper part of the plate on which it rests serves as another method to orient and fully expose the right laterocervical area for the surgical procedure. Combined with the aforementioned considerations, this setup ensures optimal accessibility and visualization of the surgical site.

Preparation of the External Jugular Vein

The jugular vein is skeletonized and isolated first, as it is located on a more superficial plane. All venous collaterals draining into it—usually no fewer than five—are ligated and severed following cauterization. Particular attention must be paid to a larger collateral emerging from the posterolateral plane. In some cases, for a safer and more controlled section, it is advisable to ligate the vessel proximally and distally before cutting, rather than relying solely on cauterization.

Regarding the external jugular vein, its eversion onto the cuff is more accommodating in terms of length, owing to the slightly greater extensibility of venous tissue. This property facilitates the procedure and minimizes the risk of technical complications.

The most critical aspect of the vein cuffing phase is the precise identification of the lumen after severing the cranial ligature. For this step, the use of high-quality forceps with undamaged, sharp tips is highly recommended, as it ensures accurate handling and clean exposure of the vessel's lumen.

Figure 3-03. External jugular vein cuffing.

Traditional Method for Preparing the Common Carotid Artery

According to this traditional microsurgical method [58], the first step involves the sectioning of the sternocleidomastoid muscle, following extensive cauterization in order to prevent bleeding.

This step is performed to create a surgical window that provides access to the underlying planes. These planes contain the neurovascular bundle, which includes the common carotid artery and the vagus nerve. The bundle is located along the anteromedial aspect of the muscle and is enveloped in a delicate network of fibrous connective tissue trabeculae. By carefully sectioning the sternocleidomastoid muscle and exposing the neurovascular structures, this approach ensures precise and convenient visualization and access to the common carotid artery for subsequent procedures while minimizing the risk of damage to the surrounding anatomy.

Once the carotid artery has been identified, its separation from the thin venous branches surrounding it, and especially from the vagus nerve, is performed through careful blunt dissection. Subsequently, the vessel should be encircled from below in a medio-lateral direction using a blunt surgical clamp, and a ligature should be placed cranially, slightly proximal to its bifurcation (internal and external branches). By maintaining traction on the carotid artery using the pre-bifurcation ligature just applied, the artery is tied again one millimeter (at most two) more proximally, ensuring that it can then be sectioned between the ligatures.

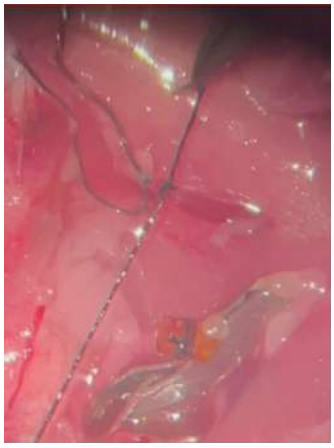

Figure 3-04. Proximal ligation 1-2 mm from the distal one, followed by sectioning.

Achieving a proper and well-skeletonized segment of the common carotid artery: thanks to the sectioning of the sternocleidomastoid muscle and the resulting space created, it is possible to extend the isolation down to the emergence of the common carotid artery from the muscle itself. Obtaining this length is essential to ensure a sufficient segment of the vessel that can be everted onto the cuff.

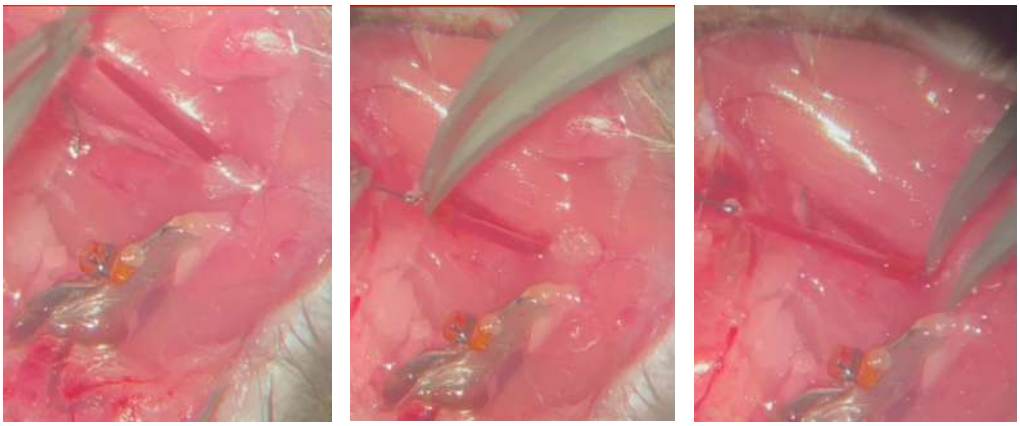

Figure 3-05. Achieving the correct length of the carotid segment through traction and tissue dissection from below.

The cuff is then inserted from above, using the proximal ligature thread as a guide, and slid along the body of the common carotid artery. The artery is clamped proximally to the cuff (at its flat portion) with a clamp that is more robust than the one used for the external jugular vein. The clamping must ensure not only that the length of the carotid artery is sufficient but also that the cuff remains unaltered in its flat portion.

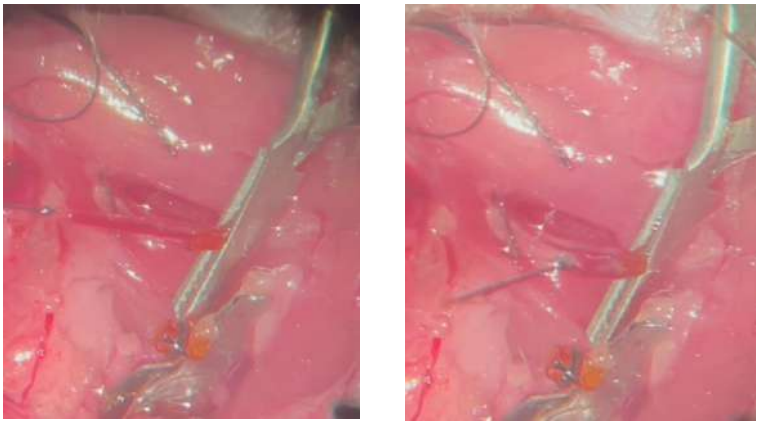

Figure 3-06. Clamping of the common carotid artery. Note the different length of the vessel after releasing it with the left clamp.

An additional critical step, which I learned directly during my experience in Innsbruck, involves securing the clamping component of the clamp under the skin on the medial aspect of the wound, first rotating it slightly upwards. This ensures stability and prevents movement when the carotid artery is everted onto the cuff. Furthermore, this technique aligns the eversion plane parallel to the microscope's field of view, facilitating precise visualization.

Figure 3-07. Clamping of the common carotid artery and upward rotation of the clamp to secure it under the animal's skin. Note the different position of the clamp compared to the previous arrangement.

Dilation of the common carotid artery is performed to facilitate its eversion onto the cuff

Using ultra-fine-tipped instruments, the vessel must be stabilized with the left hand while the right hand performs a modest dilation of the lumen to overcome the retractability of the most distal portion extending beyond the clamp.

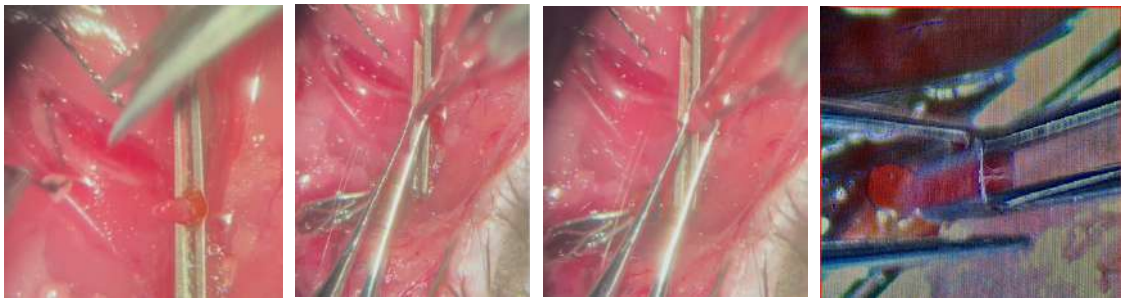

Figure 3-08. Manipulation and dilation of the common carotid artery to make it evertible onto the cuff.

This allows the lumen's rim to be securely grasped with two fine forceps and the vessel to be stretched downward to successfully perform the eversion maneuver. Once the vessel has been everted, the pre-prepared knot must be applied immediately, ensuring that it falls on the posterior plane of the cuff. This arrangement allows the second knot to be tied on the anterior plane, completing the process with precision and stability.

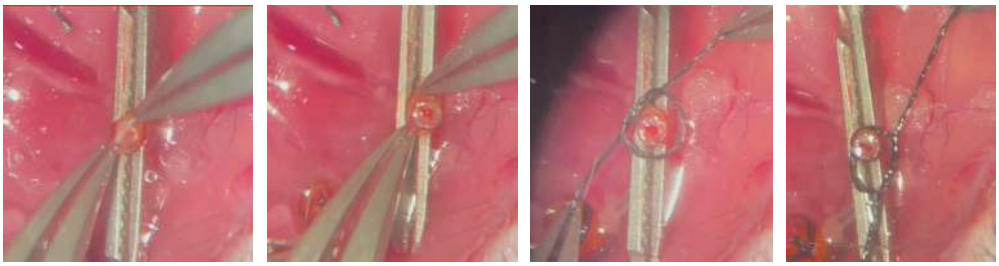

Figure 3-08. The most delicate phase of all: grasping the rim of the common carotid artery to invert it outward over the cuff. The clamp must remain in a stable position during this step. Stabilization with two knots (the first posteriorly, the second anteriorly).

The preparation of the common carotid artery carried out in this way will allow it to be wrapped with the donor ascending aorta segment, ensuring it is positioned below the knot securing the carotid artery to the cuff. From the outside, it will then be locked with an even more proximal knot, which will definitively hold together the aorta, the common carotid artery, and the cuff, thus establishing direct communication between the two lumens: that of the receiving common carotid artery and the donor ascending aorta.

3.0.1.3. During the Transplantation Phase on the Recipient Animal

This third and final phase addresses all the aspects considered previously during the heart explant and vessel preparation.

Placement and Anastomosis of the Donor Heart

The explanted heart is removed from the Custodiol solution, and a circular knot is prepared on the emergent section of the pulmonary artery. At this point, the heart is

positioned upside down on the operating field, so that the severed aorta and pulmonary artery face the common carotid artery and the external jugular vein, respectively. A key aspect of this phase is the focus of the microscope. It must be accepted that it is impossible to have the same focal plane for both the cuffed vessel and the donor vessel. It is necessary to bring the pulmonary artery as close as possible to the jugular vein so that the lumens of both vessels can be visualized, although not perfectly aligned.
At this point, the lumen of the pulmonary artery can be manipulated and pulled down to embrace the cuffed jugular vein. The prepared knot is then slid under the knot holding the jugular vein cuff in place (viewed through the wall of the pulmonary artery that encircles it) and tightened.

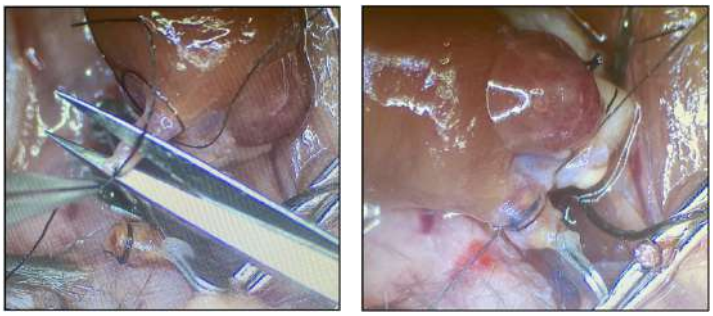

Figure 3-09. Pulmonary artery preparation and section (left). Pulmonary Artery - External Jugular Vein anastomosis (center). Note that the securing knot of the artery on the jugular cuff is placed beneath the knot holding the jugular vein to the cuff: this ensures a sealed anastomosis and guarantees hemostasis.

This pulmonary portion is more challenging due to the difficulty in identifying the lumen and establishing the correct orientation. The pulmonary artery has thinner, more collapsible walls compared to the common carotid artery, making the lumen less visible and harder to access. Proper traction and cuff wrapping may require more time than expected, as the surrounding tissues may adhere tightly or be fragile, requiring extreme precision to avoid damage to the pulmonary artery's wall.
The pulmonary artery is always anastomosed first. Subsequently, the aorta is anastomosed, in a similar manner, on the carotid artery, more medially.

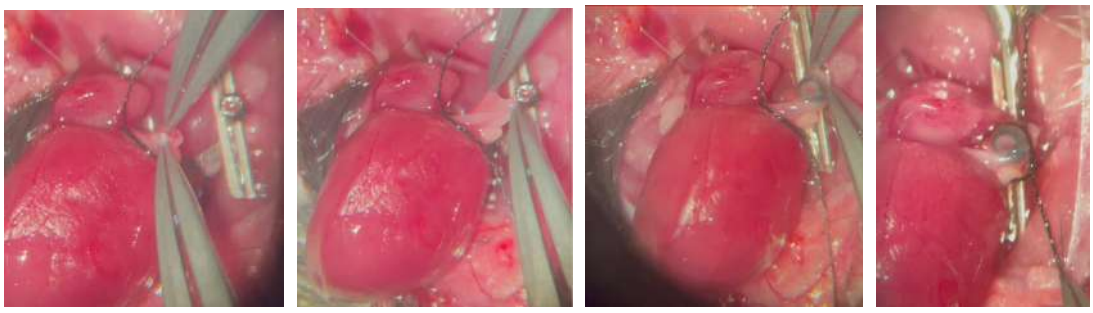

Figure 3-10. From left to right: lumen identification, downward traction, wrapping of the receiving vessel, and aorto-carotid anastomosis.

Great attention must be paid to avoid the two vessels crossing each other. The declamping is performed almost simultaneously and very gently, first removing the jugular clamp to create an outflow path, and then the carotid clamp to provide blood flow to the myocardial tissue and the right cardiac chamber, which can be drained directly through the jugular. The mitral floor does not allow blood to fill the left ventricle.

Essential Elements for Considering the Transplantation Successful

At declamping, it may take only a few seconds for the heart to appear vascularized. However, during this time, there should absolutely be no significant bleeding at the arterial or venous anastomotic sites. If some minor venous bleeding occurs, it can be controlled with gentle tamponade using a cotton swab while waiting for the heart to expand. As the heart begins to enlarge, the auricles start to swell, taking on a red-violet parenchymal appearance. The coronary vessels begin to become identifiable. At this point, the heart usually begins to contract as if it were pumping normally, though it is only being perfused through its myocardium, while the left ventricular chamber remains empty.

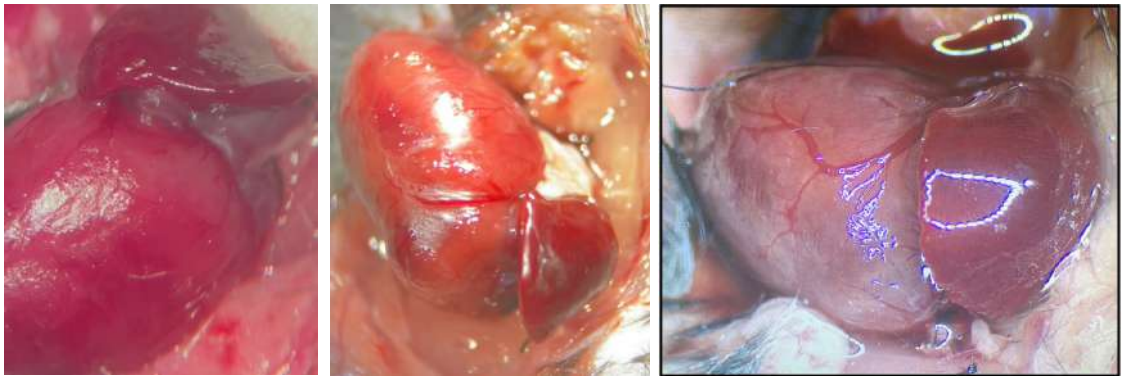

Figure 3-11. Myocardial perfusion upon declamping. Note the increase in volume and the vascularized appearance of the ventricle (coronary vessels) and atria. On the right, the heart cervically transplanted is contracting.

3.0.2. Personally developed improvements in carotid isolation

3.0.2.1. Minimally invasive carotid isolation

The sectioning of the sternocleidomastoid (SCM) muscle inevitably often caused bleeding from small vessels near the cauterized area, which required continuous control during subsequent phases. Furthermore, the muscle trauma induced by the sectioning of the SCM is significant, and despite optimal management through subcutaneous

analgesic injections in the immediate postoperative period and during monitoring, the animal could experience discomfort.
I considered avoiding the sectioning of the SCM by creating space between it and the sternothyroid muscle (located near the midline of the mouse's body) through blunt dissection. The right forceps should be used to medially separate the sternothyroid muscle while simultaneously creating a slit along the medial aspect of the vascular-nervous bundle, creating a breach between its delicate connective trabeculations. The left forceps should be used to carefully traction the belly of the SCM laterally, thereby creating the appropriate surgical window.

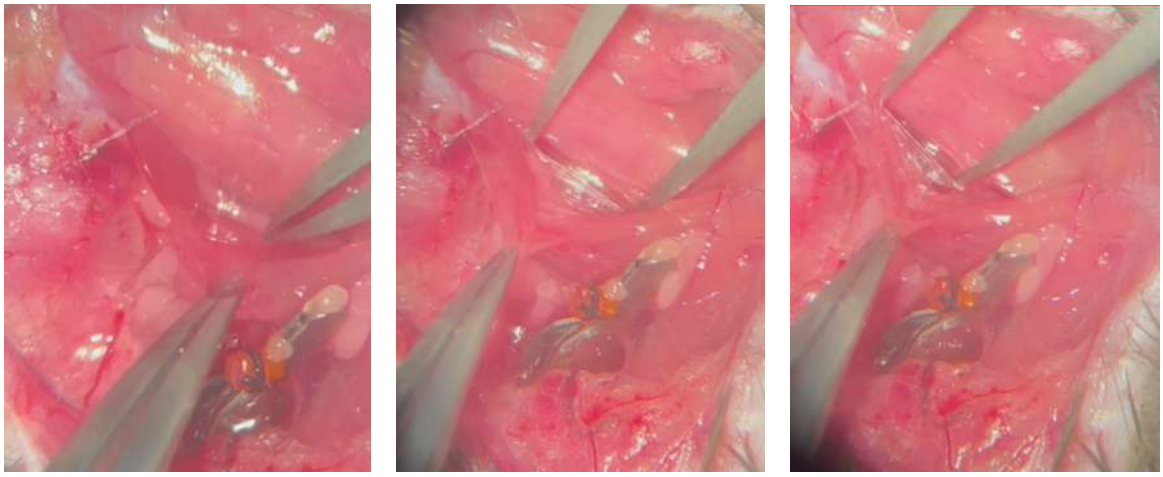

Figure 3-12. Blunt dissection and longitudinal separation of tissue planes between the medial aspect of the SCM (sternocleidomastoid) and the lateral aspect of the sternothyroid muscle.

The next step involves finding a plane to be obtained longitudinally, medial to the carotid artery, using right forceps to separate the structures. In this way, the structures can be gently detached without causing vascular or nerve damage (the vagus nerve runs postero-laterally to the common carotid artery).

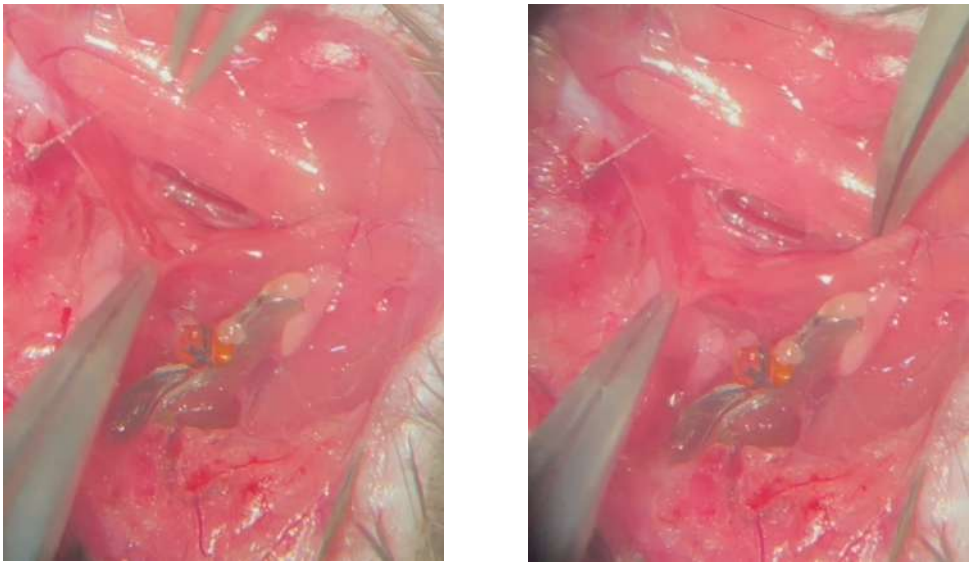

Figure 3-13. Creation of a vascular plane along the medial aspect of the vascular-nervous bundle. In the left image, note a thin, whitish longitudinal structure located laterally to the common carotid artery: the vagus nerve. It must be carefully separated from the artery and excluded from the subsequent ligation (as described earlier) to prevent postoperative digestive issues in the animal.

Once the vascular plane is lightly touched, the tip of the right forceps should be advanced slightly in depth, without losing sight of it, in a medio-lateral direction, while keeping the SCM in tension with the left forceps. At this point, the common carotid artery must be displaced from beneath, and only then, while keeping the tip of the forceps in sight (which should remain closed during this phase), can the tip be directed upwards along the lateral side of the carotid artery, gently spreading the forceps' tips to create space by breaking the thin connective trabeculae that bind it to the vagus nerve and the underlying planes.

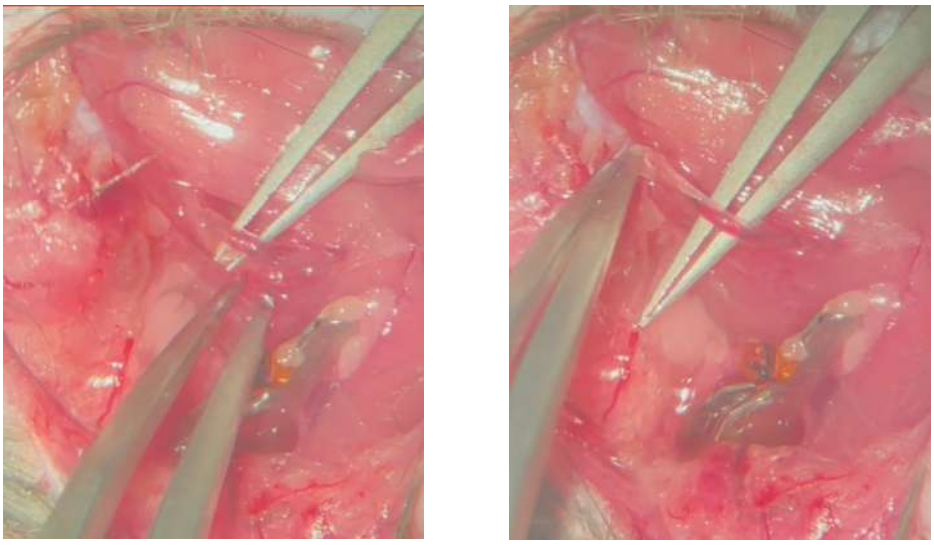

Figure 3-14. Isolation of the common carotid artery after detachment from below. At this stage, sparing the vagus nerve is crucial: it must remain in a postero-lateral plane, adhered to the underlying structures. Note that only at this point can the clamp held by the left hand release the medial side of the SCM.

With careful and successive spreading movements, more space can be created to isolate the artery and pass the first wire. At this point, the medial belly of the SCM can be released from the left forcep, and the procedure proceeds as described above.

3.0.2.2. Endpoints achieved through this Procedural Improvement

The minimally invasive isolation of the carotid artery, as described above, significantly impacts several key aspects of the surgical procedure.

1) First, there is a marked decrease in bleeding, particularly from small vessels near the cauterized area, minimizing the need for constant monitoring and hemostatic intervention. This avoidance of the sternocleidomastoid muscle sectioning not only streamlines the dissection but also reduces tissue trauma.
2) As a result, it notably reduces the overall operative time, with the isolation process taking approximately 5-10 minutes less compared to traditional method.
3) Furthermore, the technique leads to a better postoperative recovery for the animal, with a reduced incidence of pain and muscle-related discomfort. The refined approach enhances the overall success of the procedure by promoting quicker healing and lessened complication rates, contributing to a smoother recovery process.

3.1. Cardiac Unloading in Vivo Enhances Cancer Cell Proliferation

Cardiac metastases, while rare, are also typically smaller compared to extra-cardiac lesions, particularly in the case of hematogenous metastases within the myocardium. This observation is consistent even in patients with highly aggressive cancers that disseminate extensively to other organs. For example, in a case of aggressive uveal melanoma, the tumor exhibited widespread invasion of the liver and lungs but only minimal involvement of the myocardium (figure 3-1).

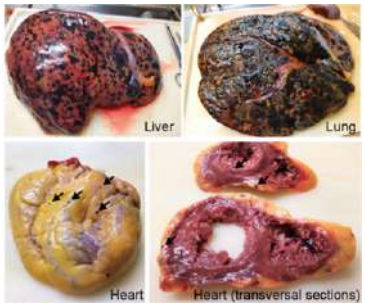

Figure 3-1. Gross appearance of en bloc resection of liver, lung and heart from a patient affected by a highly aggressive metastatic uveal melanoma. Black arrows indicate small metastatic spots mainly in the pericardial fat and minimally within the myocardium.

3.1.1. Mechanical unloading in vivo produces a significant increase in CM proliferation after one month

To investigate the potential role of mechanical load in the low incidence and limited growth of cancer in the heart, we employed an in vivo model of cardiac unloading through heterotopic heart transplantation. In this model, a donor heart is transplanted into the cervical region of a syngeneic recipient mouse, as schematically illustrated in Figure 3-2, the aorta and pulmonary artery of the donor heart are surgically connected to the carotid artery and external jugular vein of the recipient, respectively. This surgical configuration restores perfusion to the transplanted heart while eliminating mechanical load within the left ventricle (LV) [58-62].

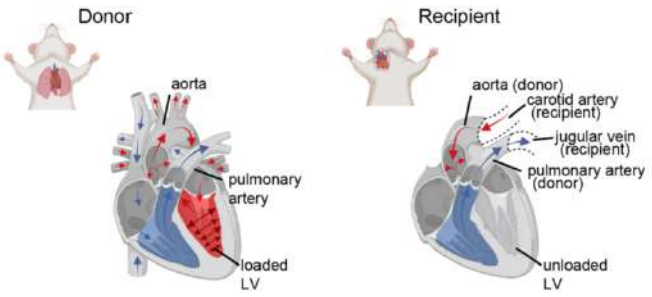

Figure 3-2. Schematic representation of the circulation following heterotopic heart transplantation. The heart is removed from the thorax of a donor mouse (left) and anastomosed to the neck vessels of a recipient mouse (right). In the transplanted heart, the oxygenated blood from the carotid artery bumps into the closed aortic valve and enters the coronary tree. The venous blood is drained back through the pulmonary artery into the jugular vein, in the absence of blood flow into the left ventricle (LV).

Cardiac unloading was confirmed by echocardiographic analysis, which demonstrated a marked reduction in key myocardial strain metrics, including velocity, displacement,

longitudinal strain, and strain rate, in the unloaded hearts compared to native hearts (Figure 3-3).

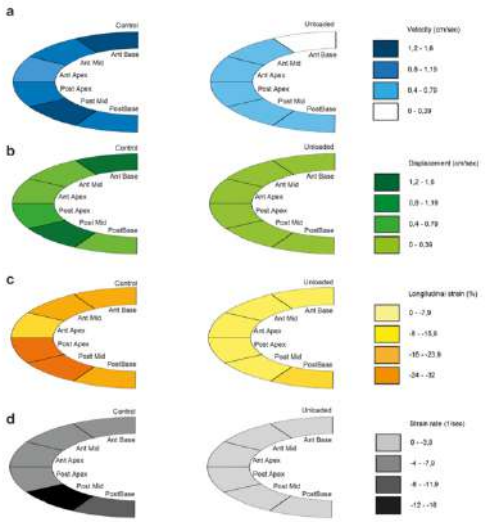

Figure 3-3. Graphical representation of regional velocity (a), displacement (b), longitudinal strain (c) and strain rate (d) of control and unloaded hearts.

These findings validated the efficiency of the unloading model in reducing cyclic mechanical stress within the myocardium. After one month of in vivo unloading, we observed a significant increase in the number of proliferating cardiomyocytes (EdU+ CMs) in the transplanted hearts. This result is consistent with previous evidence showing increased CM regeneration in human hearts mechanically unloaded through left ventricular assist device (LVAD) implantation [3], (Figure 3-4 and 3-5).

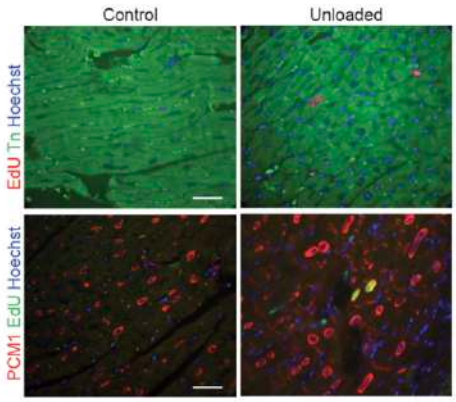

Figure 3-4. Representative immunofluorescence of control and unloaded hearts, in which CMs are stained for either troponin (Tn, upper panels) or the CM-specific nuclear marker pericentriolar material 1 (PCM 1, lower panels) antibodies. Proliferating nuclei are labelled by EdU incorporation. Scale bar: 50 µm.

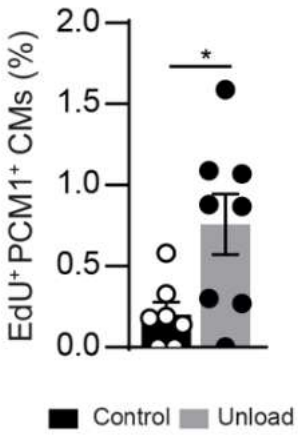

Figure 3-5. Quantification of EdU+PCM1+ proliferating CMs in control and unladed hearts.

To evaluate the impact of mechanical load on tumor cell proliferation, 1 × 10^5 LG1233 lung adenocarcinoma cells, stably expressing Green Fluorescent Protein (GFP), were injected intramyocardially into the LV of both native and unloaded hearts. Lung cancer was selected as the model due to its relatively high propensity to metastasize to the heart, particularly targeting the outer cardiac layers such as the epicardium and pericardium [8].

In native hearts, cancer cells exhibited limited growth, occupying less than 20% of the LV area two weeks after injection, consistent with previous findings. Conversely, in unloaded hearts, cancer cells proliferated extensively, infiltrating the myocardium and leading to an almost complete replacement of healthy cardiac tissue by two weeks post-injection (Figure 3-6 and 3-7).

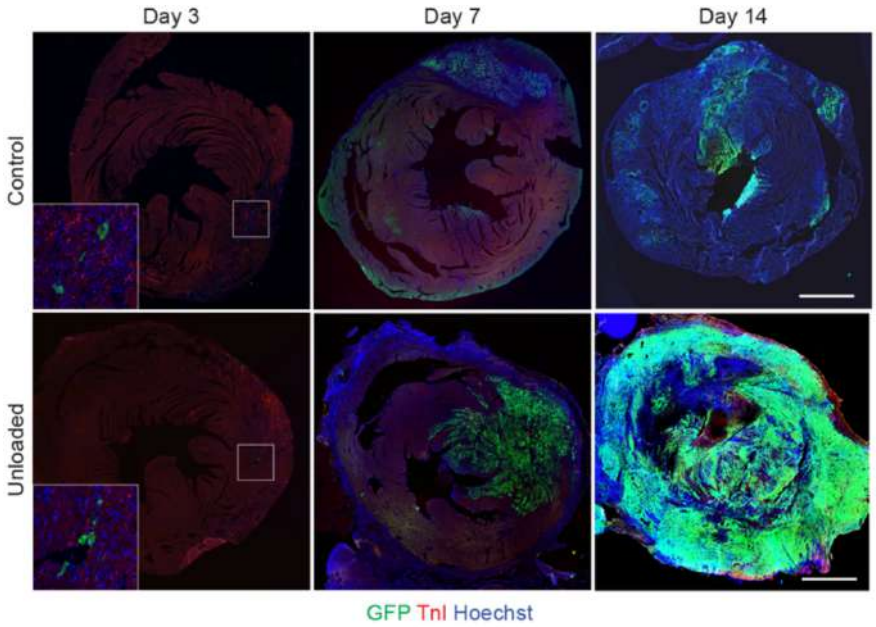

Figure 3-6. Transversal sections of control and unloaded hearts injected with LG1233 GFP+ cancer cells at the indicated time points. CMs are stained for Troponin I (TnI). Insets show high magnification images of engrafted cells at day 3.

.

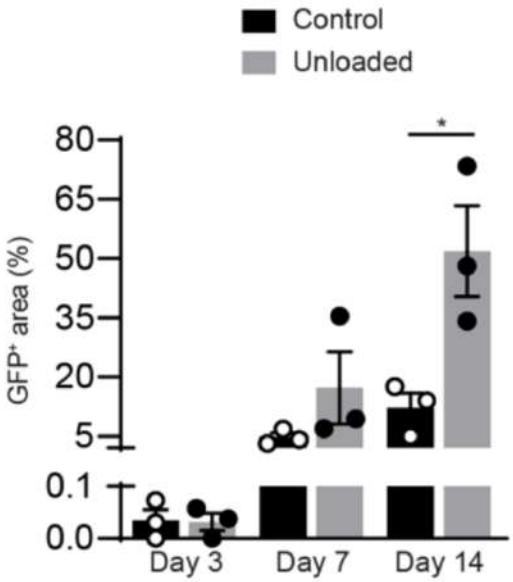

Figure 3-7. Quantification of the area occupied by GFP+ cancer cells in control and unloaded hearts at the indicated time points.

.

The enhanced proliferation of cancer cells in unloaded hearts was not attributable to differences in initial engraftment, as the number of GFP+ cells observed three days post-injection was comparable between the two groups (Figure 3-8, top). Analysis of cell death using TUNEL and cleaved Caspase-3 (cCASP3) staining revealed no GFP+TUNEL+ or GFP+cCASP3+ cells in either native or unloaded hearts at day 3, indicating that tumor size differences observed at day 14 were not due to differential rates of cell death (Figure 3-8, bottom).

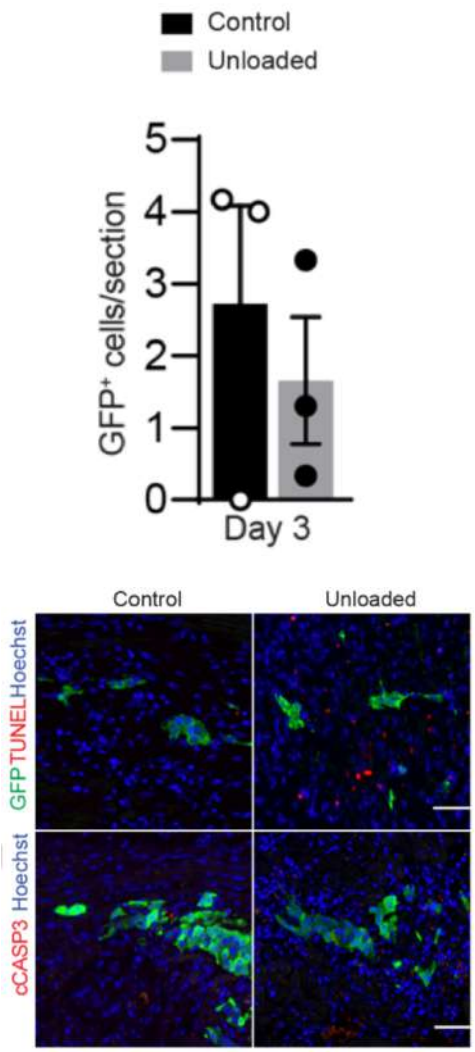

Figure 3-8. Quantification of GFP+ cancer cells in control and unloaded hearts at day 3 [top]. Representative images of control and unloaded hearts stained for TUNEL and GFP. Representative images of control and unloaded hearts stained for cleaved Caspase 3 (cCASP3) and GFP at day 3 [bottom].

3.1.2. Cancer cells grow very poorly in native hearts, but they massively infiltrate the unloaded ones

Cell proliferation was assessed by quantifying the number of cells positive for Ki67 and phosphorylated histone H3 (pHH3), which serve as markers for all active phases of the cell cycle and mitosis/late G2 phase, respectively. Analysis revealed a two-fold increase in the number of proliferating cancer cells in unloaded hearts compared to native hearts at both 7 and 14 days post-injection (Figure 3-9; 3-10; 3-11).

These findings demonstrate that lung cancer cells form larger tumor masses in mechanically unloaded hearts than in native hearts, and this difference can be attributed to an increase in cell proliferation under unloaded conditions.

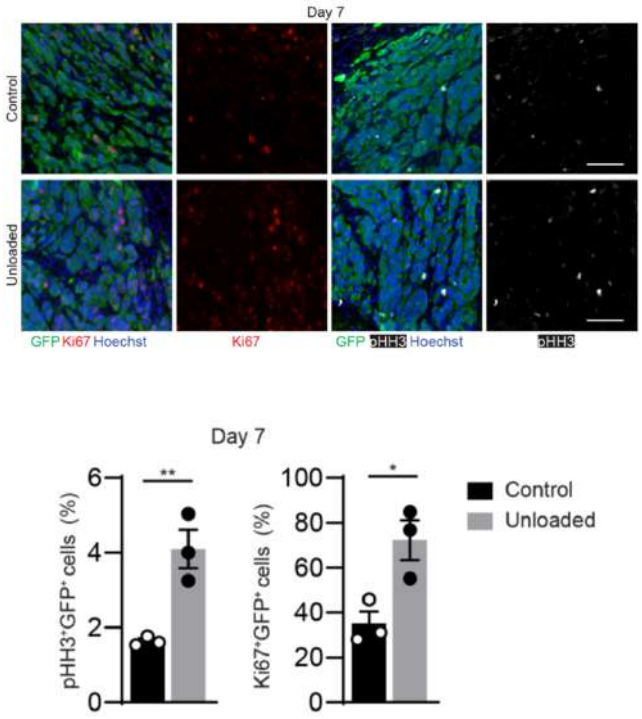

Figure 3-9. Representative images of control and unloaded hearts stained for the proliferation markers phospho-Histone H3 (pHH3) and Ki67, together with GFP, at day 7 (top). Quantification of pHH3+ and Ki67+ cancer cells in control and unloaded hearts at day 7 (bottom).

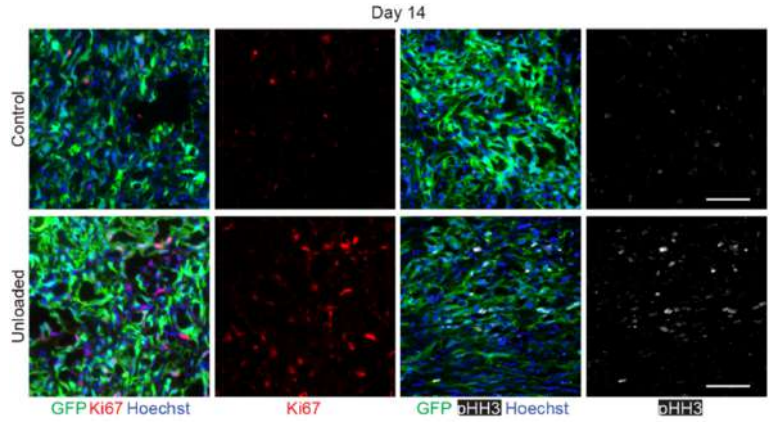

Figure 3-10. Representative images of control and unloaded hearts stained for the proliferation markers phospho-Histone H3 (pHH3) and Ki67, together with GFP, at day 7. Scale bar: 10μm.

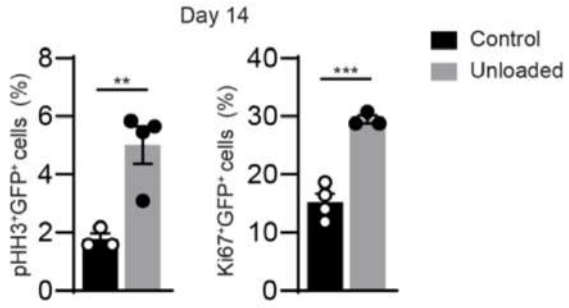

Figure 3-11. Quantification of pHH3+ and Ki67+ cancer cells in control and unloaded hearts at day 14.

3.2. Mechanical Load Modulates Cancer Cell Proliferation in Engineered Heart Tissues

To investigate the role of mechanical load on cancer cell proliferation in a controlled environment, the Engineered Heart Tissue (EHT) system was adapted to include neonatal rat cardiomyocytes (CMs) and fibroblasts. The setup was further modified by incorporating two adjustable metal braces that allowed precise regulation of mechanical load. By rotating these braces, the stiffness of the silicone posts anchoring the tissue could be increased to simulate conditions of elevated mechanical load. Alternatively, the braces could be adjusted to reduce the distance between the tissue's ends, effectively mimicking a mechanically unloaded state (Figure 3-12).

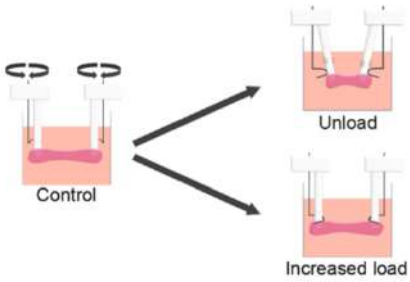

Figure 3-12. Schematic representation of control EHT (left) and its adaptation to induce either unload (top right) or increased load (bottom right).

To assess the suitability of EHTs for studying the effects of mechanical load variations on cell proliferation, experiments were first conducted on CMs.

3.2.1. Mechanical load affects CM proliferation and maturation in EHTs

Mechanical unloading led to an increase in CM proliferation at 3 days, as shown by EdU incorporation and the expression of proliferation markers Ki67 and phospho-histone H3 (pHH3) (Figure 3-13; 3-14; 3-15). These findings are consistent with the results observed in heterotopically transplanted hearts in vivo.

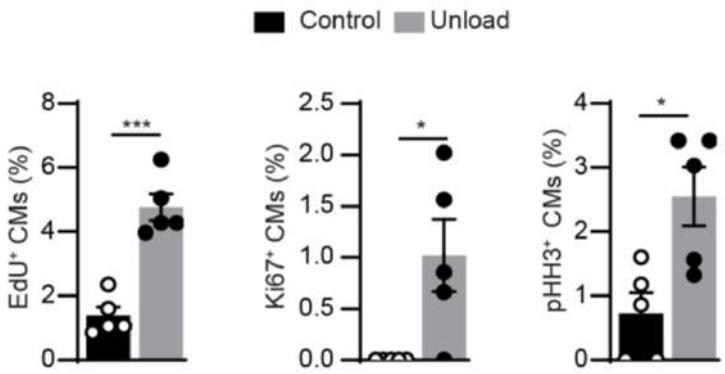

Figure 3-13. Quantification of CM proliferation in control and unloaded EHTs, assessed by EdU incorporation and staining for both Ki67 and phospho-histone H3

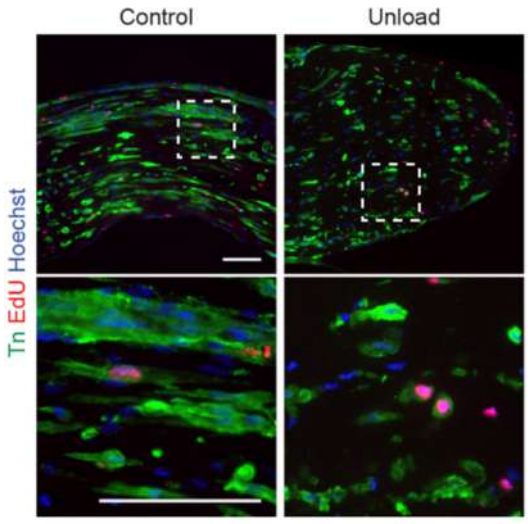

Figure 3-14. Representative immunofluorescence of control and unloaded EHTs in which CMs are stained for troponin (Tn) and proliferating nuclei are labelled by EdU. Lower panels are high magnification images of the dashed square drawn on upper panels.

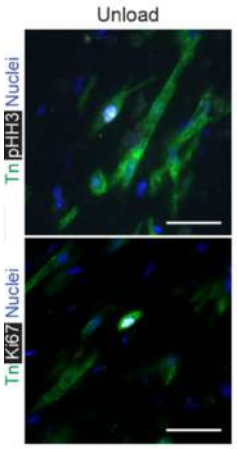

Figure 3-15. Representative immunofluorescence of an unloaded EHT in which CMs are stained for troponin (Tn) and proliferating nuclei for phospho-histone H3. d. Representative immunofluorescence of an unloaded EHT in which CMs are stained for troponin (Tn) and proliferating nuclei for phospho-histone H3. Representative immunofluorescence of an unloaded EHT in which CMs are stained for troponin (Tn) and proliferating nuclei for Ki67.

In contrast, prolonged mechanical loading for 2 weeks resulted in reduced CM proliferation, as indicated by Ki67 and pHH3 staining (Figure 3-16, top). EdU incorporation was slightly increased under conditions of elevated mechanical load (3-16, bottom left). However, the EdU+ nuclei primarily corresponded to bi-nucleated CMs (3-16, bottom right), which aligns with enhanced CM maturation.

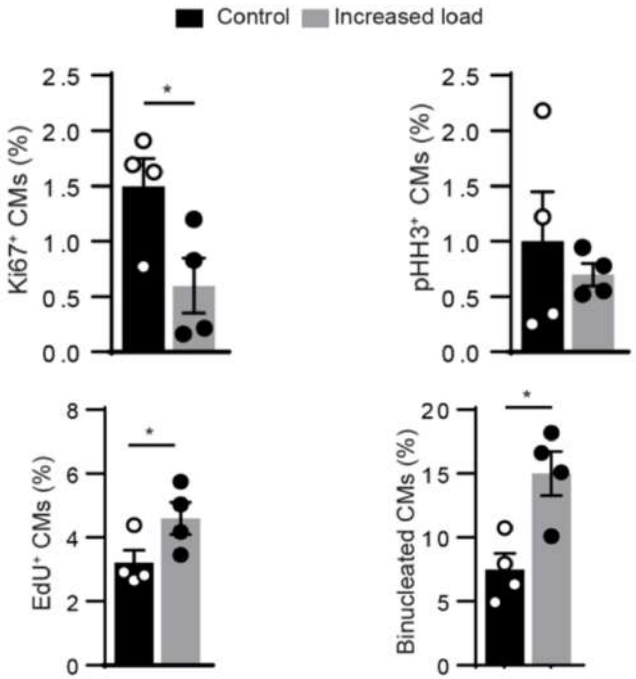

Figure 3-16. Quantification of CM proliferation in EHTs in conditions of control and increased overload, assessed by staining for Ki67 (top left) and phospho-histone H3 (top right). Quantification of EdU incorporation in EHTs in conditions

of control and increased overload (bottom left). Quantification of CM binucleation in EHTs in conditions of control and increased overload (bottom right).

This was further supported by a significant increase in CM cross-sectional area and contractile force under conditions of increased load (Figure 3-17).

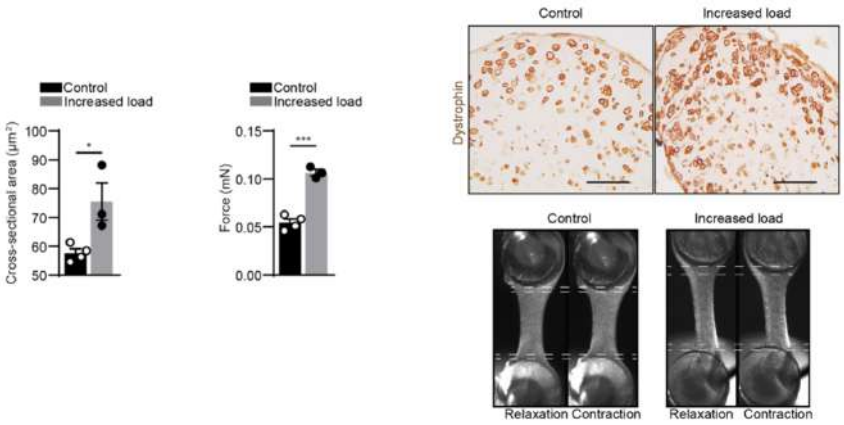

Figure 3-17. Quantification of CM cross-sectional area in EHTs in conditions of control and increased overload (left). Quantification of force generated by EHTs in conditions of control and increased overload (right). Representative immunohistochemistry of EHTs in conditions of control and increased overload, stained for dystrophin (right top). Representative images of EHTs in conditions of control and increased overload (right bottom) [white dashed lines indicate the displacement of silicon posts from relaxation to contraction].

These results indicate that mechanical unloading promotes CM proliferation, while increased mechanical load reduces proliferation and favors CM maturation.

3.2.2. Mechanical load regulates cancer cell proliferation in EHTs, which mimic the nature and magnitude of mechanical forces present in a functioning, beating heart

Engineered Heart Tissues (EHTs) were constructed incorporating GFP+ lung cancer cells (Figure 3-18).

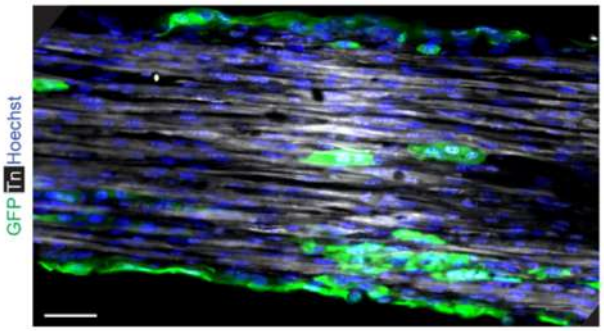

Figure 3-18. Representative immunofluorescence image of an EHT composed of both Troponin (Tn)+ CMs and GFP+ cancer cells.

After 7 days, a period sufficient for cardiomyocyte maturation and the establishment of synchronized contractions, the metal braces were adjusted to either reduce or increase the mechanical load for an additional 3-day period. Unloading conditions resulted in an increase in cancer cell proliferation within the EHTs, whereas increased loading conditions led to a reduction in their proliferation (Figure 3-19).

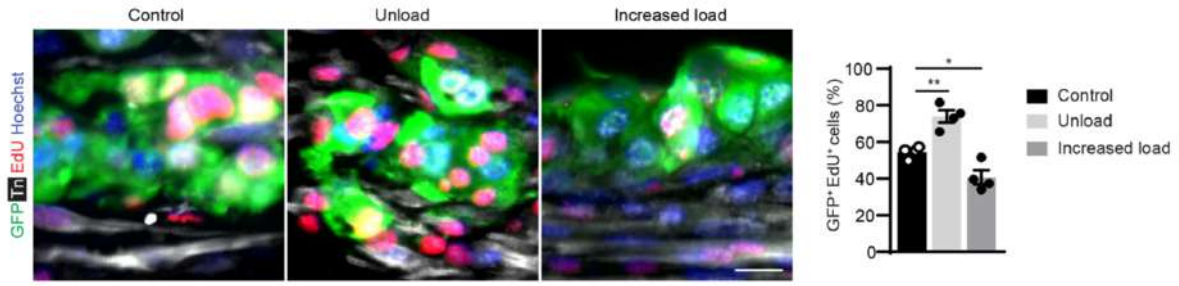

Figure 3-19. Immunofluorescence images of EHTs exposed to control load, unload and increased load, stained for GFP, Troponin (Tn) and EdU (left). Quantification of the percentage of proliferating EdU+ cancer cells in EHTs exposed to control load, unload and increased load (right).

These findings align with the results observed in vivo, where heterotopic heart transplantation (HHT) influenced cancer cell proliferation under unloaded conditions.

3.2.3. Validated quality of the EHT model

To assess whether the EHT system accurately replicates the primary mechanical forces present in a beating heart, mathematical simulations of cardiac mechanics were performed. Figure 3-20 illustrates an idealized rodent LV, where myofiber orientation transitions transmurally from the endocardium (+60°, shown in red) to the epicardium (-60°, shown in blue).

Figure 3-20. Simulated LV geometry and imposed fiber fields.

This LV model was simulated contracting under either a standard systolic cavity pressure or, in the unloaded condition, with no cavity pressure (Figure 3-21).

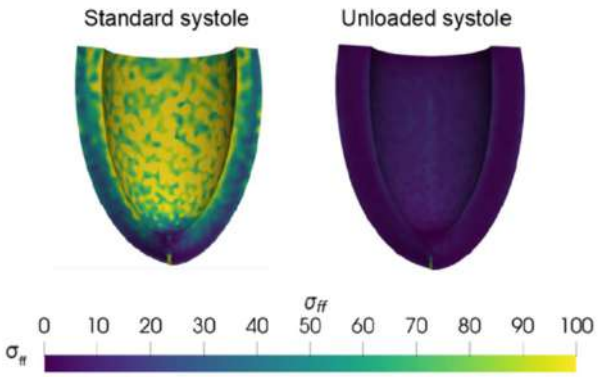

Figure 3-21. Graphical representation of end systolic fiber direction Cauchy stresses on the endocardial surface for a standard systolic load (15 kPa) and in the absence of load.

The removal of pressure significantly reduced calculated stress magnitudes across all three principal directions: the myofiber direction (σff), the sheet-aligned direction (σss), and the normal direction (σnn) (Figure 3-22). These results align with the strain parameters obtained experimentally, as shown in Figure 3-3.

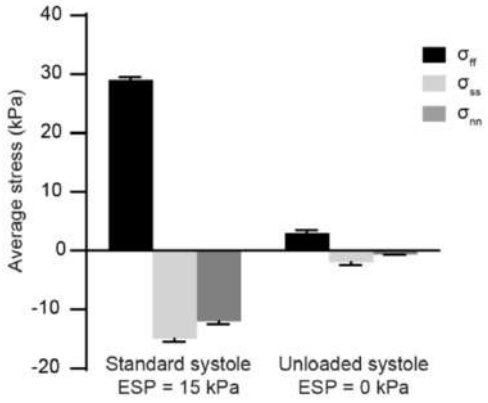

Figure 3-22. Calculated average peak stress in the fiber (σff), cross fiber (σss) and cross sheet direction (σnn) in the myocardium for standard and unloaded simulations.

A model was then developed to represent the EHT, assuming a cylindrical geometry. The contraction of the EHT was simulated against a spring constant that closely approximates the experimentally measured contraction at peak systole (~15%), as depicted in Figure 3-23. Mechanical stresses were computed for the three configurations described in Figure 3-12: standard contraction (control), unloaded, and increased load conditions. As shown in Figure 3-23, the EHT exhibited stress patterns consistent with those observed in the LV simulation, particularly for fiber-aligned stresses (σff) and

orthogonal normal stresses, both circumferential (σc) and radial (σr). Increasing the mechanical load resulted in a marked rise in the magnitude of all stress components, whereas stresses were largely absent under unloaded conditions.
These findings demonstrate that mechanical load modulation in EHTs effectively mirrors the effects observed during cardiac unloading in vivo. Additionally, the modulation of mechanical forces in both systems results in comparable outcomes on the proliferation of both cardiac and cancer cells.

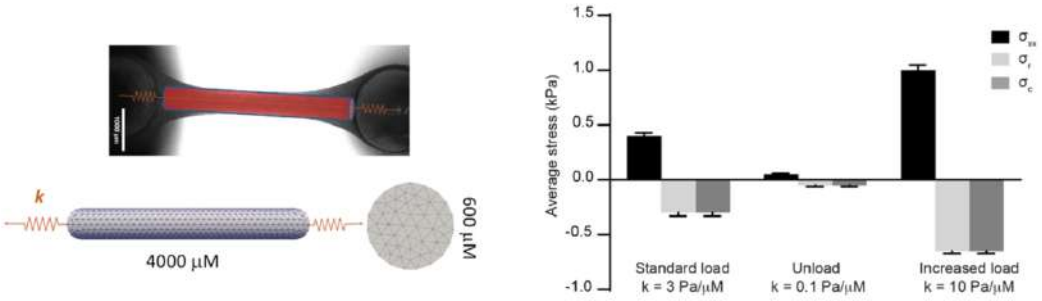

*Figure 3-23. EHT cylindrical geometry and imposed Robin boundary conditions for finite element method (FEM) simulation (left). Calculated average EHT stress in standard conditions, and in unloaded and increased load conditions, via altering Robin boundary stiffness (right). Scale bar:100μm in **b**;20μm in **c**.*

3.3. Cancer cells preferentially grow in EHT regions exposed to low mechanical pressure

3.3.1. Calcium addition to obtain beating EHT systems

3.3.1.1. GFP+ cancer cells grew significantly more and occupied a larger area in static than beating EHTs

The unloading system for EHTs described in Figure 3-12 is not suitable for long-term experiments, as tissues subjected to unloading undergo extensive remodeling and lose their original 3D structure over time. To investigate the effects of prolonged cardiac unloading on cancer cell growth, an alternative model was used in which cardiomyocyte contractility was controlled by the presence or absence of calcium in the culture medium. GFP+ lung cancer cells were incorporated into EHTs cultured in either calcium-free medium (static EHTs) or calcium-containing medium (beating EHTs), as illustrated in Figure 3-24. Consistent with prior observations, GFP+ cancer cells exhibited significantly greater growth and occupied a larger area in static EHTs compared to beating EHTs, as demonstrated and quantified in Figure 3-24 and 3-25 for whole tissues and in Figure 3-26 and 3-27, for cross-sectional analysis.

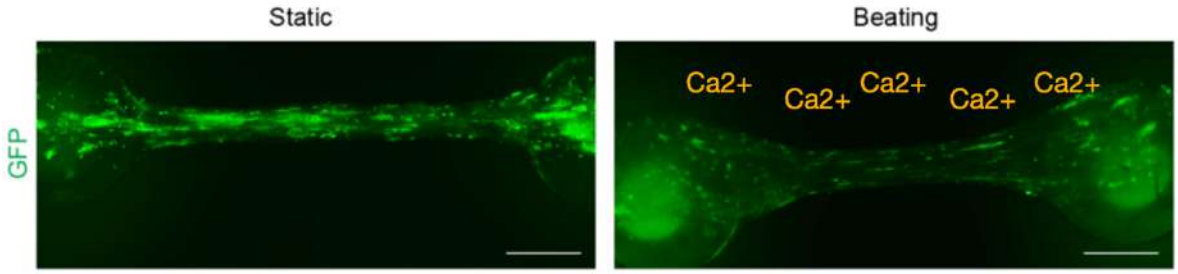

Figure 3-24. Representative low magnification images of EHTs composed by both CMs and LG1233 GFP+ cancer cells, cultured in the absence (static) or presence (beating) of calcium.

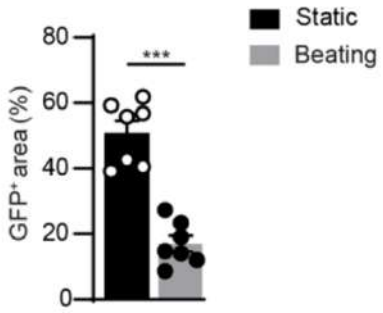

Figure 3-25. Quantification of the area occupied by LG1233 GFP+ cancer cells in static and beating EHTs.

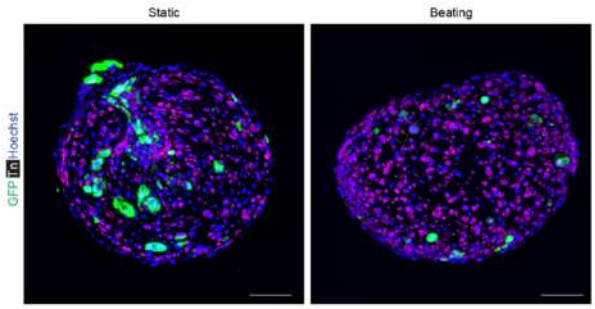

Figure 3-26. Representative cross-sections of static and beating EHTs stained for Troponin (Tn) and GFP.

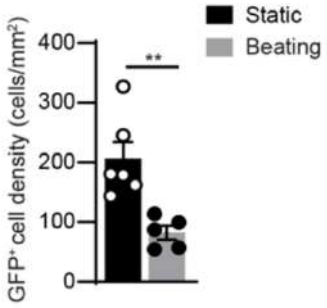

Figure 3-27. Quantification of LG1233 GFP+ cancer cell density in static and beating EHTs.

This difference was accompanied by a notable reduction in cancer cell proliferation in beating EHTs (Figure 3-28 and 3-29).

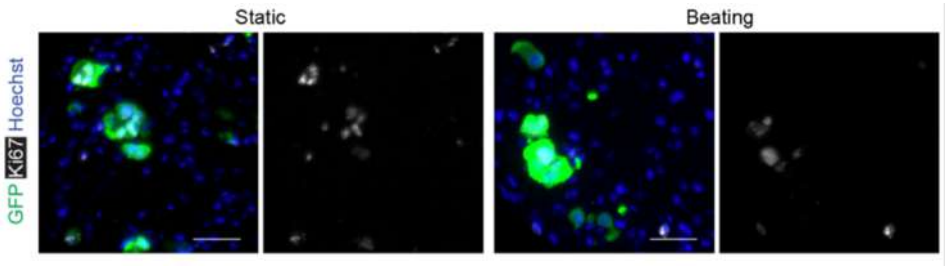

Figure 3-28. Representative immunofluorescence staining of static and beating EHTs stained for Ki67 and GFP.

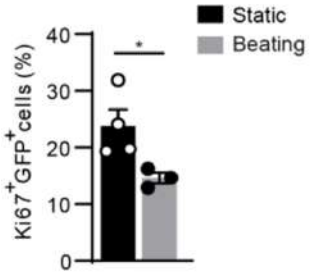

Figure 3-29. Quantification of Ki67+ proliferating LG1233 GFP+ cancer cells in static and beating EHTs.

Figure 3-30 confirms that the absence of calcium did not affect the proliferation of LG cells cultured in standard 2D conditions.

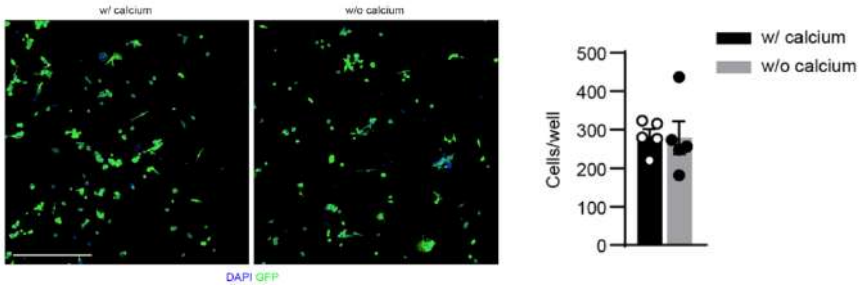

Figure 3-30. Quantification of the number of LG1233 cells after 5 days of culture in EHT medium with or without calcium supplementation (left). Representative images of LG1233 cells cultured in EHT medium with or without calcium supplementation (right). Scale bar: 100 µm.

3.3.1.2. In beating EHTs, cancer cell density forms a gradient that is inversely related to the gradient of hydrostatic pressure

Cancer cells were found to preferentially localize in the outer layers of beating EHTs, avoiding the central regions, while in static EHTs, they were evenly distributed throughout the tissue (Figure 3-26). Using the simulated EHT model presented in Figure 3-31 (right), the beating EHT was analyzed along the radial direction over a full simulated twitch. This analysis considered the higher density of myocytes in the outer layers of the EHT, as observed microscopically. The simulation results, shown in Figure 3-31 (left), indicated elevated hydrostatic pressure in the internal regions of the EHT at peak systole. Quantification of cancer cell distribution across multiple concentric layers within each EHT confirmed an even distribution in static EHTs. In contrast, in beating EHTs, cancer cell density displayed a gradient that inversely correlated with the gradient of hydrostatic pressure (Figure 3-32), suggesting that increased compressive forces in the central regions of the tissue inhibit cancer cell proliferation.

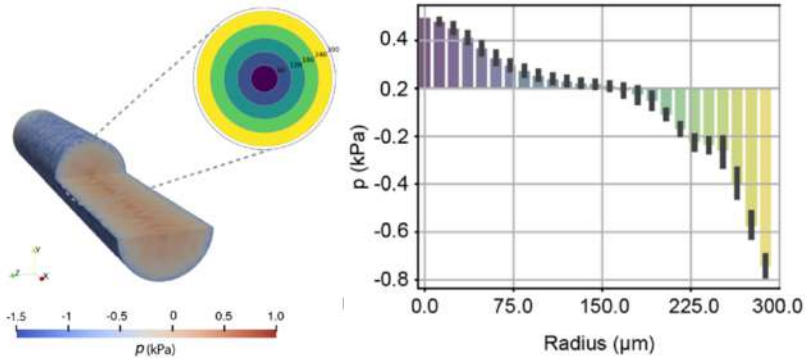

Figure 3-31. Graphical depiction of calculated hydrostatic pressure throughout the simulated EHT at peak systole with inset showing the cross section divided into 5 radial layers for reference (left). Quantification of simulated hydrostatic pressure as a function of radial distance from the centerline of the modelled EHT (right).

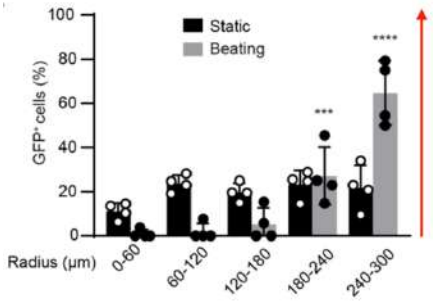

Figure 3-32. Distribution of GFP+ cancer cells in the radial layers depicted in g. Scale bar: 1mm in a,100μm in c, 50μm in e

.

These findings indicate that both mechanical load and the compressive forces generated by cardiomyocyte contraction play a significant role in reducing cancer cell proliferation within EHTs.

3.4. Transcriptome analysis on human cardiac cancer cells

3.4.1. The most highly overexpressed genes in cardiac metastases belong to the "Histone demethylation" enzymatic pathway

To investigate the molecular mechanisms through which cancer cells detect mechanical stimuli in the beating heart and translate them into reduced cell proliferation, we analyzed the transcriptional profile of cancer cells that naturally grow in the myocardium, specifically within human cardiac metastases. Samples were obtained from patients with three distinct primary tumors (lung adenocarcinoma, colon carcinoma, and cutaneous melanoma) that had metastasized to both the heart and other organs, as illustrated in Figure 3-33. Using spatial transcriptomics with GeoMX technology, cancer cells were identified based on specific markers: anti-pan-cytokeratin antibodies for lung and colon carcinoma cells, and anti-PMEL antibodies for melanoma cells (Figure 3-34). The transcriptional profiles of cancer cells in cardiac metastases were compared with those from extra-cardiac sites, including primary tumors and non-cardiac metastases.

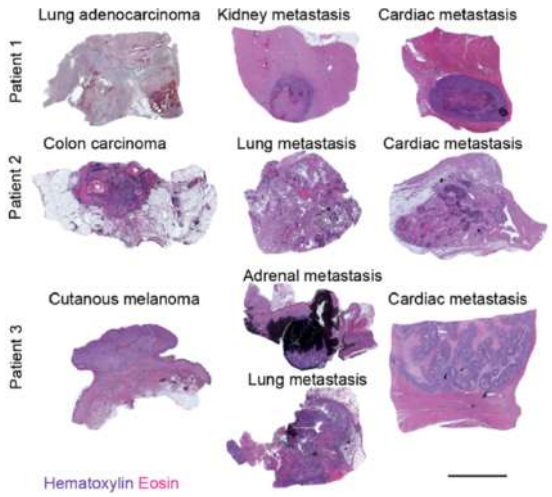

Figure 3-33. Hematoxylin/eosin staining of primary cancers that disseminated to both the heart and extra- cardiac sites.

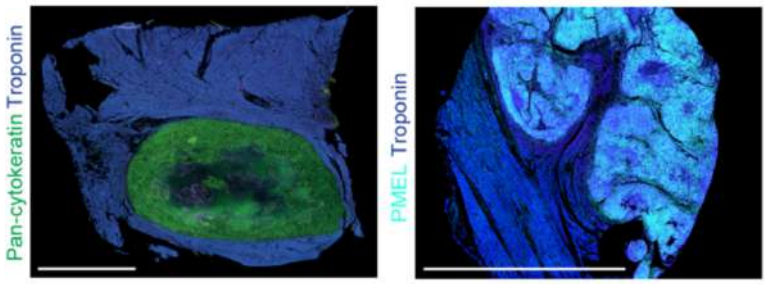

Figure 3-34. Representative immunofluorescent staining of cardiac metastases, in which carcinoma cells are stained for pan-cytokeratin, melanoma cells for PMEL and CMs for Troponin.

Unsupervised hierarchical clustering, based on the most differentially expressed genes (DEGs, n = 1753, ANOVA P < 0.01), revealed a shared transcriptional profile among cardiac metastases, irrespective of the tumor's origin (Figure 3-35, left). Gene ontology analysis identified "Histone Demethylation" as the most enriched pathway in cardiac metastases, characterized by the highest number of DEGs and the most significant upregulation of associated genes (Figure 3-35, right).

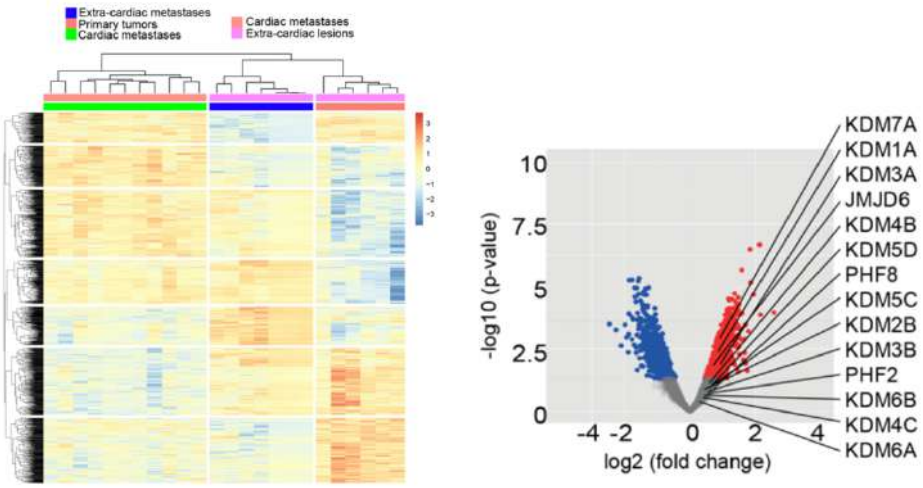

Figure 3-35. Heatmap showing unsupervised clustering based on most differentially expressed genes. Gene expression level was expressed as normalized value after row standardization and displayed as gradient colors from higher (dark red) to lower (dark blue) – [left]. Volcano plot of differential gene expression analysis, comparing cardiac metastases and extra-cardiac metastases, with indication of the most upregulated genes belonging to the Histone Demethlyation pathway in cardiac metastases. The log2(fold-change) and the -log10(p-value) are represented in x-axis and y-axis, respectively. Red and blue dots denote genes significantly overexpressed or silenced in cardiac metastases, respectively (p < 0.05), while grey dots represent genes without difference in expression between the two groups [right].

3.4.2. The levels of H3K9 tri-methylation were lower in the nuclei of cardiac metastases compared to those detected in extra-cardiac metastases

In line with the observed upregulation of multiple histone demethylases, the levels of H3K9 tri-methylation were found to be reduced in the nuclei of cancer cells within cardiac metastases when compared to those in primary tumors and extra-cardiac metastases (Figure 3-36 and 3-37).

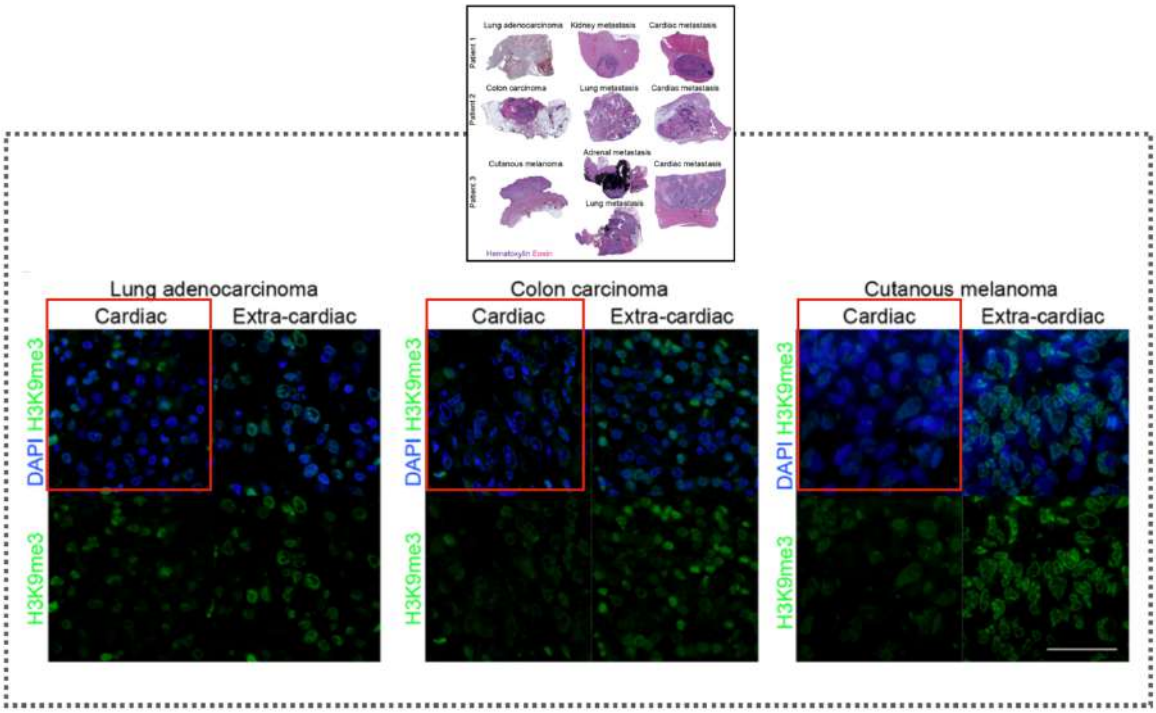

Figure 3-36. Representative images of H3K9me3 in the nucleus of cardiac and extra-cardiac lesions from the samples analyzed by spatial transcriptomics.

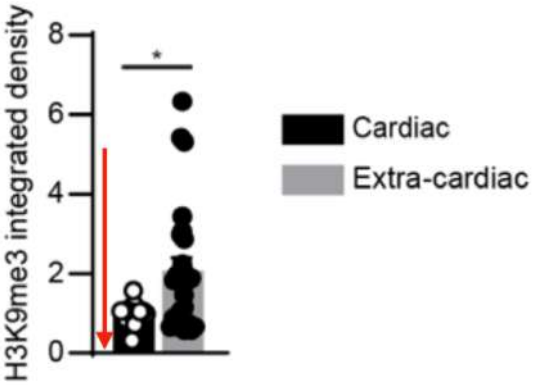

Figure 3-37. Quantification of the levels of H3K9me3 in the nucleus of cardiac and extra-cardiac lesions from the samples analyzed by spatial transcriptomics.

3.4.3. The chromatin state results less compact in cardiac metastases than in extra-cardiac lesions

The observed reduction in H3K9 tri-methylation levels was accompanied by changes in chromatin organization, with chromatin appearing less compact in cardiac metastases compared to extra-cardiac lesions. As illustrated in Figure 3-38 and 3-39, the coefficient of variation (CV) of DNA compaction, a standard metric for evaluating chromatin condensation [63-65], was significantly lower in cardiac metastases than in extra-cardiac lesions.

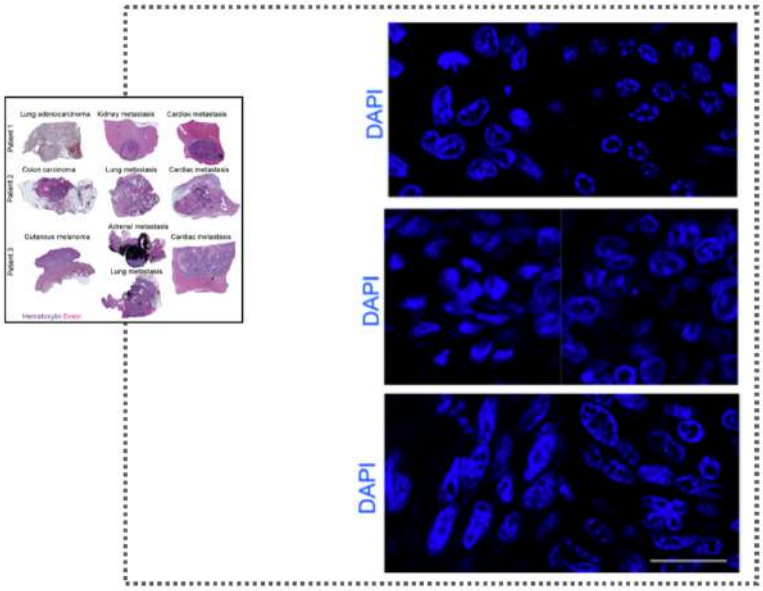

Figure 3-38. Representative images of chromatin compaction in the nucleus of cardiac and extra-cardiac lesions from the samples analyzed by spatial transcriptomics. Scale bar: 20µm.

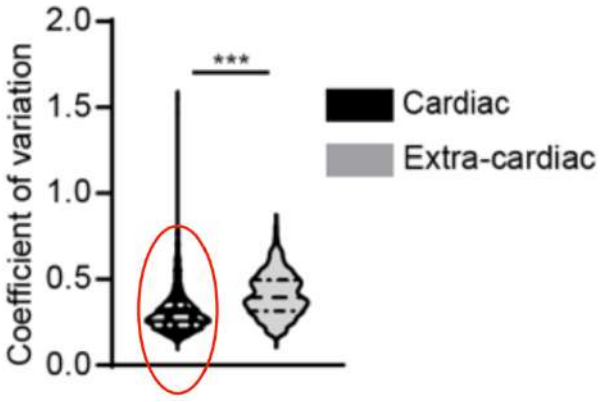

Figure 3-39. Coefficient of variation calculated based on the DAPI fluorescent images represented (top).

These findings indicate that cancer cells located in the human heart exhibit increased expression of histone demethylases, leading to decreased H3K9 tri-methylation levels and reduced chromatin compaction.

3.5. The effect of mechanical load on chromatin

To confirm the impact of mechanical load on histone methylation and chromatin structure, we examined these parameters within our experimental models of cardiac unloading.

3.5.1. Assessing the H3K9me Level and Chromatin Compaction in our Experimental Models In Vivo

3.5.1.1. H3K9me Level

Initially, we analyzed histone methylation in both native and unloaded hearts, observing that cardiac unloading led to a notable increase in H3K9 tri-methylation levels (Figure 3-40).

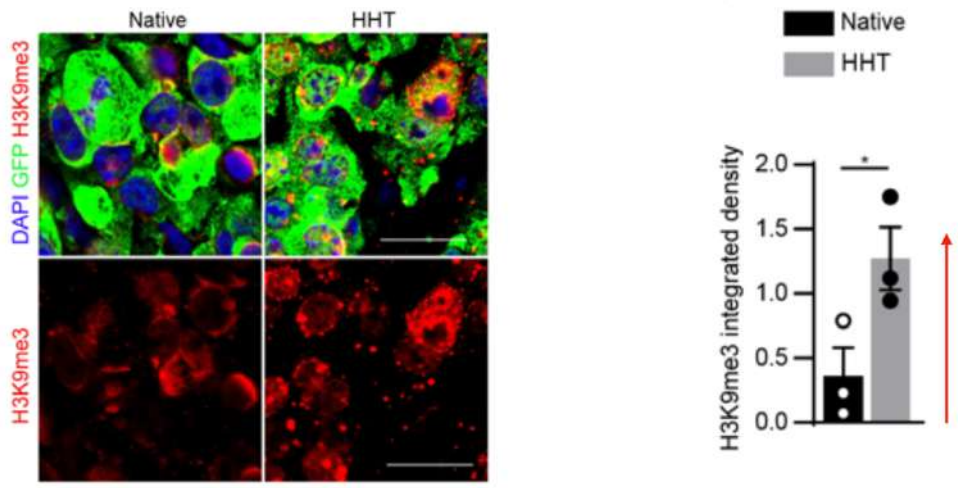

Figure 3-40. Representative images (left) and quantification (right) of H3K9me3 in the nucleus of LG1233 GFP+ cancer cells in native hearts and in hearts unloaded by heterotopic transplantation.

3.5.1.2. Chromatin Compaction

This increase was accompanied by enhanced chromatin compaction (Figure 3-41).

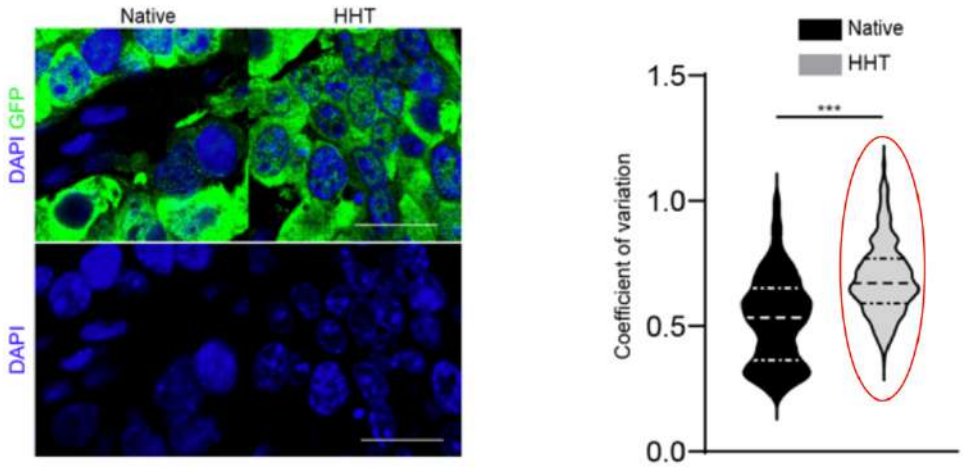

Figure 3-41. Representative images (left) and quantification (right) of chromatin compaction by DAPI staining of LG1233 GFP+ cancer cells in native hearts and in hearts unloaded by heterotopic transplantation.

3.5.2. Assessing the H3K9me Level and Chromatin Compaction in our Experimental Models Ex Vivo

3.5.2.1. H3K9me Level

Subsequently, we examined beating and static EHTs, finding elevated levels of H3K9 tri-methylation under static conditions compared to beating EHTs (Figure 3-42).

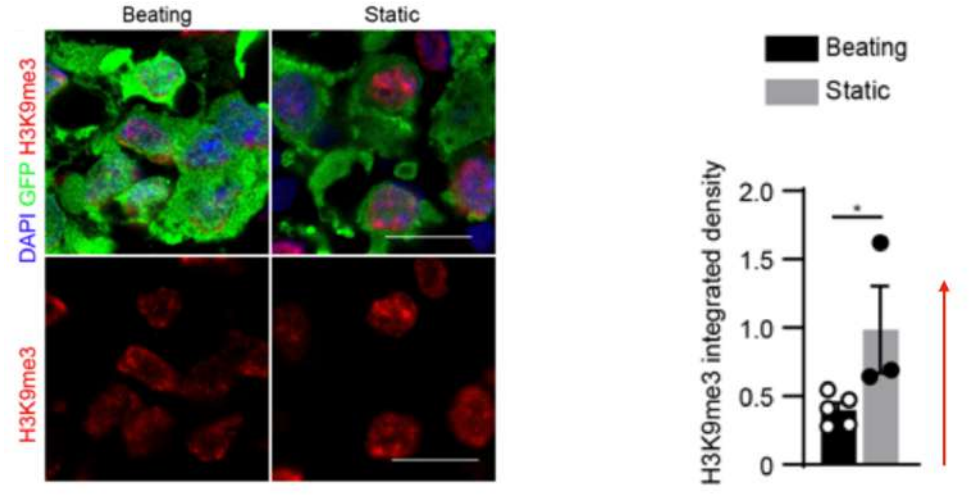

Figure 3-42. Representative images (left) and quantification (right) of H3K9me3 in the nucleus of LG1233 GFP+ cancer cells in static and beating EHTs.

3.5.2.2. Chromatin Compaction

We also observed a significant chromatin compaction under static conditions (Figure 3-43).

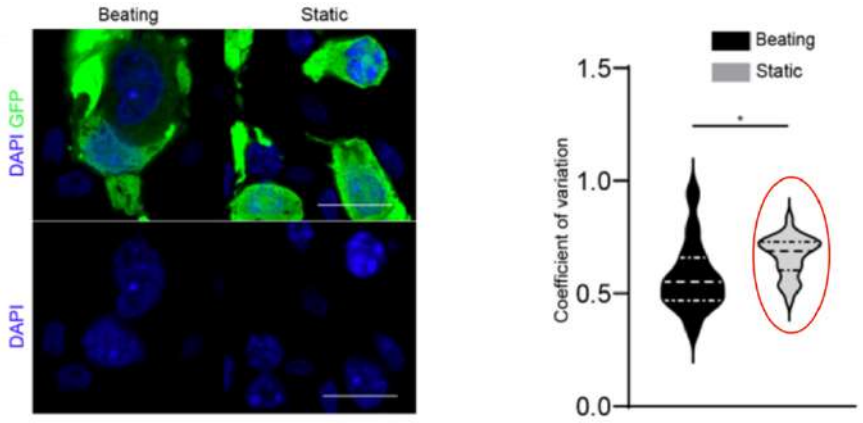

Figure 3-43. Representative images (lesft) and quantification (right) of chromatin compaction by DAPI staining of LG1233 GFP+ cancer cells in static and beating EHTs.

To determine whether H3K9 tri-methylation is not only associated with but also causally linked to cancer cell proliferation, we silenced the main lysine-specific demethylases (KDMs) that target H3K9 and were found to be upregulated in human cardiac metastases. The silencing of KDM4C, KDM4D, or both in combination, in LG1233 cells prior to their incorporation into EHTs, led to an increase in the area occupied by GFP+ cancer cells and an elevated density of LG1233 cells within beating EHTs (Figure 3-44).

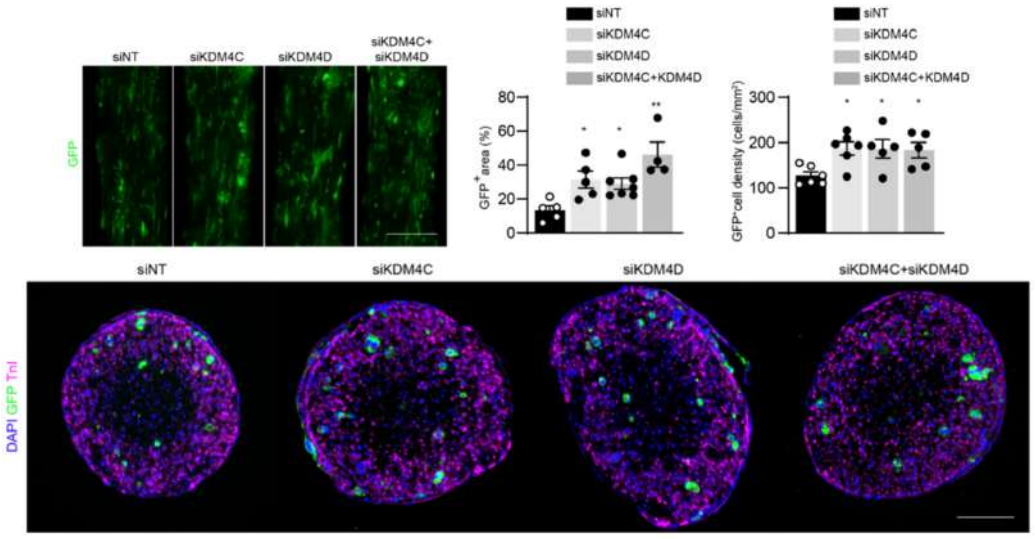

Figure 3-44. Representative low magnification images of EHTs containing LG1233 GFP+ cancer cells treated with the indicated siRNAs (top, left). Quantification of the area occupied by LG1233 GFP+ cancer cells upon treatment with the indicated siRNAs (top, center). Quantification of the density of LG1233 GFP+ cancer cells in EHT cross-sections, upon treatment with the indicated siRNAs (top, right). Representative cross-sections of EHTs containing LG1233 GFP+ cancer cells treated with the indicated siRNAs (bottom). Scalebar: 300µm (top, left),100 µm (bottom).

3.6. Does the LINC complex play a role?

Mechanical forces can influence chromatin condensation through specific mechanotransduction pathways. One such key mechanotransducer is the Linker of Nucleoskeleton and Cytoskeleton (LINC) complex, which consists of four Nesprin proteins and two Sun proteins [66]. To determine whether components of the LINC complex are necessary for cancer cells to detect mechanical load and mediate its effects on cell proliferation, we silenced each LINC complex member individually using specific siRNAs in LG1233 cells and evaluated their proliferation within beating EHTs.

3.6.1. Silencing LINC Members with Specific siRNA

3.6.1.1. Silencing of both Nesprin-2 and Nesprin-4 significantly increased the area occupied by LG1233 cells

As illustrated in Figure 3-45, the silencing of Nesprin-2 and Nesprin-4 led to a notable increase in the area occupied by LG1233 cells.

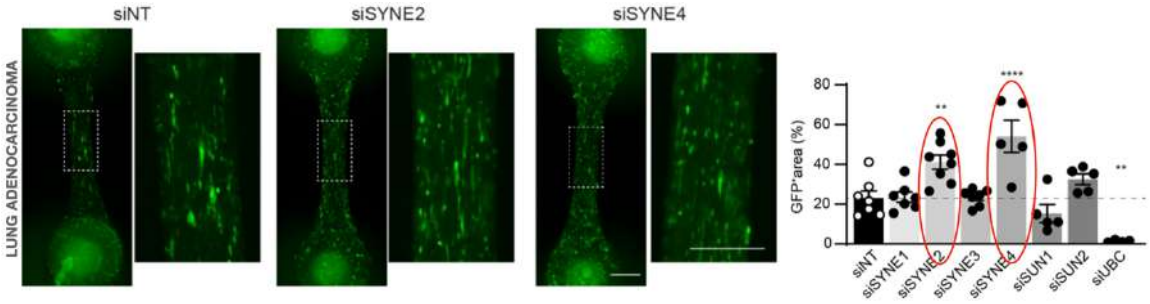

Figure 3-45. Representative low magnification images of EHTs containing LG1233 GFP+ cancer cells treated with the indicated siRNAs. A higher magnification of the squared region is shown on the right for each EHT (left). Quantification of the area occupied by LG1233 GFP+ cancer cells upon treatment with the indicated siRNAs (right). Scale bar: 300 µm.

3.6.1.2. Silencing of both Nesprin-2 and Nesprin-4 significantly increased the LG1233 cell density in EHT cross-section

Silencing of both Nesprin-2 and Nesprin-4 led to a significant increase in LG1233 cell density within EHT cross-sections (Figure 3-46).

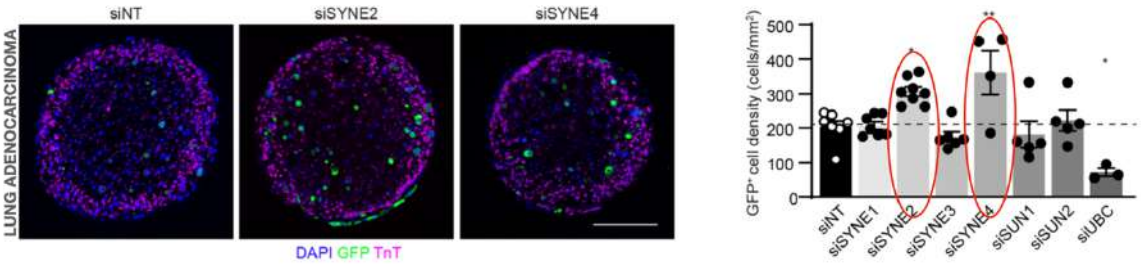

Figure 3-46. Representative cross-sections of EHTs containing LG1233 GFP+ cancer cells treated with the indicated siRNAs (left). Quantification of the density of LG1233 GFP+ cancer cells in EHT cross-sections, upon treatment with the indicated siRNAs (right). Scale bar: 100 µm.

However, none of the LINC complex components influenced cell proliferation when assessed in two-dimensional pure cell cultures (Figure 3-47)

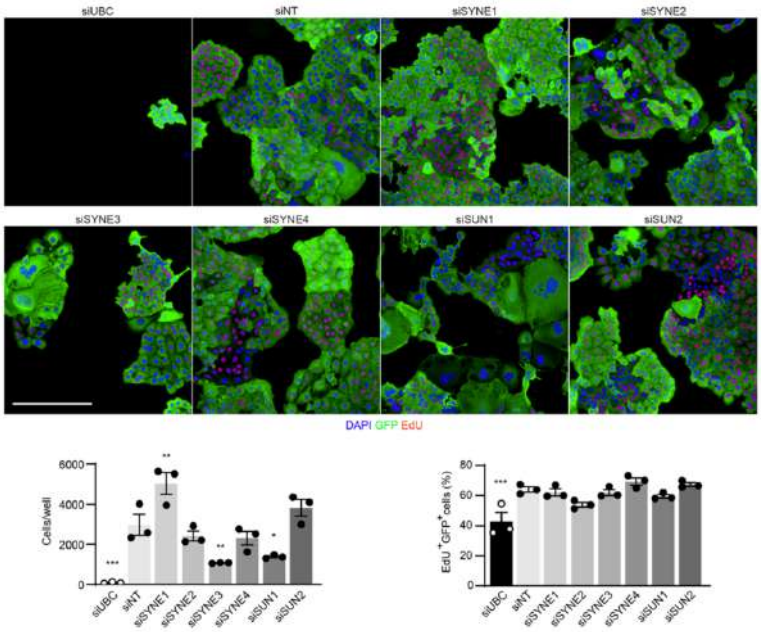

Figure 3-47. Representative images of LG1233 cells upon transfection with the indicated siRNAs. Proliferating nuclei are labelled by EdU. Scale bar: 100 µm (top). Quantification of the number of LG1233 cells after 5 days of culture upon transfection with the indicated siRNAs (bottom left). Quantification of EdU+ LG1233 cells after 5 days of culture upon transfection with the indicated siRNAs (bottom right).

3.6.1.3. For colon cancer cells (CT26) and melanoma cancer cells (B6-F10), silencing of Nesprin-2 resulted in increased proliferative capacity and cell density

Subsequently, Nesprin-2 and Nesprin-4 were silenced in additional cancer cell lines that corresponded to the tumor types analyzed in the spatial transcriptomics of cardiac metastases, specifically CT26 colon cancer cells and B16-F10 melanoma cells. Proliferation was then evaluated in beating EHTs. The silencing of Nesprin-2 led to an

increase in both the area occupied by cancer cells and cell density within EHT cross-sections for CT26 cells (Figure 4-38) and B16-F10 cells (Figure 3-49).

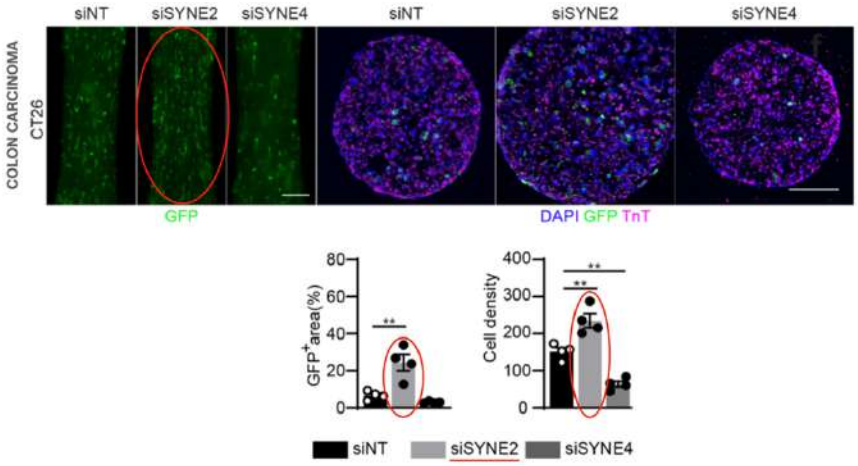

Figure 3-48. Representative low magnification images and cross sections of EHTs containing CT26 GFP+ colon cancer cells treated with the indicated siRNAs (top). Quantification of the area occupied by CT26 GFP+ cancer cells upon treatment with the indicated siRNAs (bottom left). Quantification of the density of CT26 GFP+ cancer cells in EHT cross-sections, upon treatment with the indicated siRNAs (bottom right). Scale bar: 100 µm.

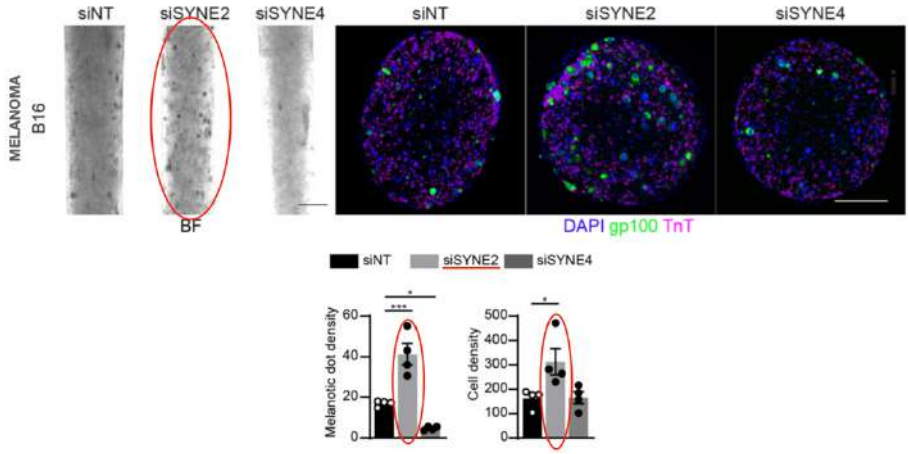

Figure 3-49. Representative low magnification bright-field images and cross sections of EHTs containing B16 melanoma cells, stained for gp100, treated with the indicated siRNAs (top). Quantification of the density of melanotic dots density upon treatment with the indicated siRNAs (bottom left). Quantification of the density of B16 gp100+ melanoma cells in EHT cross-sections, upon treatment with the indicated siRNAs (bottom right). Scale bar: 100 µm.

These findings indicate that Nesprin-2 functions as a critical mechanotransducer in regulating the proliferation of various cancer cell types within beating heart tissues.

3.6.1.4. Nesprin-2 is required to mediate chromatin decompaction in contracting EHT cells

We further examined whether Nesprin-2 was necessary to modulate chromatin structure in response to mechanical load. Figures 3-50 illustrate that Nesprin-2 silencing in LG1233 cells led to a marked increase in chromatin compaction within beating EHTs.

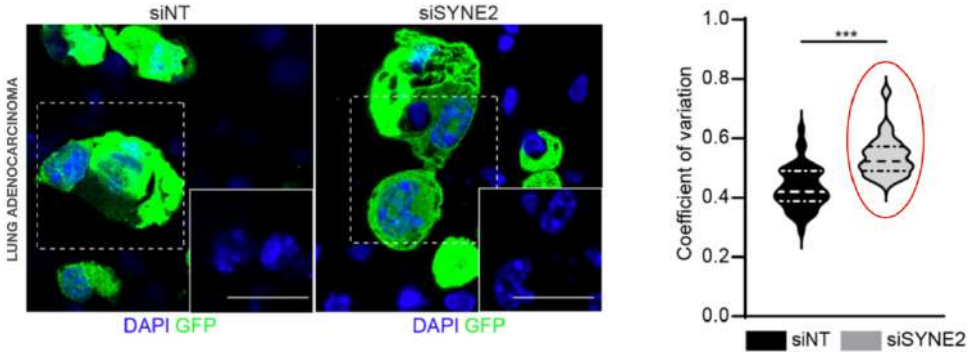

Figure 3-50. Representative images of chromatin compaction by DAPI staining of LG1233 GFP+ cancer cells in and EHTs treated with indicated siRNA (left). Coefficient of variation calculated based on the DAPI fluorescent images (right).

3.6.2. Nesprin-2 under Overloading Conditions

To delve deeper into the role of Nesprin-2 in cardiac mechanotransduction, we conducted experiments under both static and overloaded EHT conditions.

Across all cell types, the effect of Nesprin-2 silencing was more pronounced under conditions of increased mechanical load (Figure 3-51 for LG1233 cells – left and center), with many cells proliferating in the central region of the EHT, an area characterized by elevated hydrostatic compressive pressure (0–120 mm, Figure 3-51 - right).

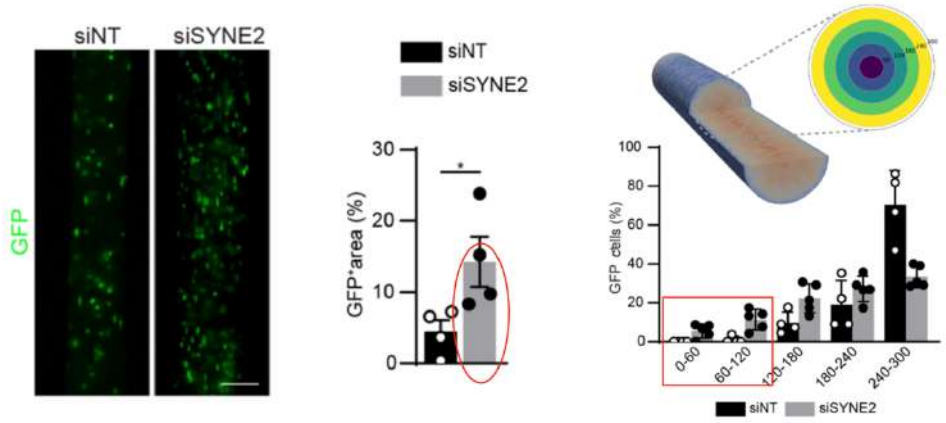

Figure 3-51. Representative low magnification images of overloaded EHTs containing LG1233 GFP+ cancer cells treated with the indicated siRNAs (left). Quantification of the area occupied by LG1233GFP+ cancer cells within overloaded EHTs upon treatment with the indicated siRNAs (center). Distribution of GFP+ cancer cells in the EHT radial layers depicted in different colors (right). Scale bar: 300 µm.

In static EHTs, by contrast, silencing Nesprin-2 did not affect the area occupied by any cell type. (Figure 3-52 for LG1233 cells).

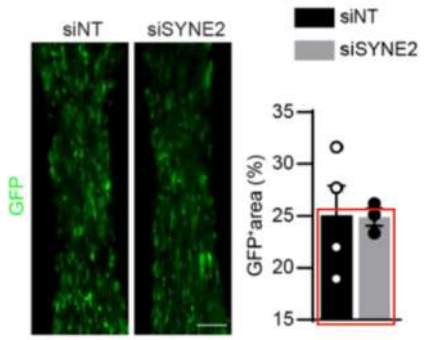

Figure 3-52. Representative low magnification images of static EHTs containing LG1233 GFP+ cancer cells treated with the indicated siRNAs (left). Quantification of the area occupied by LG1233 GFP+ cancer cells within static EHTs upon treatment with the indicated siRNAs (right). Scale bar: 300 µm.

Therefore, by increasing loading forces, the silencing effect of Nesprin-2 is further amplified.

3.6.3. Silencing Nesprin-2 in Vivo

3.6.3.1. Silencing of Nesprin-2 allows cancer cells to extensively expand and proliferate within the myocardium

Nesprin-2 was silenced in LG1233 cells prior to their in vivo implantation into beating hearts. In agreement with the observations from EHT experiments, Nesprin-2 silencing enabled cancer cells to expand significantly and proliferate within the myocardium (Figure 3-53).

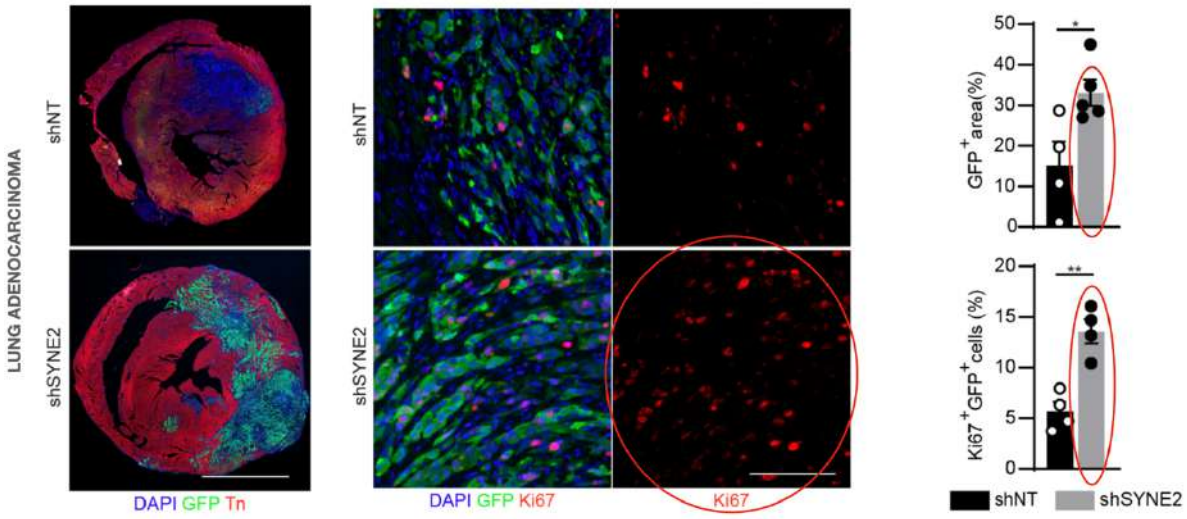

Figure 3-53. Representative immunofluorescence images of hearts injected with LG1233 GFP+ cancer cells transduced with lentiviral vectors expressing the indicated shRNAs (left). High magnification images of GFP+ LG1233 cells transduced with the indicated shRNAs and injected in the heart, stained for the proliferation marker Ki67 (center). Quantification of the area occupied by GFP+ LG1233 cells transduced with the indicated shRNAs and injected in vivo into the cardiac muscle (center). Quantification of proliferating GFP+ Ki67+ LG1233 cancer cells transduced with the indicated shRNAs and injected in vivo into the cardiac muscle (right). Scale bar: 1 mm (left), 50 µm (center).

3.6.3.2. Chromatin compaction is more pronounced in Nesprin-2 silenced cells

Similarly, consistent with earlier findings, Nesprin-2 silencing resulted in increased chromatin compaction in LG1233 cells implanted into beating hearts (Figure 3-54).

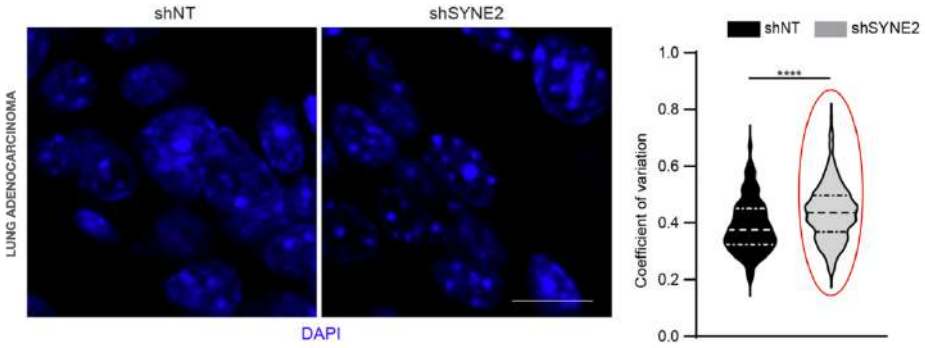

Figure 3-54. Coefficient of variation and representative images of chromatin compaction by DAPI staining of GFP+ LG1233 cancer cells transduced with the indicated shRNAs. Scale bar: 20 µm.

In summary, our findings demonstrate that mechanical load within beating heart tissue leads to a decrease in histone methylation and chromatin compaction in cancer cells, thereby limiting their proliferation. This process of mechanotransduction, which suppresses cancer cell growth in the heart, is critically mediated by Nesprin-2.

4. Discussion

The primary finding and novelty of this manuscript lies in demonstrating that variations in mechanical load have a pronounced impact on cancer cell growth within cardiac tissue. Specifically, mechanical load acts as an inhibitor of cancer cell proliferation both *in vivo* within beating hearts and *ex vivo* in engineered heart tissues (EHTs). In contrast, conditions of mechanical unloading promote cancer cell proliferation, effectively restoring their proliferative capacity. This is a significant insight as it sheds light on the interplay between mechanical forces and cancer biology in the heart, a relatively underexplored area.

4.1. The Importance of an Unloading Model

The use of an in vivo heterotopic transplantation model, as detailed in the previous sections, was crucial in validating the results of this study. The heterotopic model allowed for the accurate simulation of mechanical loading and unloading conditions, providing invaluable insights that would not have been as reliable if only in vitro models had been used. These models offered a more complex, dynamic system where the effects of mechanical load on cancer cell proliferation could be studied within the natural, highly structured environment of the heart.

In vitro models, while valuable for controlled experiments, cannot replicate the complexity of living organisms, particularly in terms of how mechanical forces influence cellular behavior within a tissue. The heterotopic transplantation approach, by transplanting the donor heart into the recipient's cervical region, simulated the mechanical forces that would be present in a living heart, such as compression and stretching during each heartbeat. This method allowed for the observation of cancer cell behavior in response to these forces in a living system, showing results with far greater physiological relevance.

Additionally, the heterotopic model demonstrated a significant enhancement in the applicability and consistency of the findings. While mechanical unloading was shown to promote cancer cell proliferation in isolated in vitro conditions, only within the heterotopic transplantation model did the effect of mechanical load inhibition become clearly evident. This model also proved essential in confirming the mechanistic insights uncovered, particularly with the influence of histone modifications and mechanotransduction pathways on cancer cell proliferation.

4.1.1. Considerations on the Key Stages of HHT

This experience aims to highlight the importance of precision in each phase of the transplantation, as even minor adjustments in the surgical process—such as suture placement or tissue manipulation—directly influence the viability of the graft and its functional outcomes.

During the explantation phase: each micro-movement, suture placement, and adjustment directly influences the viability of the graft and the functional outcome of the procedure.
During the vessel preparation phase: based on my personal experience, the dilation of the common carotid artery is by far the most critical step, essential for the successful eversion of the common carotid artery onto the cuff. Given the arterial nature of the vessel, its extensibility is significantly lower compared to the external jugular vein, whereas its retractability is extremely high. Any minor miscalculation of the length previously obtained will impact this step, potentially preventing the artery from wrapping around the cuff. Further optimization of the eversion technique for the common carotid artery could reduce the risks associated with minor miscalculations during artery length measurements, which can impede the successful wrapping of the artery around the cuff.
During the implantation phase: the goal is not just technical completion but the establishment of a stable and functional connection between the donor heart and the recipient's vascular system. The beating of the transplanted heart is a testament to the surgical accuracy and the success of the procedure.

4.1.2. The Minimally Invasive Approach to Common Carotid Artery Isolation

The surgical refinement introduced by avoiding the sectioning of the sternocleidomastoid (SCM) muscle played a pivotal role in enhancing the success of the procedure. By creating space between the SCM and the sternothyroid muscle through blunt dissection, the procedure not only reduced tissue trauma but also shortened the operative time and minimized bleeding, contributing to a smoother recovery for the animal. This improvement, as described in the Results section, significantly optimized the overall surgical efficiency, reinforcing the importance of minimizing muscle damage during the operation. The reduction in complications provided a more stable foundation for the transplantation, ultimately increasing the stability of the outcomes.

4.1.3. Limitations of the Procedure

However, it is important to recognize the limitations of the heterotopic transplantation methodology. One key challenge is the extremely complex and lengthy learning curve associated with the procedure. Mastery of the necessary microsurgical techniques takes significant practice and experience. Moreover, even when the procedure is well-executed, the mortality rate can still be relatively high, posing a significant obstacle to the model's consistency and reliability.
Enhanced techniques in these areas would improve the overall efficiency of the procedure, minimizing complications and maximizing graft success.

4.2. Impact of Mechanical Load on Proliferation

The inhibitory effect of mechanical load on cardiomyocyte (CM) proliferation has been previously observed in other contexts, such as patients implanted with left ventricular

assist devices (LVADs) and mouse models of myocardial infarction, where unloading conditions were shown to promote CM proliferation [3; 67]. However, this study offers the first evidence that a similar mechanism may also suppress cancer cell proliferation in the heart, potentially serving as a protective barrier against cardiac metastases. This novel discovery bridges the fields of cancer biology and mechanobiology, offering fundamental insights into the unique environment of the heart.

We initially focused on lung adenocarcinoma cells to explore this phenomenon. This choice was motivated by the fact that the lung, like the heart, is continuously exposed to mechanical stimulation. However, the nature of the mechanical forces differs significantly between the two organs. The heart experiences compressive forces due to cardiomyocyte contraction, as demonstrated in the study's models, whereas the lung is subject to stretching forces from diaphragm and intercostal muscle activity. Additionally, lung cancer ranks mid-level in terms of metastatic dissemination to the heart, making it an appropriate model for evaluating the effects of mechanical loading and unloading [8]. To generalize their findings, we extended our research to melanoma and colon cancer cells, which exhibit high and low frequencies of heart metastases, respectively [8; 68-69]. This comparative approach strengthened the conclusion that mechanical load influences cancer cell proliferation across various cancer types.

4.3. Mechanobiology and Cancer Proliferation

Mechanobiology has primarily focused on how cells sense alterations in matrix stiffness and other extracellular physical properties, translating these cues into modified behaviors such as proliferation and invasiveness [70-71]. The current study advances this field by providing robust evidence for the inhibitory effects of compressive forces, like those generated in a beating heart, on cancer cell proliferation. This finding aligns with previous studies, where compressive forces exerted by cancer-associated fibroblasts were shown to suppress proliferation via altered localization of YAP protein. Similarly, volumetric compression induced by osmotic pressure was reported to inhibit melanoma cell proliferation and migration [72-73].

In this study, transcriptomic analysis revealed that histone demethylases were among the most upregulated genes in cardiac metastases, irrespective of the tumor's origin. These enzymes, which dynamically regulate histone methylation, are known to play critical roles in various cancer progression processes, including proliferation, migration, invasiveness, and drug resistance [74-77]. We focused specifically on H3K9 trimethylation (H3K9me3), a hallmark of heterochromatin associated with chromatin compaction and gene expression regulation. We observed that mechanical loading decreased H3K9me3 levels and chromatin compaction across all experimental settings, including native versus heterotransplanted hearts, overloaded versus unloaded EHTs, and human cardiac metastases versus extra-cardiac lesions [78-84].

4.4. Experimental Validation of Mechanistic Insights

To validate the causal relationship between H3K9 trimethylation and cancer cell proliferation under mechanical load, we silenced key histone demethylases, KDM4C and KDM4D, in cancer cells. This intervention resulted in increased proliferation, confirming that these enzymes play a critical role in the observed mechanoresponse. This mechanistic insight is highly relevant, especially in light of recent clinical trials targeting histone-modifying enzymes like KDMs and lysine methyltransferases (KMTs) for cancer therapy [85]. The findings raise the intriguing possibility that such therapies might inadvertently influence the incidence of cardiac cancers, warranting further investigation.

4.5. Role of Nesprin-2 in Mechanotransduction

A critical component of the mechanotransduction pathway identified in this study is the LINC (Linker of Nucleoskeleton and Cytoskeleton) complex, particularly Nesprin-2. This molecule was shown to be essential for halting cancer cell proliferation in response to mechanical load, as its silencing allowed cancer cells to proliferate even in beating EHTs and in vivo hearts. This observation aligns with Nesprin-2's documented role in regulating nuclear architecture, chromatin organization, and the transcription of cancer-associated genes in response to mechanical forces [86]. By identifying Nesprin-2 as a key mediator, this study provides a molecular link between mechanical load and epigenetic regulation, adding a new dimension to our understanding of cancer cell biology.

5. Conclusions

The findings from this study underscore the importance of mechanical forces in regulating cancer cell behavior, particularly in the heart, a site that traditionally experiences low rates of metastasis. By employing a heterotopic transplantation model, the study moved beyond the limitations of in vitro models, providing more robust and applicable results. This model not only validated the hypothesis that mechanical loading inhibits cancer cell proliferation but also revealed key molecular mechanisms, such as histone demethylation and chromatin compaction, that could be targeted therapeutically.

The results suggest a protective role for the mechanical environment of the heart against metastasis, potentially explaining the rarity of cardiac tumors despite the heart's high blood flow. Importantly, the study opens new avenues for therapeutic interventions that could harness mechanical forces to suppress tumor growth in other tissues. By mimicking the mechanical forces experienced in the heart, it may be possible to develop novel mechanical therapies for cancer, particularly in tissues prone to metastatic invasion.

In future research, further refinements to the surgical techniques employed in the heterotopic transplantation model could optimize short-term survival rates for the recipient animals. These improvements would contribute to the reproducibility and consistency of results, enhancing the overall success of the procedure.

The insights gained from this research contribute to our understanding of cancer cell behavior in response to mechanical forces and open avenues for targeted therapies that utilize mechanical stimuli. Future studies should explore the broader applications of these findings in other tissues and cancer types, with the potential for clinical applications to improve cancer treatments and reduce metastasis.

References

1. Giacca, M. et al., "Harnessing the micro-RNA pathway for cardiac regeneration," 2015.
2. Puente, B. N. et al., "Oxygen increases oxidative stress and halts cardiomyocyte cell cycle," 2014.
3. Canseco, D. C. et al., "Human mechanical unloading induces cardiomyocyte proliferation," 2015.
4. Kocijan, T. et al., "Genetic lineage tracing reveals poor angiogenic potential of cardiac endothelial cells," 2020.
5. Meschia, G. et al., "Fetal circulation and oxygen saturation levels," 2011.
6. Lopaschuk, G. D. & Jaswal, J. S., "Metabolic adaptations in postnatal cardiomyocytes," 2010.
7. Nolfi-Donegan, D. et al., "Mitochondrial ROS and DDR activation," 2020.
8. Bussani, R. et al., "Epidemiology of primary and secondary cardiac tumors," 2007.
9. Amano, J. et al., "Metastatic mechanisms in the heart," 2013.
10. Al-Mamgani, A. et al., "Cardiac metastases distribution and impact," 2008.
11. Bergmann, O. et al., "Annual cardiomyocyte renewal rate in adults," 2009.
12. Rubart, M. & Field, L. J., "Cellular composition of the heart," 2006.
13. Roberts, W. C., "Primary cardiac tumors arising in epicardium and atrial walls," 1997.
14. Burke, A. P. et al., "Classification of primary cardiac tumors," 1990.
15. Ekmektzoglou, K. A. et al., "Cardiac tumors: benign and malignant," 2008.
16. Lestuzzi, C., "Clinical features of cardiac myxomas," 2016.
17. Burke, A. & Virmani, R., "Rhabdomyomas and their clinical significance," 2008.
18. Nwachukwu, N. et al., "Fibromas in pediatric cardiology," 2011.
19. Shu, J. et al., "Clinical features of cardiac lipomas," 2021.
20. Maleszewski, J. et al., "Hamartomas in the cardiac context," 2018.
21. Joshi, P. et al., "MDM2 expression in undifferentiated sarcomas," 2020.
22. Taguchi, T., "Prognosis and progression of angiosarcomas," 2018.
23. Tischoff, I. & Tannapfel, A., "Clinical aspects of pericardial mesotheliomas," 2017.
24. Zhao, Y. et al., "B-cell cardiac lymphomas," 2021.
25. Lee, J. et al., "Mechanobiology: cellular response to mechanical stimuli," 2011.
26. Szczesny, S. E. & Mauck, R. L., "Advances in mechanotransduction mechanisms," 2017.
27. Liu, Y. et al., "Mechanotransduction and cellular adaptation," 2023.
28. Zacchigna, S. & Giacca, M., "Mechanical load and subepicardial growth," 2014.
29. Kikuchi, K. et al., "Regenerative capacity in vertebrate cardiac chambers," 2010.
30. Sun, J. et al., "Nuclear mechanics in disease progression," 2020.

31. Schreiner, S. M. et al., "Nuclear mechanotransduction pathways," 2015.
32. Pajerowski, J. et al., "Nuclear deformation in cancer cells," 2007.
33. Roberts et al. 2021.
34. Enyedi et al., "Nuclear membrane stretch and its role in mechanotransduction", 2016.
35. Neelam et al., "Direct force measurements on the cell nucleus using optical tweezers", 2015.
36. Friedl et al., "Classifying collective cancer cell invasion", 2011.
37. Li et al., "Nuclear lamin A/C as a mechanotransducer mediating cellular mechanoadaptation and mechanotransduction", 2015.
38. Zullo et al., "DNA sequence-dependent compartmentalization and silencing of chromatin at the nuclear lamina", 2012.
39. Dahl et al., "Power-law rheology of isolated nuclei with deformation mapping of nuclear substructures", 2005.
40. Feinberg et al., "Assessing the stiffness of biological materials and tissues using atomic force microscopy", 2016.
41. Tajik et al., "Transcription upregulation via force-induced direct stretching of chromatin", 2016.
42. Elosegui-Artola, A. et al., "Mechanosensitive gene expression via LINC," 2017.
43. Davidson et al. "Nuclear deformability constitutes a rate-limiting step during cell migration in 3-D environments", 2014.
44. Alam, S. et al., "LINC complex in tumor invasion and metastasis," 2016.
45. Gundersen, G. G. & Worman, H. J., "Role of LINC in mechanotransduction," 2013.
46. Janota et al., "The LINC complex: ushering the nucleus into position", 2017.
47. Nie et al., 2016.
48. Harada, T. et al., "Nuclear deformability and migration," 2014.
49. Razafsky, D. et al., "LINC-mediated genomic stability," 2013.
50. Matsumoto, A. et al., "Downregulation of nesprins in breast cancer," 2015.
51. Sjöblom, T. et al., "Mutations in LINC components in gastrointestinal cancers," 2023.
52. Guilluy, C. et al., "Force transmission in cancer cell migration," 2014.
53. Stewart-Hutchinson et al., "Structural requirements for the assembly of LINC complexes and their function in cellular mechanical stiffness", 2008
54. g et al., "A new mouse model of heterotopic heart transplantation to study graft arteriosclerosis", 1991.
55. Wang et al., "A novel murine model of heterotopic heart transplantation for the study of transplant arteriosclerosis", 2002.
56. Yasura et al., "A new technique for heterotopic cardiac transplantation in mice", 1991;
57. A. K. Nowocin et al., "An extraperitoneal technique for murine heterotopic cardiac transplantation", 2015.

58. Oberhuber et al., “Murine cervical heart transplantation model using a modified cuff technique”, 2014.
59. Eschenhagen, T. et al., "Development of engineered heart tissues," 2002.
60. Hansen, A. et al., "Miniaturization and scalability of EHTs," 2010.
61. Janmey, P. A. et al., "Fibrin as a biopolymer in tissue engineering," 2009.
62. Ratschiller, T. *et al., “*Heterotopic Cervical Heart Transplantation in Mice”, 2015.
63. Dupont, C. *et al. “*Evidence for low nanocompaction of heterochromatin in living embryonicstem cells”, 2023.
64. Ramirez-Cuellar, J. *et al. “*LATS1 controls CTCF chromatin occupancy and hormonal response of 3D-grown breast cancer cells”, 2024.
65. Salinas-Pena, M. e al., “Imaging analysis of six human histone H1 variants reveals universal enrichment of H1.2, H1.3, and H1.5 at the nuclear periphery and nucleolar H1X presence”, 2024.
66. Mejat, et Al., “LINC complexes in health and disease”, 2010.
67. Suzuki, R. *et al., “*The reduction of hemodynamic loading assists self-regeneration of the injured heart by increasing cell proliferation, inhibiting cell apoptosis, and inducing stem-cell recruitment”, 2007.
68. Bussani, R. *et al., “*Cardiac Tumors: Diagnosis, Prognosis, and Treatment”, 2020.
69. Nova-Camacho, L. M. *et al., “*Cardiac Metastasis From Solid Cancers: A 35-Year Single-Center Autopsy Study”, 2023.
70. Bertolio, R. *et al*., “Dynamic links between mechanical forces and metabolism shape the tumor milieu”, 2023.
71. Mohammadi, H. *et al*., “Mechanisms and impact of altered tumour mechanics”, 2018.
72. Barbazan, J. *et al. “*Cancer-associated fibroblasts actively compress cancer cells and modulate mechanotransduction”, 2023.
73. Zhang, X. *et al. “*Compression drives diverse transcriptomic and phenotypic adaptations in melanoma”., 2023.
74. An, X. *et al*., “ Histone modification: Biomarkers and potential therapies in colorectal cancer”, 2023.
75. Audia, J. E. *et al*. “Histone Modifications and Cancer”, 2016.
76. Chen, Y. *et al*. “ The role of histone methylation in the development of digestive cancers: a potential direction for cancer management”, 2020.
77. Zhuang, J. *et al*., “Perspectives on the Role of Histone modification in Breast Canter Progression and the Advanced Technological Tools to Study Epigenetic Determinants of Metastasis”, 2020.
78. Sterling, J. *et al*. “Histone lysine demethylases and their functions in cancer”, 2021.
79. Black, J. C. *et al*., “Histone lysine methylation dynamics: establishment, regulation, and biological impact”, (2012).

80. Yokoyama, Y. *et al., "*Cancer-associated upregulation of histone H3 lysine 9 trimethylation promotes cell motility in vitro and drives tumor formation in vivo", 2013.
81. Gaggioli, V. *et al., "* Dynamic de novo heterochromatin assembly and disassembly at replication forks ensures fork stability", 2023.
82. Lam-Ubol, A. *et al*., Distinct histone H3 modification profiles correlate with aggressive characteristics of salivary gland neoplasms", 2022.
83. Keung, E. Z. *et al., "*Increased H3K9me3 drives dedifferentiated phenotype via KLF6 repression in liposarcoma", 2015.
84. Chen, M. W. *et al., "*H3K9 histone methyltransferase G9a promotes lung cancer invasion and metastasis by silencing the cell adhesion molecule Ep-CAM", 2010.
85. Yu, X. *et al., "*Cancer epigenetics: from laboratory studies and clinical trials to precision medicine", 2024.
86. Li Mow Chee, F. *et al., "* Mena regulates nesprin-2 to control actin-nuclear lamina associations, trans-nuclear membrane signalling and gene expression", 2023.

Acknowledgements

Prof. Serena Zacchigna
Prof. Gabriele Stocco
Prof. Marianna Lucafò
Giulio Ciucci, PhD
Roman Vuerich, PhD
Simone Vodret, PhD
Andrea Colliva, PhD
Ann-Vu Nguyen, PhD